

# **KESS - A new Monte Carlo simulation code for low-energy electron interactions in silicon detectors**

Zur Erlangung des akademischen Grades eines  
DOKTORS DER NATURWISSENSCHAFTEN  
von der Fakultät für Physik des  
Karlsruher Instituts für Technologie (KIT)

genehmigte

DISSERTATION

von

Dipl. Phys. Pascal Renschler  
aus Karlsruhe

Tag der mündlichen Prüfung: 28.10.2011

Referent: Prof. Dr. J. Blümer  
Institut für Experimentelle Kernphysik, KIT

Korreferent: Prof. Dr. G. Quast  
Institut für Experimentelle Kernphysik, KIT

Hiermit versichere ich die vorliegende Arbeit selbstständig und nur unter Verwendung der angegebenen Hilfsmittel und Quellen verfasst zu haben.

Karlsruhe, den 10. Mai 2011 .....

# Contents

<b>List of Figures</b>	<b>e</b>
<b>List of Tables</b>	<b>g</b>
<b>Abstract</b>	<b>i</b>
<b>1 Introduction</b>	<b>1</b>
1.1 The discovery of the neutrino and the standard model . . . . .	1
1.2 Neutrino oscillations . . . . .	3
1.3 Measurement of the neutrino mass . . . . .	7
<b>2 The KATRIN experiment</b>	<b>11</b>
2.1 Theory and measurement principle . . . . .	11
2.2 The source and transport section . . . . .	13
2.3 The spectrometer section . . . . .	14
2.4 Systematic and statistical uncertainties . . . . .	16
<b>3 Detector systems of the KATRIN experiment</b>	<b>21</b>
3.1 The focal plane detector system . . . . .	22
3.2 The pre-spectrometer test experiment . . . . .	25
3.2.1 Experimental setup . . . . .	25
3.2.2 The pre-spectrometer detector system . . . . .	27
3.3 The forward beam monitor detector system . . . . .	28
3.3.1 Area of application . . . . .	28
3.3.2 Experimental setup . . . . .	29
<b>4 Monte Carlo simulations of keV electrons in solids</b>	<b>33</b>
4.1 Motivation . . . . .	34
4.1.1 Detector response to x-rays and electrons . . . . .	34
4.1.2 Efficiency of the focal plane detector . . . . .	36
4.1.3 Simulation of the detector response . . . . .	38
4.2 Electron scattering in silicon . . . . .	42
4.2.1 Inelastic collision cross sections . . . . .	42
4.2.2 Elastic scattering cross sections . . . . .	46
4.3 Secondary electron production . . . . .	48
4.3.1 Ionization and knock-on electrons . . . . .	48
4.3.2 Auger electrons . . . . .	50

4.4	The surface escape process . . . . .	51
4.5	Electron track generation . . . . .	54
4.6	KESS in the global KATRIN simulation framework Kassiopeia . . . . .	57
<b>5</b>	<b>KESS benchmarks and results</b>	<b>59</b>
5.1	The influence of secondary electrons . . . . .	60
5.2	Backscattering from the detector surface . . . . .	64
5.2.1	Primary backscattering coefficient . . . . .	65
5.2.2	Secondary backscattering yield . . . . .	69
5.2.3	Energy spectra of backscattered electrons . . . . .	70
5.2.4	Angular distribution of backscattered electrons . . . . .	75
5.3	Dead layer effects . . . . .	77
5.3.1	Dead layer models . . . . .	77
5.3.2	Influence on the detector response . . . . .	80
5.3.3	Comparison to continuous-slowing-down-approximation dead layers . . . . .	82
<b>6</b>	<b>KESS application for KATRIN</b>	<b>85</b>
6.1	The detector response of KATRIN detectors . . . . .	86
6.1.1	Focal plane detector . . . . .	86
6.1.2	Forward beam monitor detector . . . . .	92
6.2	The detector response including electromagnetic design . . . . .	95
6.2.1	Pre-spectrometer transmission at high surplus energies . . . . .	95
6.2.2	Efficiency of the focal plane detector in the final KATRIN setup	101
<b>7</b>	<b>Summary and Outlook</b>	<b>111</b>
7.1	Summary . . . . .	111
7.2	Outlook . . . . .	116
<b>A</b>	<b>Appendix</b>	<b>119</b>
A.1	Standard KESS simulation settings . . . . .	119
A.2	Additional focal plane detector figures . . . . .	119
	<b>Acknowledgements</b>	<b>I</b>
	<b>Bibliography</b>	<b>III</b>

# List of Figures

1.1	Allowed regions for neutrino oscillation parameters by KamLAND . . .	6
1.2	Mass scale of the neutrino mass eigenvalues . . . . .	7
1.3	Feynman graph of neutrinoless double beta decay . . . . .	8
1.4	Results on the neutrino mass from $\beta$ -decay experiments since 1990 . .	10
2.1	The tritium $\beta$ -spectrum . . . . .	11
2.2	The KATRIN experimental setup . . . . .	13
2.3	KATRIN components containing tritium . . . . .	14
2.4	MAC-E filter principle . . . . .	15
2.5	Transmission and response function . . . . .	17
3.1	Drawing of the focal plane detector system . . . . .	22
3.2	The segmentation of the focal plane detector . . . . .	24
3.3	The KATRIN pre-spectrometer test experiment . . . . .	26
3.4	The schematic and real setup of the pre-spectrometer detector . . . .	27
3.5	Photographs of the forward beam monitor detector system . . . . .	30
4.1	Simulated detector response to x-rays and electrons . . . . .	35
4.2	Energy distribution of a mono-energetic electron beam after 100 nm of silicon . . . . .	40
4.3	Energy distribution of backscattered electrons for 1 keV incident elec- trons . . . . .	41
4.4	Mean free path and energy loss function . . . . .	44
4.5	Probability density functions for scattering . . . . .	46
4.6	Schematic energy levels of solid silicon . . . . .	48
4.7	Ionization probabilities . . . . .	50
4.8	The transmission probability . . . . .	53
4.9	Simulated tracks of electrons in Si . . . . .	55
4.10	Overview of angles used in the simulation . . . . .	56
4.11	Magnetron motion in inhomogeneous magnetic fields . . . . .	58
5.1	Energy deposit by 18 keV electrons in a detector . . . . .	62
5.2	Energy distribution of backscattered electrons . . . . .	64
5.3	The primary backscattering coefficient for various incident energies and angles . . . . .	65
5.4	The primary backscattering coefficient . . . . .	66
5.5	The primary backscattering coefficient over the incident angle . . . .	68

List of Figures

5.6	The secondary backscattering yield over the electron incident energy .	69
5.7	Energy spectrum of backscattered electrons, 1 keV . . . . .	71
5.8	Energy spectrum of backscattered electrons, 0.5 keV to 5 keV . . . . .	72
5.9	The spatial distribution of the backscattered energy . . . . .	74
5.10	Angular distribution of backscattered electrons . . . . .	76
5.11	Energy distribution of a mono-energetic electron beam after traversing 100 nm of silicon . . . . .	78
5.12	Overview of dead layer models . . . . .	79
5.13	Energy spectra obtained from different dead layer models . . . . .	81
5.14	Comparison of KESS and continuous-slowng-down-approximation dead layers . . . . .	83
6.1	Best-fit dead layer values for pixel 140 . . . . .	88
6.2	Comparison of KESS simulations to focal plane detector data for pixel 140 . . . . .	89
6.3	Comparison of KESS simulations to focal plane detector data for pixel 140 with a modified energy calibration . . . . .	89
6.4	Offset and slope variations of the energy calibration of the focal plane detector . . . . .	90
6.5	Simulated and experimental detector response of the forward beam monitor detector . . . . .	93
6.6	Simulation setup of the pre-spectrometer . . . . .	96
6.7	Pre-spectrometer transmission at high surplus . . . . .	99
6.8	Energy dependent detection efficiency . . . . .	100
6.9	Simulation setup for the mainspectrometer and focal plane detector .	102
6.10	Simulated focal plane detector efficiency $\varepsilon$ over the initial polar angle $\theta_{\text{PMS}}$ . . . . .	104
6.11	Simulated focal plane detector efficiency $\varepsilon$ over the dead layer $\lambda_{\text{D}}$ . .	104
6.12	Simulated focal plane detector efficiency $\varepsilon$ over the retarding potential	106
6.13	Simulated focal plane detector efficiency $\varepsilon$ over the initial energy . . .	106
6.14	Systematic error on $m_{\nu}^2$ . . . . .	109
6.15	Multiple focal plane detector hits by one electron . . . . .	110
7.1	Comparison of KESS simulations to experimental data . . . . .	113
A.1	Best-fit dead layer values for pixel 61 . . . . .	120
A.2	Comparison of FPD data to simulations for pixel 61 with a modified energy calibration . . . . .	120
A.3	Best-fit dead layer values for pixel 52 . . . . .	121
A.4	Comparison of FPD data to simulations for pixel 52 with a modified energy calibration . . . . .	121

# List of Tables

1.1	The fermions of the standard model . . . . .	2
2.1	Reference parameters used to calculate the statistical error on $m_\nu^2$ . . .	19
2.2	Summary of sources of systematic errors on $m_\nu^2$ . . . . .	19
3.1	Comparison of focal plane detector and segmented PIN diode properties	28
4.1	Average number of ionized shells per track . . . . .	52
4.2	Shakeoff probability and shakeoff electron energies . . . . .	52
4.3	Transition probabilities for K-shell vacancies . . . . .	52
4.4	Transition probabilities for L-shell vacancies . . . . .	52
5.1	Fit parameters for the peak shift over the dead layer thickness . . . . .	84
6.1	$\chi^2$ -values and dead layer thicknesses for three focal plane detector pixels . . . . .	91
6.2	Fit parameters for an energy dependent slope $d\varepsilon(E_{\text{PMS}})/dE$ . . . . .	105
A.1	Standard simulations settings . . . . .	119



# Abstract

The evidence for massive neutrinos and its impact on particle physics and cosmology emphasizes the need for the measurement of the neutrino mass. The **K**arlsruhe **T**ritium **N**eutrino experiment KATRIN will determine the electron antineutrino mass with a sensitivity of  $m(\bar{\nu}_e) \leq 0.2 \text{ eV}/c^2$  (90% C.L.). It uses a direct approach by measuring the tritium  $\beta$ -decay spectrum with high accuracy. From the spectral shape, the neutrino mass can be derived in a model-independent way. The current upper limit from direct measurements is  $m(\bar{\nu}_e) < 2.3 \text{ eV}/c^2$  (95% C.L.) [1, 2].

In the KATRIN experiment, electrons emitted from a gaseous tritium source are magnetically guided to the focal plane detector (FPD) system. The electrons are discriminated according to their energy by a large electrostatic spectrometer. It is configured as a MAC-E filter with an energy resolution of  $\Delta E_{\text{MS}} = 0.93 \text{ eV}$ . Electrons with a longitudinal kinetic energy component larger than the spectrometer retarding potential are transmitted and re-accelerated to their original energy. Finally, they are counted at the focal plane detector to acquire the integrated tritium  $\beta$  spectrum.

To this day, no contribution to the systematic error on  $m_\nu^2$  is associated with the performance of the focal plane detector in the KATRIN neutrino mass analysis. This is due to the fact that the detector efficiency is an unconstrained fitting parameter in the analysis. In this study, the effects on the systematic error are examined under the assumption that the detection efficiency  $\varepsilon$  shows a dependence on the electron energy  $E$  or the spectrometer retarding potential (Sec. 6.2.2). This analysis set an upper limit for allowed, unaccounted for slopes of  $d\varepsilon/dE < 7 \times 10^{-4}/\text{eV}$ .

Because of the subtlety of these effects, the major part of the thesis was the development and validation of a simulation package, which models the interaction of the incident electrons with the detector wafer, and describes electron backscattering in detail.

Backscattering plays a central role in the description of the detector response of silicon detectors. Incident electrons have a probability of being backscattered from the surface of the detector depending on their polar incident angle  $\theta_1$  and incident energy  $E_1$ . Backscattered electrons contribute to the detected energy spectra by partial energy deposits, in general smaller than  $E_1$ .

A thin layer at the entrance side of silicon semiconductor detectors is insensitive to energy deposits (dead layer). Energy deposited there does not contribute to the detector signal. The dead layer thickness, which amounts to  $\sim 100 \text{ nm}$  for the focal plane detector, results in a shift of the incident energy peak from  $E_1$  to lower energies.

Backscattering and dead layer effects effectively reduce the detection efficiency of a detector system. Additionally, the detector response to a mono-energetic electron beam will have a low-energy tail and thus, a fraction of signals will be below the detection threshold. The threshold is defined by the noise of the electronic readout.

In the KATRIN beam line, backscattered electrons have a probability to return to the detector after being reflected by the magnetic mirror effect or the spectrometer retarding potential. This results in multiple passages through the dead layer and multiple backscattering, which further increases the influence on the detector response.

Existing simulation packages as the widely used `Geant4` or `Penelope2008` failed to achieve the required precision (Sec. 4.1.3). The software package developed in this study (`KESS`) is based on first principles and uses differential elastic and inelastic cross sections on single-event basis to describe the electron track and energy loss in crystalline silicon. Two approaches to the inelastic collision cross section are compared in this study. Secondary electrons are produced from ionization and the subsequent rearrangement of atomic shell electrons. Finally, `KESS` also considers the electron affinity of the detector surface, which leads to non-negligible effects when analyzing escape probabilities of secondary electrons from the detector surface to the vacuum. The simulation package `KESS` is included in the global KATRIN simulation framework `Kassiopeia`.

For validation, selected simulation results are presented and are evaluated against published experimental data in Chapter 5. The influence of secondary electrons on the detector response and on backscattering is discussed. Measurements of the primary backscattering coefficient and the secondary backscattering yield are compared to simulation results. Good agreement between experiment and simulation for the energy distribution of backscattered electrons is reported. Finally, the effects of a dead layer on the detector response are discussed. In this context, different dead layer geometries (i.e. charge collection profiles in dependence on the depth) are compared against each other. It will be shown that a step-like dead layer is generally a good approximation for the focal plane detector, as long as systematic uncertainties on the order of  $10^{-3}$  for the total detection efficiency are acceptable.

Chapter 6 shows the application of `KESS` simulations for the KATRIN experiment. Simulation results are compared to experimental energy spectra of the focal plane detector (PIN diode technology) and the forward beam monitor detector (silicon-drift technology). It will be shown that the dead layer thickness should generally be treated as a free parameter in simulations. When allowing for adjustments of the calibration coefficients of the ADC-to-energy calibration within their errors, `KESS` is able to reproduce the measured detector response.

Transmission function measurements of the pre-spectrometer [3] are simulated, confirming its adiabatic transmission properties. Moreover, this analysis shows unambiguously the need to include detailed backscattering simulations in the data analysis

to describe and understand the measured spectra correctly. Finally in this chapter, the contribution of the focal plane detector system to the statistical and systematic uncertainties on  $m_\nu^2$  are examined quantitatively.

As an introduction, the thesis starts by describing the discovery of the different neutrino flavors included in the standard model of particle physics in Chapter 1. The evidence for massive neutrinos from neutrino oscillations is presented and an overview over methods for the direct neutrino mass measurements is given. The theory, measurement principle and experimental setup of the KATRIN experiment are outlined in Chapter 2. Additionally, the statistic and systematic uncertainties on  $m_\nu^2$  are discussed.

Finally, selected silicon semiconductor detector systems used in the KATRIN experiment and important for the present study are described in Chapter 3:

- The focal plane detector (FPD) system detects the high-energy part of the tritium  $\beta$ -spectrum and acts as the KATRIN main detector.
- A predecessor of the focal plane detector, the segmented PIN diode (SPD), is used at the KATRIN pre-spectrometer test experiment.
- The forward beam monitor detector (FBMD) is located between the source and the spectrometer region and therefore detects the complete  $\beta$ -spectrum.

It will be shown in this study that the detector response of these detector systems can be successfully simulated with **KESS**. Furthermore, the good agreement with experimental data (e.g. the spectral distribution of backscattered electrons) suggests that **KESS** is also applicable to spectroscopic electron energy-loss measurements of solid silicon.



# 1 Introduction

This chapter gives a brief historic overview from the postulation of the neutrino to the experimental confirmation of the different kinds of neutrinos. The evidence for massive neutrinos and its impact on various branches of today's physics is described. Finally, experimental approaches for a model-independent measurement of the neutrino mass with a sensitivity of  $m(\bar{\nu}_e) \leq 0.2 \text{ eV}/c^2$  (90% C.L.) are presented.

## 1.1 The discovery of the neutrino and the standard model

The neutrino was postulated by Pauli in 1930 [4] and has been of interest for science since then. After the measurement of the discrete energy spectra of  $\alpha$ - and  $\gamma$ -rays, the continuous energy spectrum of the  $\beta$ -rays measured by Chadwick in 1914 [5] was puzzling. The  $\beta$ -decay was assumed to be a two-body decay and thus violated the fundamental law of energy conservation and quantum mechanical spin statistics. Pauli solved the problem 15 years later by introducing a hypothetical particle, simultaneously created with the  $\beta$ -electron and taking with it a part of the decay energy. Its properties had to be spin one half, electric neutrality and it would only interact very weakly with matter. Fermi continued Pauli's work and gave the still valid theoretical formulation of the  $\beta$ -decay [6]. Arising from Fermi's theory, the cross section for weak interactions of neutrinos with matter was very small. This made the experimental proof very difficult.

Pauli's postulated neutrino was finally detected in 1956 at the Savannah River Plant nuclear reactor by Reines and Cowan [7]. The experimental setup consisted of a diluted cadmium chloride dissolution encapsulated by two liquid scintillator detectors. The electron antineutrinos from the nuclear reactor interacted with the free protons in the cadmium chloride dissolution by the inverted  $\beta$ -decay

$$\bar{\nu}_e + p \rightarrow e^+ + n. \quad (1.1)$$

The characteristic signature for this reaction that allowed for electron anti-neutrino identification was the observation of the chronological and spatial correlation of  $\gamma$  particles created by the positron annihilation and the delayed capture onto cadmium.

In 1962, Schwartz, Ledermann and Steinberger discovered experimental evidence for a second type of neutrino [8]. They investigated pion decays from a pion beam,

## 1 Introduction

created by a particle accelerator, nowadays described by

$$\pi^+ \rightarrow \mu^+ + \nu_\mu, \quad \pi^- \rightarrow \mu^- + \bar{\nu}_\mu. \quad (1.2)$$

Neutrinos created in this decay never induced the creation of electrons or positrons; only  $\mu^\pm$  were created. With this, two types of neutrinos,  $\bar{\nu}_e$  and  $\nu_\mu, \bar{\nu}_\mu$ , were detected experimentally.

The third neutrino  $\nu_\tau$  existing in the standard model was discovered in 2001 by the DONUT experiment at Fermilab [9]. A 800 GeV proton beam was fired at a tungsten target. The leptonic decay of  $D_s$  mesons, resulting in  $\tau$  and  $\nu_\tau$  was investigated.

In 1958 Goldhaber experimentally determined the helicity of neutrinos to be  $h_\nu = -1.0 \pm 0.3$  [10]. Within the measurement accuracy, this result implies the maximum parity violation of weak interaction, as it was adopted in the standard model. If only exclusively left-handed neutrinos and right-handed antineutrinos exist, they must move with the speed of light and thus have a rest mass of zero.

The standard model of particle physics, developed in the sixties and seventies, includes twelve elementary particles, their antiparticles and the interactions through gauge bosons between them [11]. The elementary particles are divided into three generations and two families (leptons and quarks). They are shown in Table 1.1.

In addition to the electromagnetic and the weak interactions, quarks also participate in the strong interaction, in which their quantum number *color charge* is mediated by gluons. They only appear in neutral color charge doublets (mesons) or triplets (baryons) and are confined by the linearly increasing quark-quark potential. If a maximum distance is exceeded, the energy is sufficient to form two new quarks and thus creating two independent quark pairs [12].

The charged leptons participate in electromagnetic interactions. It is described by the coulomb potential and mediated by photons. The three neutral neutrinos (and their antiparticles) take part only in weak interactions, which is mediated by the  $Z^0$  and  $W^\pm$  bosons.

**Table 1.1: The fermions of the standard model**, their charge in units of the electron charge  $q = e$  and their rest mass or upper mass limit [2]. Each listed particle has an antiparticle.

	name			charge	mass [ $1/c^2$ ]		
generation	1	2	3	all	1	2	3
quarks	$u$	$c$	$t$	+2/3	2.4 MeV	1.27 GeV	172 GeV
	$d$	$s$	$b$	-1/3	4.8 MeV	101 MeV	4.2 GeV
leptons	$e^-$	$\mu^-$	$\tau^-$	-1	0.5 MeV	105 MeV	1.77 GeV
	$\nu_e$	$\nu_\mu$	$\nu_\tau$	0	< 2.3 eV	< 0.17 MeV	< 15.5 MeV

A measurement of the decay width of the  $Z^0$  boson at the LEP particle accelerator at CERN<sup>1</sup> determined the number of light neutrino generations to be  $N = 3.00 \pm 0.08$  [13].

The number  $N$  of the light neutrino generations, was determined to be from the decay width of the boson at . Therefore, no other active neutrino types are expected.

In the standard model, each of the three lepton generations, including one neutrino each, have a lepton flavor number  $L_\alpha$ , with  $\alpha = e, \mu, \tau$ , which is separately conserved. The neutrinos carry no electric charge, are massless and therefore have no magnetic dipole moment.

The masses of the fermions and  $Z^0, W^\pm$  gauge bosons are generated by the Higgs-mechanism and show a clear mass hierarchy over the generations (Tab. 1.1). However, the Higgs-mechanism fails for purely left-handed particles. Thus, the standard model has to be extended to explain massive neutrinos and the observation of massive neutrinos is regarded to be evidence for physics beyond the standard model.

## 1.2 Neutrino oscillations

In the nineties, hints towards massive neutrinos accumulated. The evidence for this arises from the phenomenon of flavor oscillation, in which the various neutrino species transform into each other, thus violating the conservation of lepton flavor. The flavor eigenstates  $|\alpha\rangle$ , with  $\alpha = e, \mu, \tau$ , are not identical with the mass eigenstates  $|m_i\rangle$ , with  $i = 1, 2, 3$ , but are given by the unitary  $3 \times 3$  mixing matrix  $U$  by

$$|\alpha\rangle = \sum_i U_{\alpha i} |m_i\rangle \quad (1.3)$$

The factorized form of the PMNS<sup>2</sup>-matrix  $U$  is

$$U = \begin{pmatrix} 1 & 0 & 0 \\ 0 & c_{23} & s_{23} \\ 0 & -s_{23} & c_{23} \end{pmatrix} \times \begin{pmatrix} c_{13} & 0 & s_{13}e^{i\delta} \\ 0 & 1 & 0 \\ -s_{13}e^{-i\delta} & 0 & c_{13} \end{pmatrix} \times \begin{pmatrix} c_{12} & -s_{12} & 0 \\ s_{12} & c_{12} & 0 \\ 0 & 0 & 1 \end{pmatrix} \times \begin{pmatrix} 1 & 0 & 0 \\ 0 & e^{-i\phi_2/2} & 0 \\ 0 & 0 & e^{-i(\phi_2/2+\delta)} \end{pmatrix} \quad (1.4)$$

with  $c_{ij} = \cos \theta_{ij}$  and  $s_{ij} = \sin \theta_{ij}$ , where  $\theta_{ij}$  are the three mixing angles. The phases  $\delta, \phi_2$  and  $\phi_3$  violate CP conservation. They are discussed in the next section.

<sup>1</sup>Organisation Européenne pour la Recherche Nucléaire, formerly Conseil Européen pour la Recherche Nucléaire

<sup>2</sup>Pontecorvo-Maki-Nakagawa-Sakata

## 1 Introduction

The transition probability  $P$  from a flavor state  $\alpha$  to a flavor state  $\beta$  in vacuum is given by

$$P_{\alpha \rightarrow \beta} = \left| \sum_i U_{\alpha i}^* U_{\beta i} e^{-i\Delta m_{ij}^2 L/2E} \right|^2 \quad \text{with } \Delta m_{ij} = m_i - m_j \neq 0 \text{ for } i \neq j, \quad (1.5)$$

with the pathlength  $L$  and the neutrino energy  $E$ .

The evidence of a flavor change indicates that neutrino types must have a different mass and therefore at least two are not massless. Additionally, the lepton flavor conservation is violated. Therefore neutrino flavor oscillations are not in accordance with the standard model.

Evidence for neutrino oscillations in the investigation of atmospheric neutrinos was first provided by the Super-Kamiokande experiment in 1998 [14]. High-energy cosmic rays produced in the upper atmosphere continuously produce secondary particles, including pions and kaons, which in their decays emit electron and muon neutrinos. The Super-Kamiokande detector is a cylindrical tank filled with 50 kt of ultra pure water shielded by about 1 km stone. The inside of the tank is equipped with more than 10,000 photomultiplier tubes. The electron and muon neutrino induced reactions

$$\nu_e + N \rightarrow X + e^- \quad (1.6)$$

$$\nu_\mu + N \rightarrow X + \mu^- \quad (1.7)$$

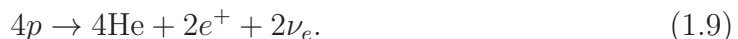
create leptons in the tank, which emit Cherenkov light cones, which were then detected by the photomultipliers. The interactions of  $\nu_e$  and  $\nu_\mu$  were distinguished through the edge sharpness of the detected rings and the direction of the incoming neutrino was determined.

The experimental results showed a strong correlation of the recorded  $\nu_\mu$ -rate with the angle of incidence and thus, with the distance traveled from  $L_{\min} = 15$  km to  $L_{\max} = 13000$  km. In contrast, the  $\nu_e$  rate was uncorrelated. Assuming a two-neutrino oscillation in vacuum between  $\nu_\mu$  and  $\nu_\tau$  with the transition probability

$$P_{\alpha \rightarrow \beta} = \sin^2 2\theta_{ij} \sin^2 \left( \frac{\Delta m_{ij}^2 L}{4E} \right), \quad (1.8)$$

a maximum mixing between  $\nu_\mu$  and  $\nu_\tau$  is derived from the experimental results. However, the  $\nu_\tau$  can not be detected with this experimental setup.

A second natural source for neutrinos is the sun. The multi-step pp-reaction chain creating electron neutrinos only, is given by



Among the reactions creating  $\nu_e$ , there are



Many different measurements of the electron neutrino flux  $\Phi_e$ , including the Homestake experiment conducted by Davis [15], GALLEX [16], SAGE [17] [18] and Super-Kamiokande consistently showed too low values over several years, to coincide with the standard model of the sun [19]. The Sudbury Neutrino Observatory (SNO) finally solved the solar  $\nu$ -problem and measured the fluxes  $\Phi_e$  and  $\Phi_{\mu,\tau}$  of all neutrino flavors [20]. For this purpose, similar to the Super-Kamiokande experiment, an underground tank was lined with thousands of photomultiplier tubes. But in this case it was filled with about 1000 t of heavy water ( $D_2O$ ). Thus, the various fluxes of the neutrino flavors could be detected by the reactions

$$\nu_e + d \rightarrow p + p + e^- \quad \Phi_e \quad (1.12)$$

$$\nu_\alpha + d \rightarrow p + n + \nu_\alpha \quad \Phi_e + \Phi_{\mu,\tau} \quad (1.13)$$

$$\nu_\alpha + d \rightarrow \nu_\alpha + e^- \quad \Phi_e + \frac{\Phi_{\mu,\tau}}{6.5}. \quad (1.14)$$

which includes the neutral current reaction (Eq. 1.13) and thus strongly decouples the analysis from solar physics. The analysis showed that the sum of the neutrino fluxes  $\Phi_{\mu,\tau}$  and  $\Phi_e$  matches the  $\nu_e$ -flux predicted by the standard model of the sun.

Since 2007, the Borexino experiment investigates the flux of  ${}^7\text{Be}$  electron neutrinos created by reaction 1.10. The results give rise to the LMA-MSW<sup>3</sup> neutrino oscillation as the correct complement for the theoretical models of neutrino oscillation in matter [26]. According to the LMA-MSW model, the  ${}^7\text{Be}$  neutrinos with a fixed energy of 0.862 MeV, for the first time detected in real-time by the Borexino experiment, have a survival probability when traveling the distance from the sun to the underground detector of  $P_{\tau\text{Be}} = 1 - P_{e \rightarrow \mu,\tau} \approx 66\%$ .

The  ${}^8\text{B}$  electron neutrinos created by reaction 1.11 with an energy of a few MeV were detected by Super-Kamiokande and SNO. They had a significantly lower survival probability of  $P_{\text{sB}} = 33\%$ . The results from Borexino and Super-Kamiokande agree with these predictions and thereby confirm the standard model of the sun, thus giving further evidence for the LMA-MSW neutrino oscillations in matter [26].

The KamLAND experiment [29] investigated electron antineutrinos emitted from nuclear reactors via the decay products of the reaction 1.1. Here, the detection took place in an underground tank that was filled with 1000 t of liquid scintillator and was lined with photomultiplier tubes. Within a radius of 100-200 km of the detector, about 70 nuclear power plants served as neutrino sources. The KamLAND experiment confirmed the disappearance of electron antineutrinos and therefore the neutrino oscillation. The results are in agreement with the LMA-MSW theory [21] (Fig. 1.1).

---

<sup>3</sup>Large Mixing Angle solution of the Mikheyev-Smirnov-Wolfenstein model. Complementary to the neutrino oscillation in vacuum, the MSW model describes the oscillation of electron or tau neutrinos in matter and thereby gives a correction for the ratio of  $\Delta m_{ij}^2$  to  $\tan \theta_{ij}$ . LMA designates solutions with a large mixing angle  $\sin^2 \theta_{ij}$ . See also [21], [22], [23], [24] and [25].

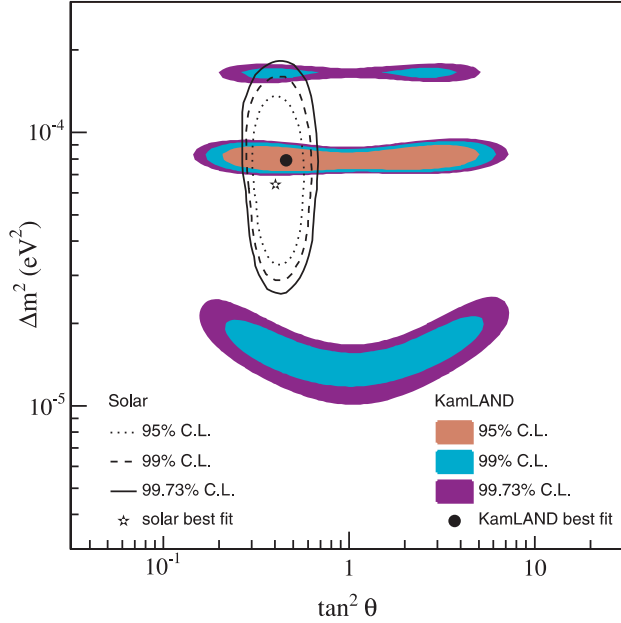


**Figure 1.1:** Allowed regions for neutrino oscillation parameters by KamLAND [27]. The LMA-MSW region of SNO is also shown [28].

Global analysis of solar, atmospheric, long and short baseline neutrino oscillation experiments allow the determination of the elements and phases of the PMNS matrix  $U$  or their limits, respectively. A full review is found in [2].

In the context of this study, it should be mentioned that one can derive

$$\Delta m_{21}^2 = 7.65_{-0.60}^{+0.69} \times 10^{-5} \text{eV}^2 / c^4 \quad (1.15)$$

$$|\Delta m_{32}^2| = 2.4_{-0.33}^{+0.36} \times 10^{-3} \text{eV}^2 / c^4 \quad (1.16)$$

Depending on the unknown value of the lightest neutrino mass, the following mass scenarios are up to now compatible with global neutrino data:

- normal hierarchy:  $m_1 \ll m_2 < m_3$
- inverted hierarchy:  $m_3 \ll m_1 < m_2$
- quasi-degenerate:  $m_1 \cong m_2 \cong m_3$ .

All three scenarios are compatible with the existing constraints on the absolute scale of neutrino masses (Fig. 1.2). Information about the neutrino mass can for example be obtained by measuring the spectrum of electrons near the end point in tritium  $\beta$ -decay experiments. The KATRIN experiment will probe the region of the quasi-degenerate hierarchy with a sensitivity of  $m(\bar{\nu}_e) \leq 0.2 \text{eV}/c^2$  (90% C.L.) [2].

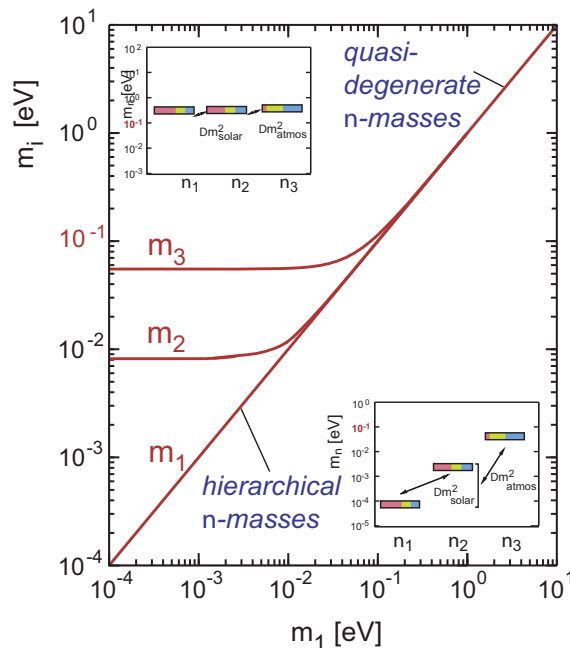


**Figure 1.2:** Mass scale of the neutrino mass eigenvalues, in relation to the smallest mass eigenvalue  $m_1$ . If  $m_1$  is small the mass scale is hierarchical, if  $m_1$  is big, the squared mass differences  $\Delta m^2$  are negligible and the mass scale is quasi-degenerate [30].

## 1.3 Measurement of the neutrino mass

The experimental results of neutrino oscillation measurements yield information on the ratios of the neutrino mass squares, but not on the absolute neutrino masses. With the measurement of one neutrino mass, all others can be derived.

A measurement of the neutrino mass in the sub-eV regime

- determines the fraction of the neutrino mass in the total energy density in the universe. During the big bang,  $10^9$  times more neutrinos than baryons were created. In cosmology, neutrinos contribute to the hot dark matter and make 0.1% to 5% of the total energy density of the universe. This is in the regime of baryonic matter [30].
- determines the values and hierarchy of all mass eigenstates  $m_i$  (Fig. 1.2) together with neutrino oscillation experiments.
- gives insights on the role of neutrinos in the structure formation of the universe [31].
- improves the understanding of supernova explosions [32] [33].
- helps to evaluate theoretical models for the generation of mass, beyond standard model physics.

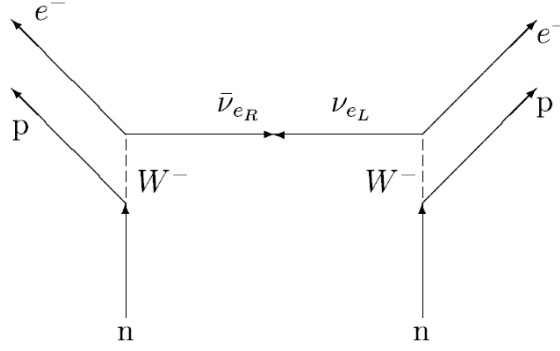


**Figure 1.3: Feynman graph of neutrinoless double beta decay.** Two neutrons simultaneously decay to protons. The right-handed antineutrino emitted from the left vertex is absorbed at the right vertex as a left-handed neutrino. [37]

Two sensitive approaches to measure the neutrino mass in a laboratory exist:

- The search and investigation of neutrinoless double  $\beta$ -decay ( $0\nu\beta\beta$ ), and
- the detailed measurement of the  $\beta$ -electron energy spectrum in case of single  $\beta$ -decay.

In a double  $\beta$ -decay ( $2\nu\beta\beta$ ), two neutrons are simultaneously converted to protons in one decay, while emitting an electron and an electron antineutrino each. The emitted electrons have a continuous energy distribution, as in the case of single  $\beta$ -decay. The double  $\beta$ -decay can only be observed as a second order process of the weak V-A interaction on elements, where the single  $\beta$ -decay is forbidden or strongly suppressed. This limits the available isotopes to 36 (among which are  $^{76}\text{Ge}$  [34],  $^{130}\text{Te}$  and  $^{136}\text{Xe}$  [35]).

Under the assumption that neutrinos are their own antiparticles (Majorana particles [36]) a *neutrinoless* double  $\beta$ -decay is possible. An electron antineutrino emitted at the first vertex is absorbed at the second vertex together with the electron neutrino created there (Fig. 1.3). Therefore, two electrons with a discrete energy are emitted during  $0\nu\beta\beta$ . The right-handed electron antineutrino has to be absorbed as a left-handed electron neutrino. This implies a mixed helicity for the neutrino and therefore a non-zero mass. A change in lepton number of  $\Delta L = 2$  is forbidden according to the standard model.

Due to the long half-life of the available isotopes<sup>4</sup>, either a long measurement time or a large isotopical abundance is necessary. The measurement will only yield a neutrino mass if neutrinos are indeed Majorana particles. The measured value is the effective neutrino mass  $m_{\beta\beta}$  of the sum of coherent mass eigenstates:

$$m_{\beta\beta} = \left| \sum_i U_{ei}^2 m_i \right| = \left| c_{13}^2 c_{12}^2 m_1 + c_{13}^2 s_{12}^2 m_2 e^{i\phi_2} + s_{13}^2 m_3 e^{i\phi_3} \right|. \quad (1.17)$$

---

<sup>4</sup> $T_{1/2} > 1.2 \times 10^{24}$  a for  $^{136}\text{Xe}$  [13]

The CP-violating Dirac-phase  $\delta$  is omitted here. The unknown and CP-violating Majorana-phases  $\phi_i$  are generally complex and can lead to a partial cancellation of  $m_{\beta\beta}$  through the summation over all mass eigenstates [25].

The precise measurement of the  $\beta$ -electron energy spectrum from  $\beta$ -decay (Chapter 2) close to the endpoint yields the neutrino mass by

$$m_\beta^2 = \sum_i |U_{ei}|^2 m_i^2 = |c_{13}^2 c_{12}^2 m_1 + c_{13}^2 s_{12}^2 m_2 + s_{13}^2 m_3|. \quad (1.18)$$

In this incoherent sum, the Majorana-phases disappear and cancellation effects do not occur [25]. The result is independent from the Dirac- or Majorana-nature of the neutrino and other models. Tritium  $\beta$ -decay experiments have been conducted for the past 60 years because tritium

- has the second lowest endpoint energy  $E_0 = 18.6$  keV of all  $\beta$ -sources. This property increases the count rate  $dN/dE \propto (E_0 - E)^2$  in the endpoint region, since  $(1/E_0)^3$  of all  $\beta$ -electrons can be found there,
- has a low half-life of  $T_{1/2} = 12.3$  a which makes high source activities possible,
- has a simple electron configuration, which allows for precise correction of the interactions between emitted electron and daughter nucleus,
- $\beta$ -decay is super-allowed which makes energy corrections of the nuclear matrix element unnecessary [30].

Figure 1.4 shows results from tritium  $\beta$ -decay experiments of the last 20 years. The KATRIN experiment is a next-generation tritium  $\beta$ -decay experiment which will measure the electron antineutrino mass with a sensitivity of  $m(\bar{\nu}_e) \leq 0.2$  eV/ $c^2$  (90% C.L.).

A complementary approach for the direct neutrino mass measurement from  $\beta$ -decay is the *microcalorimeter arrays for a rhenium experiment* (MARE) project [38]. It aims for a sensitivity comparable to the KATRIN experiment. In this case, the  $^{187}\text{Re}$  calorimeters act as both, the detector and the source. Therefore, the systematic uncertainties are fundamentally different to measurements with electrostatic spectrometers. The MARE project uses  $^{187}\text{Re}$  calorimeters, where the full energy from rhenium  $\beta$ -decay (except the energy carried away by the neutrino) is measured from the temperature rise in the detector. However, calorimetric approaches suffer from pile-up effects, since the complete  $\beta$ -spectrum is detected. Therefore, small detectors and a large detector array ( $10^4$  detectors) are required to reach sufficient statistics in the endpoint region of the  $\beta$ -spectrum.

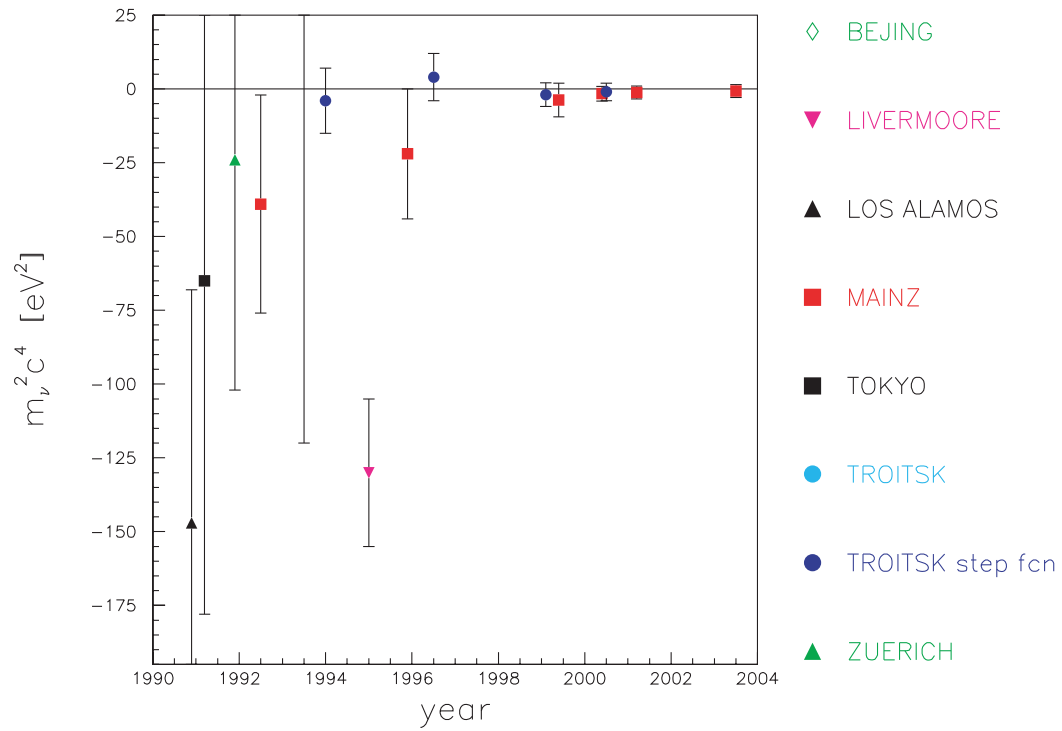


**Figure 1.4: Results on the neutrino mass from  $\beta$ -decay experiments since 1990 [30].** The understanding of systematic errors and improvement of the experimental setup has greatly reduced the uncertainties on the neutrino mass and solved the problem of negative neutrino mass squares.

## 2 The KATRIN experiment

The **K**Arlsruhe **T**Ritium Neutrino Experiment KATRIN aims to determine the neutrino mass with a sensitivity of  $m(\bar{\nu}_e) \leq 0.2 \text{ eV}/c^2$  (90% C.L.). It uses a direct and model-independent approach by the detailed determination of the  $\beta$ -decay spectrum at its endpoint. By measuring the shape of the spectrum at high energies, the neutrino mass can be derived. In the following, the theory, measurement and the basic experimental setup is described. In Section 2.4 the systematic and statistical errors on the observable  $m_\nu^2$  are discussed. Here, it is described how the focal plane detector performance enters the calculation of the systematic and statistical uncertainties on  $m_\nu^2$  prior to the section motivating this thesis.

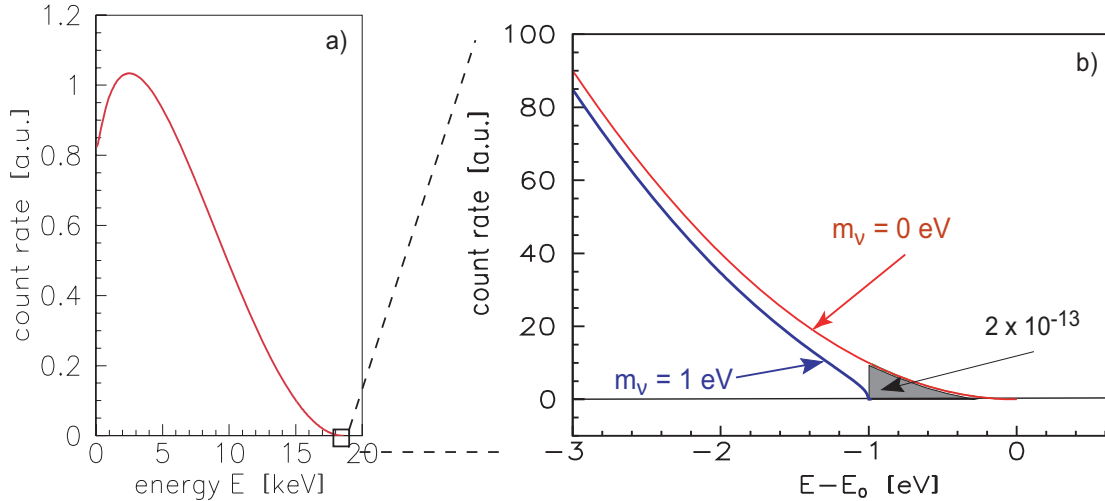


**Figure 2.1: The energy spectrum of tritium  $\beta$ -decay.**

(a) The full energy spectrum. (b) The energy spectrum at the tritium  $\beta$ -decay endpoint  $E_0$ . The lines show calculations for different  $m_\nu$ . Only a fraction of  $2 \times 10^{-3}$  events is found in an energy interval of 1 eV below the endpoint energy  $E_0$  [30].

### 2.1 Theory and measurement principle

During a  $\beta$ -decay, a proton is transformed into a neutron. In the transformation, an electron and an electron antineutrino is emitted

$$(Z, A) \rightarrow (Z + 1, A)^+ + e^- + \bar{\nu}_e. \quad (2.1)$$

## 2 The KATRIN experiment

The nucleus with charge  $Z$  and nucleus mass  $A$  can be regarded as infinitely heavy so that the available kinetic energy is shared between the electron and the electron antineutrino<sup>1</sup>. The  $\beta$ -spectrum is described by Fermi's golden rule

$$\frac{d^2 N}{dt dE} = \frac{2\pi}{\hbar} |M|^2 \rho(E) \quad (2.2)$$

giving the rate  $dN/dt$  in an energy interval  $E + dE$  with a phase space density of  $\rho(E)$  and the transitional matrix element  $M$ . This leads to the following expression [39]:

$$\frac{d^2 N}{dt dE} = A(E) \sqrt{(E_0 - E)^2 - m^2(\bar{\nu}_e) c^4} \Theta(E_0 - E - m(\bar{\nu}_e) c^2) \quad (2.3)$$

$$\text{with } A(E) = \frac{G_F^2 \cos^2 \theta_C}{2\pi^2 \hbar^7} |M^2| F(E, Z + 1) p_e (E + m_e c^2) (E_0 - E) \quad (2.4)$$

$G_F$ :	coupling constant	$\Theta_C$ :	Cabibbo angle
$M$ :	transition matrix element	$E_0$ :	endpoint energy
$p_e$ :	electron momentum	$m_e$ :	electron mass

$F(E, Z + 1)$ : Fermi function

where the Fermi function  $F$  takes into account the Coulomb interactions between the emitted electron and the daughter nucleus. For the super-allowed tritium  $\beta$ -decay,  $M$  does not depend on the energy  $E$ . The influence of the neutrino mass is most significant close to the endpoint energy  $E_0$  (Fig. 2.1 and squareroot term in Eq. 2.4). Only one of  $5 \times 10^{13}$  electrons is found in the last eV. To get sufficient statistics in the endpoint region, the following is required:

- A  $\beta$ -electron source with high intensity,
- spectrometers with very good energy resolution,
- a high-efficiency detector system, and
- a low background rate.

The KATRIN experiment consists of the windowless gaseous tritium source (WGTS), the transport section, the pre-spectrometer and main spectrometer and the focal plane detector. The final setup is shown in Figure 2.2. In the following, the experimental setup of the KATRIN experiment is presented. Special attention is paid to the spectrometers and the focal plane detector since the electromagnetic design and geometry are of importance for Chapter 6. The focal plane detector system is described in detail in Section 3.1.

---

<sup>1</sup>However, the final analysis will include the recoil of the daughter nucleus.

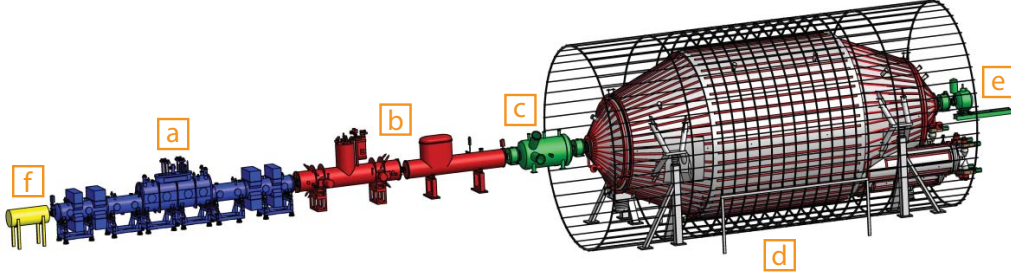


**Figure 2.2: The KATRIN experimental setup [30]:** (a) windowless gaseous tritium source (b) transport section with differential and cryogenic pumping stage (c) pre-spectrometer (d) main spectrometer with air coils (e) focal plane detector (f) rear section.

## 2.2 The source and transport section

The windowless gaseous tritium source (WGTS) is a tube with a length of 10 m and a diameter of 90 mm. Molecular tritium  $T_2$  is injected with a pressure of  $3.35 \times 10^{-3}$  mbar in the middle of the tube with a purity of 95%. Turbomolecular pumps at both ends of the tube create a pressure gradient and collect the remaining tritium, as well as its daughter molecules. The tritium is purified and fed back to the injection valve in a closed circuit. The source tube is completely enclosed by superconducting magnets creating a field of  $B = 3.6$  T. All electrons are emitted isotropically by the tritium  $\beta$ -decay and follow the magnetic field lines towards the ends of the source. They are guided adiabatically towards the rear section, or the spectrometers and focal plane detector. To reach the targeted decay rate of  $9.5 \times 10^{10}/s$ , the tritium column density has to be  $\rho \cdot d = 5 \times 10^{17}$  molecules /  $cm^2$  resulting in a tritium usage of 40 g per day. To keep the systematic error on the neutrino mass measurement below the statistical uncertainty, the column density has to be known by an accuracy of 0.1% [30].

The adjacent transport section (Fig. 2.3) further reduces the tritium flow, coming from the tritium source, from  $1.8 \text{ mbar} \cdot \text{l/s}$  to  $10^{-14} \text{ mbar} \cdot \text{l/s}$  to prevent the introduction of additional backgrounds in the spectrometer and detector section. The differential pumping section (DPS) reduces the tritium flow by a factor  $10^7$  through turbo-molecular pumping. The following cryogenic pumping section (CPS) further reduces the tritium flow by a factor of  $\geq 10^7$  by adsorbing the tritium molecules on a thin layer of argon snow covering its inner walls. The DPS and CPS are both doubly bent by  $20^\circ$  to prevent a direct line of sight from source to detector for neutral molecules.

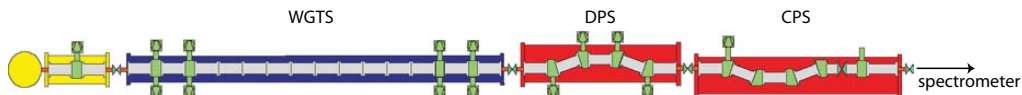


**Figure 2.3: KATRIN components containing tritium [30]** with the windowless gaseous tritium source (WGTS), the differential pumping section (DPS) and the cryogenic pumping section (CPS)

## 2.3 The spectrometer section

A MAC-E filter<sup>2</sup> defines the energy resolution of the KATRIN experiment. Electrons entering the spectrometer are guided along magnetic field lines created by superconducting coils and perform a cyclotron motion with frequency

$$f = \frac{|e|\hbar|\vec{B}|}{2\pi m_e} \sqrt{1 - \left(\frac{v}{c}\right)^2} \quad (2.5)$$

with electron charge  $e$ , electron mass  $m_e$ , electron velocity  $v$  and speed of light  $c$ . The magnetic flux density  $\vec{B}$  decreases by several orders of magnitude from the center of the superconducting coils to the middle of the spectrometer (analysis plane). Assuming adiabatic transition, the transverse energy component  $E_{\perp}$  is changed by

$$\mu = \frac{e}{2m_e} |\vec{l}| = \frac{E_{\perp}}{B} = \text{const.} \quad (2.6)$$

with a constant magnetic moment  $\mu$ . The gradient force

$$\vec{F}_{\nabla} = \vec{\nabla}(\vec{\mu} \cdot \vec{B}), \quad (2.7)$$

reduces  $E_{\perp}$  to a minimum and thereby maximizes the longitudinal energy component  $E_{\parallel}$  in the analysis plane. An electric retarding potential with a maximum in the analysis plane is applied to define which electron energies are transmitted or reflected. The MAC-E filter works as an energetic high-pass filter. Transmitted electrons are re-accelerated to their original kinetic energy and are counted at the focal plane detector. The relative energy resolution is determined by the remaining  $E_{\perp}$  resulting from the ratio of the minimal magnetic field  $B_{\min}$  and the maximum magnetic field  $B_{\max}$  in the analysis plane by

$$\frac{\Delta E}{E} = \frac{B_{\min}}{B_{\max}} \quad (2.8)$$

The normalized transmission function of the MAC-E-Filter with retarding potential

<sup>2</sup>Magnetic Adiabatic Collimation followed by an Electrostatic filter

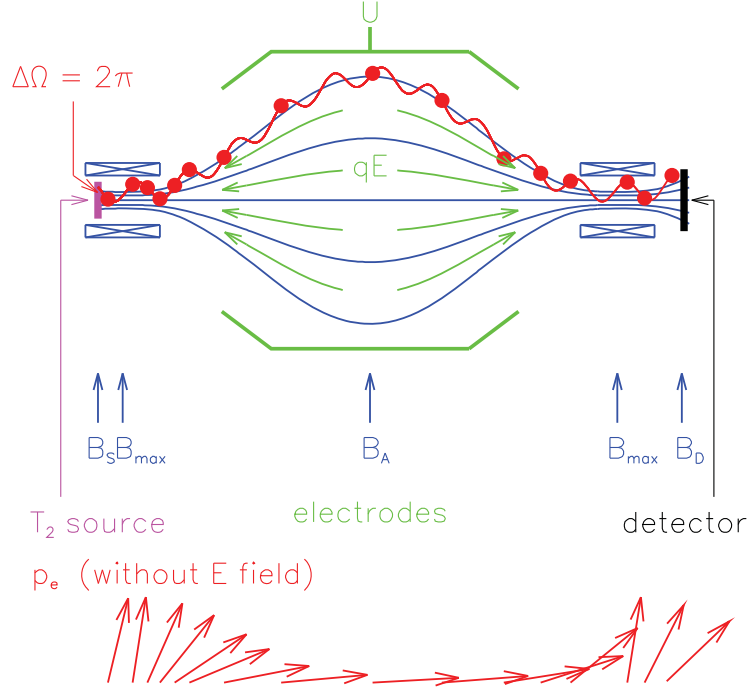


**Figure 2.4: MAC-E filter principle.** The angle between the electron momentum and the magnetic field line is changed by the adiabatic invariance of the magnetic moment  $\mu$  by the inhomogeneous magnetic field (blue lines). The electrostatic retarding potential (green lines) works as an energy high-pass filter [30].

$U$  is analytically given for an isotropically emitting electron source of energy  $E$  by

$$T(E, qU) = \begin{cases} 0 & E - qU < 0 \\ \frac{1 - \sqrt{1 - \frac{E - qU}{E} \cdot \frac{B_S}{B_A}}}{1 - \sqrt{1 - \frac{\Delta E}{E} \cdot \frac{B_S}{B_A}}} & 0 \leq E - qU \leq \Delta E \\ 1 & E - qU > \Delta E \end{cases} \quad (2.9)$$

where  $q$  denotes the electron charge  $e$  [30]. The transmission function is plotted in Figure 2.5.

The KATRIN experiment uses two spectrometers with different sizes (Fig. 2.2). The pre-spectrometer with a diameter of  $D_{PS} = 1.7$  m and energy resolution of  $\Delta E_{PS} \approx 100$  eV is kept at a constant retarding potential  $U_{PS} = 18.3$  kV to cut the low energy part of the spectrum from which no information on the neutrino mass can be derived. It thereby strongly decreases the number the electron in the main spectrometer and reduces background events from secondary electrons produced during inelastic scattering of the  $\beta$ -electrons with residual gas molecules in the spectrometer. Test experiments with the pre-spectrometer are described in Section 3.2.

Electrons transmitted by the pre-spectrometer enter the subsequent main spectrometer with an inner diameter of  $D_A = 9$  m and a length of 23 m. With a magnetic

field of  $B_A = 3 \times 10^{-4} \text{ T}$  at the analysis plane and an area of  $A_A = 63.6 \text{ m}^2$ , it is able to fit a magnetic flux tube of

$$\Phi = \int B dA = B_{\max} \cdot A_{B_{\max}} = B_A \cdot A_A = 191 \text{ T} \cdot \text{cm}^2. \quad (2.10)$$

With a maximum magnetic field of  $B_{\max} = 6 \text{ T}$ , it reaches an energy resolution of  $\Delta E_{\text{MS}} = 0.93 \text{ eV}$ .

As mentioned before, collisions of electrons with residual gas molecules can lead to background events. Therefore, both spectrometers have to comply with ultra high vacuum (UHV) standards to reach a residual gas pressure of  $p < 10^{-11} \text{ mbar}$ .

A further source for background events are low-energy electrons induced by cosmic-ray interactions with the spectrometer walls. To prevent these electrons from entering the main spectrometer, a low-mass wire electrode is installed on the vessel walls. Held at a more negative electric potential, it reflects the electrons emitted from the walls. Additionally, the electrode is segmented and can be used to fine-tune the electric field. The earth magnetic field as well as stray fields from magnetic materials are compensated by air coil systems surrounding the main spectrometer.

## 2.4 Systematic and statistical uncertainties

Table 2.2 lists the known sources for systematic errors on the KATRIN neutrino mass measurement. While the quadratic sum of these errors amount to  $\sigma_{\text{sys,tot}} \approx 0.01 \text{ eV}^2$ , the total systematic uncertainty is anticipated to be

$$\sigma_{\text{sys,tot}} \leq 0.017 \text{ eV}^2 \quad (2.11)$$

to account for unidentified sources of systematic errors. This number is the quadratic sum of five systematic uncertainties  $\Delta m_\nu^2 = 0.0075 \text{ eV}^2$  [30].

The transmission function in Eq. 2.9 is a property of the spectrometer, only determined by the magnetic fields at the tritium source and in the analyzing plane. To take into account inelastic electron scattering with  $\text{T}_2$  molecules in the gaseous source, a response function  $f_{\text{res}}$  is defined through the folding of the corresponding inelastic cross section with the transmission function. The response function for a spectrometer energy resolution  $\Delta E_{\text{MS}} = 0.93 \text{ eV}$ , a maximum accepted starting angle of  $\theta_{\max} = 50.77^\circ$  and a tritium column density  $\rho d = 5 \cdot 10^{17} / \text{cm}^2$  in the tritium source is shown in Fig. 2.5. A region of 10 eV below the endpoint is an elastic plateau. The influence of one, two and threefold scattering is visible in the next 40 eV.

Since the response function is crucial for the KATRIN sensitivity on  $m_\nu^2$  and the inelastic cross sections have an uncertainty of 2%, the response function will be determined in a pre-measurement and the fluctuations of  $\rho d$  will be monitored during

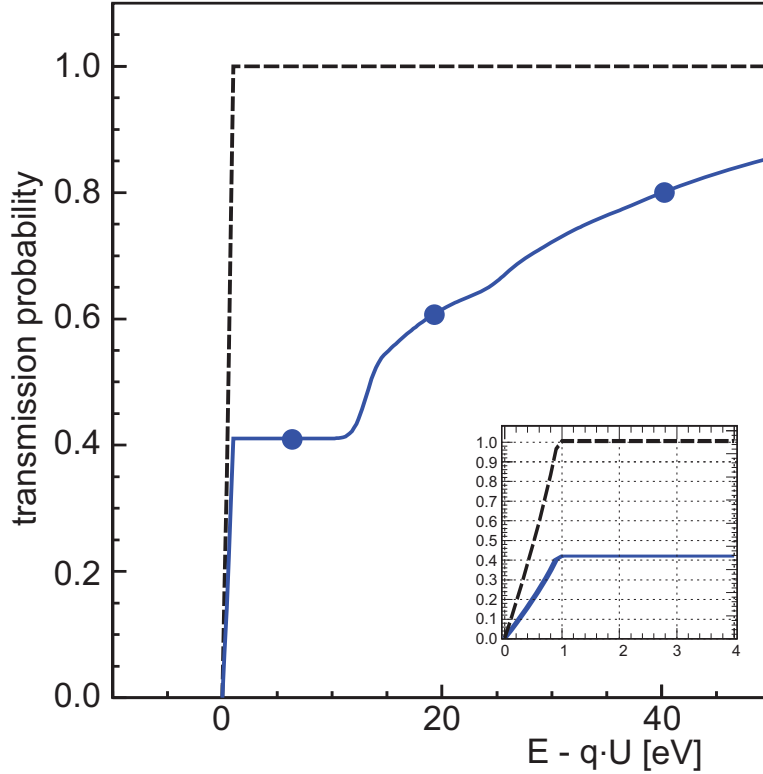


**Figure 2.5: Transmission and response function.** The transmission functions for an electron, depending on the difference of electron energy  $E$  and retarding potential  $U$ , with (blue line) and without (black dashed line) inelastic scattering in the tritium source (Sec. 2.2) is shown [40, 30]. The blue dots are proposed measurement points to prevent unaccounted for systematic uncertainties of the response function [30].

tritium measurements. For the pre-measurements, electrons are injected at the rear of the tritium source (rear section, Fig. 2.2) towards the main spectrometer. This measurement is done for an empty source to determine the transmission function and with a source filled with tritium at various values of  $\rho d$  to determine the response function (Fig. 2.5). During neutrino mass measurements, the column density is monitored by the forward beam monitor detector (Sec. 3.3).

Electrons transmitted by the main spectrometer are detected with the focal plane detector system (FPD, Sec. 3.1). No systematic uncertainty arising from angular or energy dependent detection efficiencies are considered in Table 2.2. To extend the list and determine the magnitude of possible systematic uncertainties arising from the focal plane detector, the response to low-energy electrons has to be investigated taking into account the electromagnetic design of spectrometer and detector region.

The statistical error after a three year measurement time is calculated as

$$\sigma_{\text{stat}} = 0.018 \text{ eV}^2 \quad (2.12)$$

when using the parameters listed in Table 2.1 [30]. One of these parameters is the

## 2 The KATRIN experiment

absolute focal plane detector detection efficiency  $\varepsilon = 0.9$ . The detection efficiency depends on background and noise contributions as well as backscattering and dead layer effects. To further optimize the KATRIN measurement cycle, the detector efficiency is investigated in Section 6.2.2.

Adding Eqs. 2.12 and 2.11 quadratically, leads to a total uncertainty of  $\sigma_{\text{tot}} \approx 0.025 \text{ eV}^2$ . Assuming a vanishing neutrino mass  $m_\nu = 0$ , this uncertainty translates into an upper limit  $L(90\% \text{ C.L.})$ , which is connected to the error on  $m_\nu^2$  via  $L(90\% \text{ C.L.}) = \sqrt{1.64 \cdot \sigma_{\text{tot}}}$ . After three years of measuring time, this limit becomes

$$m(\nu_e) < 0.2 \text{ eV} \quad (90\% \text{ C.L.}) \quad (2.13)$$

with no finite neutrino mass being observed. This sensitivity improves the existing limits by more than one order of magnitude [30].

**Table 2.1:** Reference parameters used to calculate the statistical error on  $m_\nu^2$  [30].

parameter	value
column density	$\rho d = 5 \cdot 10^{17} \text{ cm}^{-2}$
analysing plane	$A_A = (\pi \cdot 450^2) \text{ cm}^2 = 63.6 \text{ m}^2$
source cross section	$A_S = (\pi \cdot 4.11^2) \text{ cm}^2 = 53 \text{ cm}^2$
magnetic field strengths	$B_S = 3.6 \text{ T}, B_{\text{max}} = 6 \text{ T}, B_A = 3 \cdot 10^{-4} \text{ T}$
Tritium fraction in the source	0.95
maximum opening angle	$\theta_{\text{max}} = 50.77^\circ$
Tritium endpoint energy	$E_0 = 18575.0 \text{ eV}$
energy resolution	$\Delta E/E = 1/20000 = 0.93/18575$
zero-loss probability	$P_0(\rho d, \theta_{\text{max}}) = 0.413$
background rate per interval $U$	$\Gamma_b = 0.01 \text{ s}^{-1}$
detection efficiency	$\varepsilon = 0.9$

**Table 2.2:** Summary of sources of systematic errors on  $m_\nu^2$  and the individual effect on  $m_\nu^2$  for an analysis interval of  $[E_0 - 30 \text{ eV}, E_0 + 5 \text{ eV}]$  if not stated otherwise (for details see individual chapters in Section 11 in [30]).

source of systematic shift	systematic shift $\sigma_{\text{syst}}(m_\nu^2)[10^{-3} \text{ eV}^2]$
description of final states	< 6
$T^-$ ion concentration $n(T^-)/n(T_2)$	< 0.1
unfolding of the energy loss function (determination of $f_{\text{res}}$ )	< 6
monitoring of $\rho d$ $[E_0 - 40 \text{ eV}, E_0 + 5 \text{ eV}]$	< 1.5
background slope	< 1.2
HV variations	< 5
potential variations in the source	< 0.2
magnetic field variations in source	< 2
elastic $e^- - T_2$ scattering	< 5
<b>identified syst. uncertainties</b>	$\sigma_{\text{syst,tot}} = \sqrt{\sum \sigma_{\text{syst}}^2} \approx 0.01 \text{ eV}^2$



# 3 Detector systems of the KATRIN experiment

Main objective of this work has been the development of a simulation package (*KESS*) to precisely describe the detector response of silicon semiconductor detectors to low-energy electrons. Besides the physics of the interactions of electrons with matter, the detector response is also determined by detector properties like its electromagnetic environment, dead layer configuration and electronic readout performance.

In this chapter, three different silicon detector systems are described, which will be installed at the KATRIN experiment. The parameters mentioned before vary considerably for these three systems. As it will be shown in Chapter 6, the requirements were met that *KESS* can be applied to all cases with high precision.

The focal plane detector (FPD, Sec. 3.1) system contains a large, monolithic, 148-pixel detector, based on PIN diode technology. It will detect the highest-energy tritium  $\beta$ -decay electrons from the windowless gaseous tritium source (WGTS), transmitted by the spectrometer section. The focal plane detector is regarded as one of the key components of the KATRIN experiment. Its dedicated calibration system [41] is also discussed. Data from the commissioning of the focal plane detector are compared to simulations later in this study (Sec. 6.1.1).

A predecessor of the focal plane detector, using the same detector technology is installed at the pre-spectrometer test setup (Sec. 3.2) [42, 43]. The experimental setup consists of an adjustable mono-energetic electron source, the pre-spectrometer and the 64-pixel PIN diode (SPD). Pre-spectrometer measurements of the transmission properties at high electron surplus energies are compared to simulations in Section 6.2.1, thus, the pre-spectrometer test setup is also presented.

The third detector system is the forward beam monitor detector (FBMD, Sec. 3.3) [44]. It is a movable detector with a sub-mm<sup>2</sup> area and will be installed at the tritium-free end of the cryogenic pumping section. During neutrino mass measurements, it is used to monitor the source activity precise to a  $10^{-3}$  level. Since it is exposed to the complete  $\beta$ -spectrum, rates up to  $10^5$  counts per second (cps) have to be processed. Experimental results and simulations including the modeling of the signal amplification chain and data acquisition system are shown in Section 6.1.2.

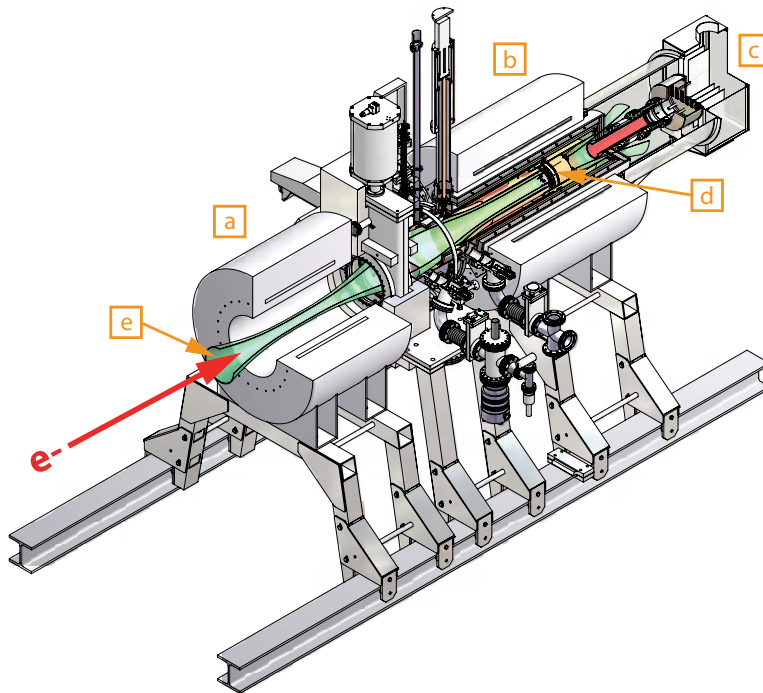


**Figure 3.1:** Drawing of the focal plane detector system with (a) the pinch magnet ( $B_{\text{pin}} = 6 \text{ T}$ ), (b) the detector magnet ( $3 < B_{\text{det}} < 6 \text{ T}$ ), (c) front-end electronics, (d) the detector wafer, feedthrough flange and first amplification stage, and (e) the magnetic flux tube, shown in green.

### 3.1 The focal plane detector system

Electrons transmitted by the spectrometers are detected by the focal plane detector (FPD) system. The heart of the system is a monolithic 148-pixel silicon PIN diode. The system is equipped with two superconducting magnets, the pinch magnet with a field of  $B_{\text{pin}} = 6 \text{ T}$  and the detector magnet with  $3 \text{ T} \leq B_{\text{det}} \leq 6 \text{ T}$  (Fig. 3.1). The silicon wafer is placed near the center of the detector magnet. It fulfills the geometric requirements from Eq. 2.10 with a sensitive area of  $A_{B_{\text{det}}} = 64 \text{ cm}^2$ .

Generally, segmented silicon PIN diodes offer the following advantages:

- large sensitive area,
- good sensitivity ratio between electron and gamma incident
- low background and low noise,
- silicon is suitable for ultra high vacuum conditions and
- mounting and connection techniques can be optimized with regard to vacuum and low background requirements.

The segmentation (Fig. 3.2) reflects the radial symmetry of the KATRIN experi-

ment. It is therefore possible to relate the recorded energy spectra of each pixel to areas of the flux tube and thereby to areas of the analyzing plane and the tritium source. Possible inhomogeneities in electric and magnetic fields, sources of background, and inhomogeneities in the source can be identified. All pixels have the same area of  $44.1 \text{ mm}^2$  to ensure similar noise behavior, which is mainly given by the input capacitance of the pixel.

18 keV electrons interact with the silicon detector in the first few  $\mu\text{m}$  only. Despite this fact, the detector thickness was chosen to be  $500 \mu\text{m}$  [30]. This thickness is a trade-off between increasing intrinsic detector background and decreasing energy resolution due to lower electronic noise by a lower input capacitance into the readout electronics. Furthermore, a  $500 \mu\text{m}$  wafer provides sufficient mechanical stability to withstand the pressure of  $\sim 160$  spring-loaded pogo-pins. These are used for the readout connection, while the detector is only fixed at its circumference. This unique wafer mounting relinquishes the need for any substrate and is mandatory to meet the radiopurity requirements for KATRIN.

To achieve the statistical uncertainty for the neutrino mass measurement within the planned running time, a detection efficiency of 90% is required [30]. Additionally, the intrinsic detector background is allowed to be  $10^{-3}$  cps. To meet these requirements the detector has the following design properties:

- An energy resolution  $\Delta E_{\text{FWHM}} = 600 \text{ eV}$  (FWHM<sup>1</sup> at  $E = 18.6 \text{ keV}$ ),
- low natural radioactivity of all used materials,
- spatial separation of 'hot' materials (e.g. ceramic substrate),
- passive shielding, and
- an active veto system to account for cosmically induced events.

The passive shielding is a 5 cm layer of low-activity copper installed between the detector wafer and the stainless steel vacuum chamber [46]. It stops the decay products of natural radioactivity from reaching the detector. Inside the copper shielding, an active veto system made of plastic scintillator is installed. Passing particles create scintillation light, which is collected by wavelength-shifting fibers. They are read out by multi-pixel photon counters. Measurement intervals following an active veto event can be removed for the analysis.

During neutrino mass measurements, incoming electrons are in the energy range  $18.3 \text{ keV} \leq E \leq E_0 \approx 18.6 \text{ keV}$  with a rate of a few electrons per minute. During calibration runs, the spectrometer potential is lowered further. Average rates up to 100 kHz can be processed by the focal plane detector and its data acquisition system (DAQ) without losses in efficiency.

The 148-pixel silicon PIN diode consists of a  $n^{++}$ -doped entrance side and a  $p^{++}$ -doped read-out side, separated by a  $n$ -intrinsic wafer. No metalization layer is

---

<sup>1</sup>Full Width at Half Maximum

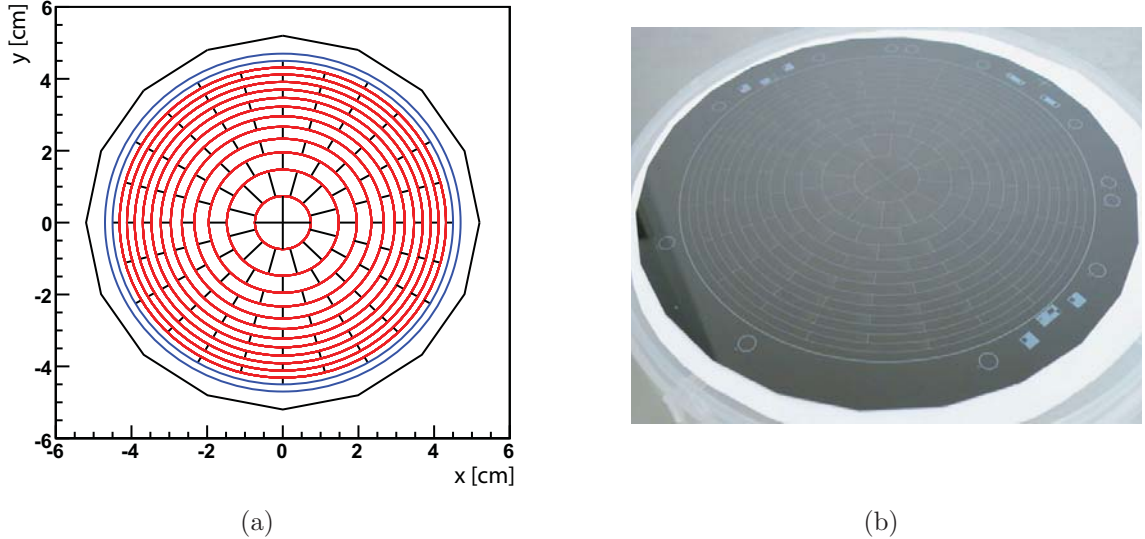


**Figure 3.2:** The segmentation of the focal plane detector into 148-pixels with the same size is shown (a) as a drawing and (b) as a photography of the backside of an actual detector wafer [45].

applied to obtain a maximum detection efficiency for electrons. The entrance side is homogeneous, while the segmentation is applied at the readout side by  $p^{++}$  pads (Fig. 3.2). Each pixel has a size of  $44.1 \text{ mm}^2$  and a leakage current  $I_{lc} \ll 0.1 \text{ nA}$  at  $T = -100^\circ\text{C}$ . The readout pads are contacted by spring-loaded pogo pins to pick up the signal. It is then transported from the ultra-high-vacuum region to a medium-vacuum region through a feedthrough flange. Here, the pre-amplifiers pick up and process the signal. The signal chain continues into ambient air to digitizer boards. Finally, the signal is transported over optical fibers to the ADC (analog-to-digital conversion) readout-boards.

The pre-amplifier modules are designed in a classical, charge-sensitive configuration with a low-noise field-effect transistor ( $2 \text{ nV}/\sqrt{\text{Hz}}$ ) matching the input capacitance. The electronic readout is designed such that parallel and serial noise sources contribute equally. In practice, energy resolutions of  $1.5 \text{ keV}$  are achieved routinely. The signals from the pre-amp are transmitted via an optical transmitter/receiver board to the DAQ system. The DAQ samples each channel with  $20 \text{ MHz}$  and  $12 \text{ bit}$  ADC resolution. Through the configuration of field programmable gate arrays (FPGA), the user can choose to readout

- the signal trace with a time interval of  $\pm 50 \mu\text{s}$  around a signal trigger (for rates up to  $350 \text{ Hz}$ ),
- the energy output by application of a trapezoidal filter with selectable length (for rates up to  $120 \text{ kHz}$ ) or
- or energy histograms (for rates  $> 120 \text{ kHz}$ ).

To perform frequent energy calibrations, a  $\gamma$ -source and an electron emitter are available. Both can be inserted automatically into the beam tube in front of the detector and illuminate the full focal plane detector surface. As a  $\gamma$ -source,  $^{241}\text{Am}$  is used. The electron emitter is a large copper disc, which can be put on negative electrostatic potential. It can be irradiated with ultraviolet light from an array of LEDs, installed outside of the detector chamber. Electrons are emitted from the disc by the photoelectric effect. They are accelerated along the magnetic field lines towards the detector, which is held at a more positive potential. The potential difference defines the kinetic energy of the electron. Since the electric field between the two only affects the longitudinal energy component, incident angles at the detector are small and can be considered as being perpendicular to the detector surface. By measuring the current emitted from the disc with picoampere precision, an absolute measurement of the detection efficiency of the focal plane detector is possible [41].

A post-acceleration electrode is available, which optionally increases the kinetic energy of the  $\beta$ -electrons by up to 30 keV. Thereby, the energy region of interest can be shifted to an optimal energy interval with low intrinsic background. The detector background was determined by detailed Monte Carlo investigations [46] and will be measured. The post-acceleration only affects the longitudinal kinetic energy component of the electron  $E_{\parallel}$  and can therefore decrease the backscattering coefficient through smaller incident angles and higher incident energies (Sec. 5.2.1 and Fig. 5.3).

## 3.2 The pre-spectrometer test experiment

The pre-spectrometer (PS) test experiment serves a twofold purpose. It is a testbed for the electromagnetic design configuration of MAC-E filters and ensures the pre-spectrometer will perform as expected in the final KATRIN beam line setup (Sec. 2.3). This includes the adiabatic transmission of electrons. Transmission functions have been measured and confirmed its function as a MAC-E filter [47, 48, 49]. As it will be shown in detail in Section 6.2.1, it is mandatory to include a model describing the electron backscattering from the silicon detector, which is available with the simulation created during this study. Only then, it is possible to analyze the transmission function in detail.

### 3.2.1 Experimental setup

The experimental setup basically consists of a movable electron source, the spectrometer itself and a detector system (Fig. 3.3) [48, 49]. The magnetic field guiding the electrons is created by two superconducting coils which are 4.3 m apart. Each solenoid reaches a maximal central field of  $B_{\text{max}} = 4.5$  T when applying a current of 156 A. The magnetic field in the analyzing plane is  $B_{\text{A}} = 0.016$  T.

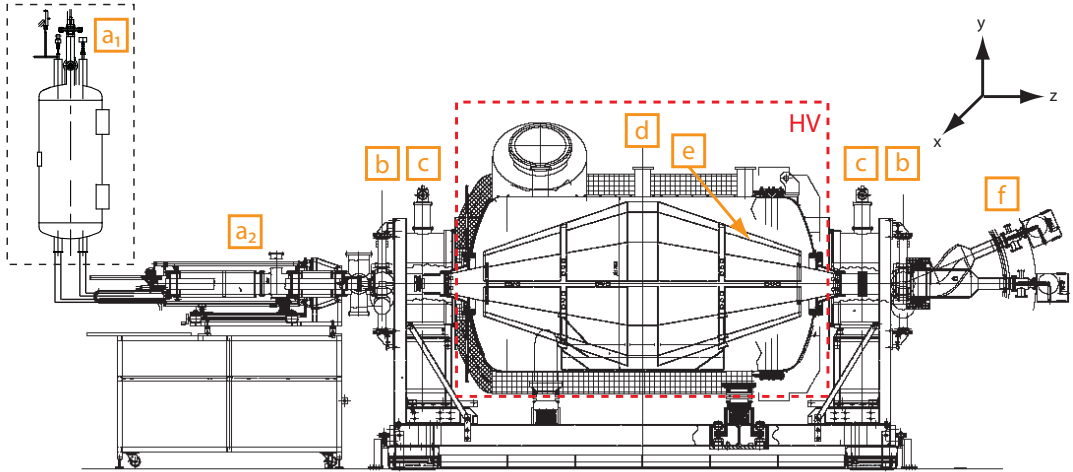


**Figure 3.3: The KATRIN pre-spectrometer test experiment.** The red dotted line shows the boundary between ground potential and high voltage. **(a<sub>1</sub>)** Liquid nitrogen dewar (not to scale), **(a<sub>2</sub>)** detector chamber, **(b)** DN200 valves, **(c)** superconducting coils, **(d)** analyzing plane, **(e)** inner electrode, and **(f)** electron source (e-gun).

The electrostatic retarding potential  $U$  is applied to a system of inner electrodes and the spectrometer vessel itself.  $U$  is primarily created by the vessel potential and its shape can be finely tuned by the inner electrodes. While the nominal potential is  $U_{\text{PS}} = -18.3 \text{ kV}$ , the electrode system is designed for potentials up to  $-35 \text{ kV}$ .

An electron source (e-gun) provides electrons with kinetic energies  $1 < E < 30 \text{ keV}$  for measurements of the electromagnetic properties of the pre-spectrometer [50]. Electrons are emitted from a thin gold layer via photoelectric effect by illuminating the backside with ultraviolet light. The gold layer is held at the desired negative potential while the electrons are accelerated towards an electrode on ground potential. The ground electrode has a hole in its middle through which the electrons are guided by the magnetic field. The absolute potential difference between the gold layer and the ground electrode therefore defines the kinetic electron energy with an uncertainty in energy of a few eV. To inject electrons in different areas of the flux tube, the e-gun is movable in the  $x$ - $y$ -plane.

Electrons yielded from the gold have a maximum initial kinetic energy of  $E \approx 2 \text{ eV}$ , obtained from the difference of the maximum photon energy and the gold work function. This energy is split into a transversal and longitudinal energy component. The initial angular distribution can be approximated by a polar angle  $\theta = \arcsin(R)$  and an azimuthal angle  $\phi = 2\pi R$  with a uniformly distributed random number  $R \in [0, 1]$  [51, 52]. The electrostatic potential between the gold layer and the ground blind mainly affects the longitudinal component, since the guiding center of the electron follows the magnetic field lines. Therefore, after leaving the e-gun, large angles between the electron energy vector and the magnetic field line are rare [50].

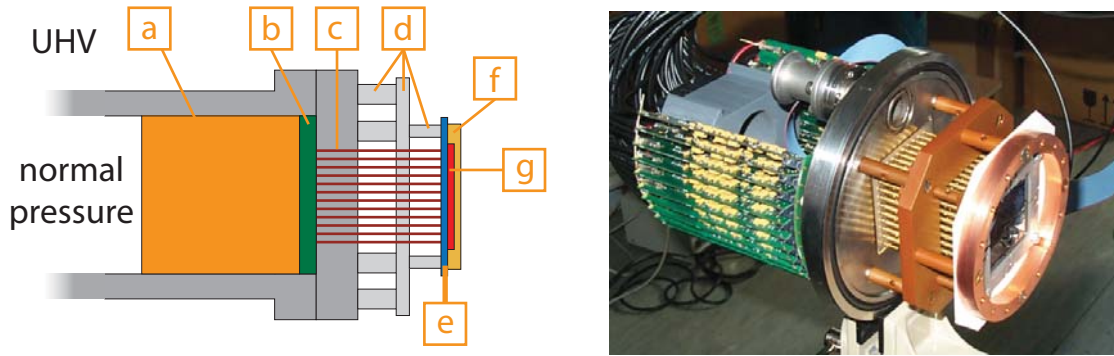


**Figure 3.4: The schematic and completed setup of the pre-spectrometer detector.**

(a) 32 radially arranged circuit boards each with two low-noise pre-amplifiers on ambient side, (b) distribution board, (c) DN 100 feedthrough flange, (d) mounting structure made of DuPont VESPEL S3, (e) ceramics with the first JFET amplification stage, (f) copper cooling ring, and (g) detector wafer

### 3.2.2 The pre-spectrometer detector system

While the pre-spectrometer test experiment is a testbed for electromagnetic design configurations of MAC-E filters, its detector system was also a proof-of-principle experiment for the focal plane detector (Sec. 3.1), as similar detector technologies were used.

The heart of the pre-spectrometer detector system is a quadratically segmented silicon PIN diode with 64 pixels of equal size and an overall sensitive area of  $16 \text{ cm}^2$ . The most important properties of the segmented PIN diode (SPD) and the focal plane detector are given in table 3.1. Its wafer material is manufactured with the same processing technique as the focal plane detector. Therefore, the entrance window is an unsegmented  $n^{++}$  layer in a  $n$ -doped wafer. The readout pads for segmented readout are  $p^{++}$ -doped and are applied on the backside of the detector wafer.

The segmented PIN diode is here glued to an  $\text{Al}_2\text{O}_3$  ceramic, which is cooled by a copper ring in contact with a closed liquid nitrogen circuit. The operating temperature of the segmented PIN diode is  $-60^\circ\text{C}$ . The first signal amplification stage of 64 JFETs is mounted on the backside of the ceramic. The circuit on the ceramic is contacted by spring loaded pogo-pins and the signal is transmitted to the normal pressure region through a feedthrough flange. It is then processed by an array of low-noise amplifiers in source-follower configuration.

The detector properties important for the comparison of modeled and measured detector responses (Sec. 6.2.1) are the energy resolution  $\Delta E_{\text{FWHM}}$  and the dead layer thickness. The energy resolution was found to be dominated by the signal noise

and therefore independent of the incident energy in the interval relevant for the pre-spectrometer test setup. The average over all pixels was measured to be  $\Delta E_{\text{FWHM}} = 4.4$  keV for photons [53, 43]. The dead layer was measured as  $\lambda_{\text{CSDA}} = 119$  nm [54]. Due to the usage of ceramic materials in the proximity of the detector and the absence of passive shielding, the intrinsic detector background is  $20.3 \times 10^{-3}$  cps [53].

Further details on the detector system and the pre-spectrometer test setup can be found in [53, 42, 43, 48, 47, 49].

**Table 3.1: Comparison of focal plane detector and segmented PIN diode design properties.** The segmented PIN diode system has a lower sensitive area and is not optimized for background reduction or energy resolution. For the focal plane detector, the quoted intrinsic background is given for an energy interval of 15.9-19.4 keV, for the segmented PIN diode it is 15-22 keV.

parameter	focal plane detector	segmented PIN diode
$\Delta E_{\text{FWHM}}$ at 18.6 keV [keV]	1.5	4.4
dead layer $\lambda_{\text{CSDA}}$ [nm]	110	110
wafer thickness [ $\mu\text{m}$ ]	500	200
geometry	circle	square
sensitive area [ $\text{cm}^2$ ]	64	16
number of pixel	148	64
pixel size [ $\text{mm}^2$ ]	44.1	25
pixel capacity [pF]	9	16
leakage current [ $\text{nA}/\text{cm}^2$ ]	0.2	0.2
intrinsic background [cps]	$1 \times 10^{-3}$	$20.3 \times 10^{-3}$
active/passive veto	yes	no
movable in x,y [cm]	no	$\pm 2$
movable in z [cm]	no	50

## 3.3 The forward beam monitor detector system

### 3.3.1 Area of application

In Section 2.4, the importance of the KATRIN response function is outlined. Since its shape is strongly dependent on the tritium source column density  $\rho d$  and the uncertainties of the theoretical description are too large, the column density  $\rho d$  will be measured in regular intervals.

Between neutrino mass measurements, a rear electron gun is used to shoot electrons through the tritium source towards the spectrometer region. With three different values for the difference between electron energy and retarding potential  $E - qU_R$ , the column density can be measured with a  $10^{-3}$  precision once the energy loss function is known in advance from another measurement [30]. The proposed energies at which the response function will be measured are  $E - qU = 7, 20$  and  $40$  keV (Fig. 2.5). This measurement is repeated regularly to prevent unaccounted for systematic uncertainties of the response function.

Due to the significant contribution of the response function, and thus  $\rho d$ , to the total systematic error on  $m_\nu^2$ , a detector system is proposed to monitor the activity of the source permanently.

Monitoring  $\rho d$  with a  $10^{-3}$  precision over long time scales of weeks calls for a detailed understanding of the detector response. For example, how buildups of dead layers over time can change the detector response. Therefore, the forward beam monitor detector is another detector system relying on systematic investigations of its performance by detailed simulations of the detector response.

The column density  $\rho d$  can be expressed through the  $T_2$  isotopical content  $\epsilon_T$  and the source activity  $A$  by

$$A = \epsilon_T \rho d \quad (3.1)$$

which can be measured independently.

To prevent interruptions of the neutrino mass measurements, a continuous monitoring system is being developed using a small and movable silicon detector, the forward beam monitor detector (FBMD) [44]. It is situated in a tritium free environment at the end of the cryogenic pumping section just before the pre-spectrometer (Fig. 2.2). The complete  $\beta$ -spectrum is available at this position in the KATRIN beam line. This allows for high statistics and short measuring intervals of the source activity.

During neutrino mass measurements, the detector is placed at the outer edge of the flux tube and will not affect the measurement. The forward beam monitor detector system is movable, which allows the measurement of the  $\beta$ -spectrum for each part of the flux tube.

The second part of the monitoring procedure is the continuous measurement of the isotopical content of the tritium gas  $\epsilon_T$ . This will be determined by Laser Raman spectroscopy at the inner loop inlet (see [30, 55]).

#### 3.3.2 Experimental setup

The forward beam monitor detector (FBMD) will be placed in the outer flux tube at the end of the cryogenic pumping section. The magnetic field at this position is  $B = 1.18$  T which, following Eq. 4.2, corresponds to a maximum incident angle of  $\theta_I = 18.8^\circ$ . The forward beam monitor detector will see the complete  $\beta$ -spectrum

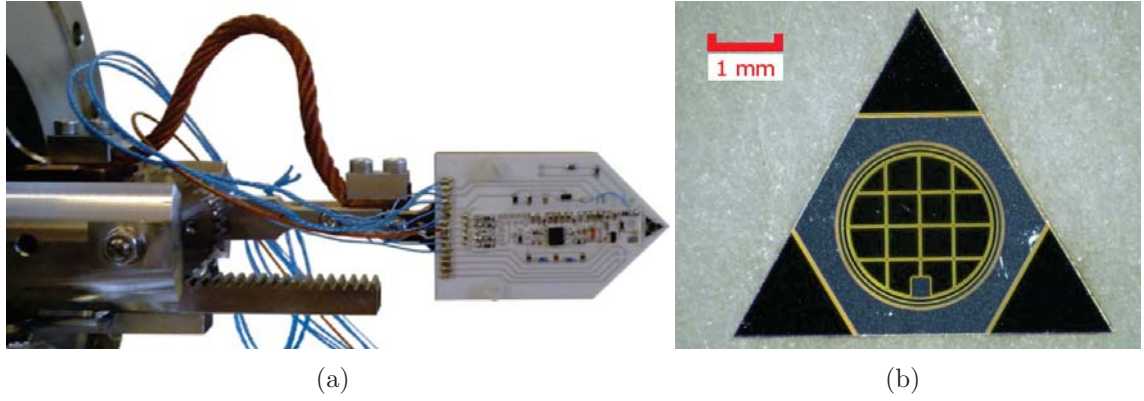


**Figure 3.5: Photographs of the forward beam monitor detector system [40]. (a) The silicon PIN diode is mounted to a prototype pre-amplification board and attached to the manipulator (b) The silicon PIN diode.**

with an intensity of  $1.6 \cdot 10^6 / (\text{s} \cdot \text{mm}^2)$ . To account for this high rate and the limitations by DAQ systems, the detector will have an area of the order of  $0.1 \text{ mm}^2$ .

In addition to the position in the outer flux tube during neutrino mass measurements, the forward beam monitor detector is able to scan each point of the magnetic flux tube in the plane perpendicular to the beamline axis. The detector and the first amplification stage is mounted to a manipulator, which allows a reproducible positioning accuracy of  $50 \mu\text{m}$  [44]. The manipulator, electronics and detector have to fulfill the outgassing requirements for the ultra-high-vacuum conditions inside the beam line.

Two options for the detector technology were evaluated [40]. One was a silicon drift detector (SDD) based on sideways depletion. The second was the standard PIN diode design (Fig. 3.5).

The silicon drift detector has a thickness of  $300 \mu\text{m}$  and is made of n-doped silicon. The entrance side is completely  $\text{p}^+$  doped. The readout side is composed of multiple rings of  $\text{p}^+$  alternating with the n doped bulk material. A depleted p-channel field-effect transistor (DEPFET) is sitting in the center of the readout side.

The  $\text{p}^+$  rings are supplied with more negative voltages from the detector edge to its center, thereby depleting the detector from free charge carriers. A second potential between entrance- and readout side shifts the absolute potential minimum to the readout side. The potentials are chosen so that the gate of the DEPFET is equal to the absolute potential minimum in the detector and all charge carriers are collected.

Silicon drift diodes offer a superior energy resolution since the first FET amplification stage is built into the silicon wafer. Additionally, the charge carriers are directly converted to a voltage signal. Two disadvantages are the rather complicated design for the detector electronics and the need to clear the JFET from the collected electrons in a constant time interval. The silicon drift diode has a design dead layer of

### 3.3 The forward beam monitor detector system

$\lambda_{\text{CSDA}} = 100 \text{ nm}$  [40] and an average energy resolution measured in a test setup of  $\Delta E_{\text{FWHM}} = 780 \pm 140 \text{ eV}$  for x-rays [40].

The PIN diode has a thickness of  $140 \mu\text{m}$  with a standard design. It can be operated with straight-forward electronics and due to its small size it offers a good energy resolution. The PIN diode has a design dead layer of  $\lambda_{\text{CSDA}} = 100 \text{ nm}$  and the average energy resolution was measured to be  $\Delta E_{\text{FWHM}} = 1439 \pm 31 \text{ eV}$  for x-rays [40].



## 4 Monte Carlo simulations of keV electrons in solids

The scope of this study is the detailed modeling of the response of silicon semiconductor detectors to  $\beta$ -decay electrons. The detection efficiency of the focal plane detector has a direct impact on the systematic and statistical errors on  $m_\nu^2$ , which are not included in full detail in the current treatment of uncertainties. Due to the electromagnetic fields in the spectrometer and focal plane detector region, it is necessary to model backscattering and dead layer effects precisely. Then it is possible to determine changes in the relative efficiency with regard to various detector parameters at the  $10^{-3}$  level.

After evaluating available simulation packages and understanding their shortcomings, a specialized Monte Carlo simulation (**KESS**<sup>1</sup>) was written. It is derived from first principles and is able to fulfill the requirements. The simulation was evaluated against published experimental data and data acquired with different detectors at KATRIN test experiments during their commissioning phases. Since good agreement with the experimental data is found, further parameters can be derived from the simulated energy spectra. The created simulation was embedded into the global KATRIN simulation framework **Kassiopeia**. Together with additional simulation packages for electromagnetic tracking of electrons available in **Kassiopeia**, it is possible to model more complex and complete experimental setups (i.e. the pre-spectrometer test experiment, and the final KATRIN beamline setup of the main spectrometer and the focal plane detector). These simulations verified and explained experimentally observed effects, and allowed the estimation of systematic and statistical errors on  $m_\nu^2$  measured with KATRIN (Sec. 6.2.2).

In this chapter, the need for detailed detector response simulations is motivated in Section 4.1.2 by a possible energy dependent detection efficiency. The continuous-slowing-down-approximation is shown to be insufficient in Section 4.1.3. Additionally, the limitations of the well known Bethe formula at low energies are discussed. To precisely model the interactions, including energy loss and angular changes of the electrons in the silicon crystal, event-based Monte Carlo simulations describing each collision are the most promising approach. The available and widely used simulation packages **Geant4** and **Penelope2008** are discussed and a summary of the observed limitations is given.

---

<sup>1</sup>KESS is short for **KATRIN Electron Scattering in Silicon**

To describe the energy losses of the electrons in detail, differential inelastic collision cross sections are required. The detailed description of electron backscattering additionally requires differential elastic cross sections. The track of an electron in silicon is fully defined by elastic and inelastic collisions. Two models describing inelastic collisions and one model describing elastic collisions are presented in Section 4.2.

The production of secondary electrons, which contribute to backscattering, has to be described by an ionization model yielding knock-on electrons from ionized shells, and an atomic relaxation model creating Auger electrons. Two models for the ionization<sup>2</sup> and one model for the relaxation are described in Section 4.3. The effects of the interface of vacuum to silicon, resulting in an energy and angle dependent transmission probability are also described and included in the simulation (Sec. 4.4).

Finally, the role of this newly created simulation in the global KATRIN simulation framework *Kassiopeia* is highlighted and some features of the framework are presented briefly in Section 4.6.

The evaluation of this simulation is included in Chapter 5 and the application to KATRIN test experiments is shown in Chapter 6.

## 4.1 Motivation

### 4.1.1 Detector response to x-rays and electrons

The detector response is usually defined as the energy spectrum gathered from the detector from incidence of a mono-energetic particle beam. The detector response to low-energy electrons is fundamentally different from the response to x-rays. In the energy range below 100 keV, x-rays almost exclusively interact via the photoelectric effect<sup>3</sup>. The x-ray is absorbed by the solid and, in good approximation, its total energy is transferred to an electron (photoelectron). These interactions take place over the whole wafer thickness  $t$ . A typical silicon semiconductor detector has a thickness of  $t = 500 \mu\text{m}$ . In contrast, low-energy electrons hitting the detector only travel a few  $\mu\text{m}$  from the detector surface into the silicon.

Compared to x-rays, electrons lose their energy in silicon in a different way. They are not absorbed in one interaction, but lose energy in many subsequent collisions. However, the only difference between electrons and x-rays incidence is the position where these interactions take place. Apart from that, a photoelectron created by x-rays behaves no different in the silicon, than an electron hitting the detector.

Figure 4.1 shows the simulated detector response for a mono-energetic x-ray and electron beam with an incident energy of  $E_I = 18 \text{ keV}$ . The response to x-rays is a sharp peak at 18 keV, broadened by the energy resolution  $\Delta E_{\text{FWHM}} = 0.2 \text{ keV}$  of the

<sup>2</sup>However, only one is available in the simulation.

<sup>3</sup>Compton scattering is a sub-1% effect [56] and is not of interest for this study.

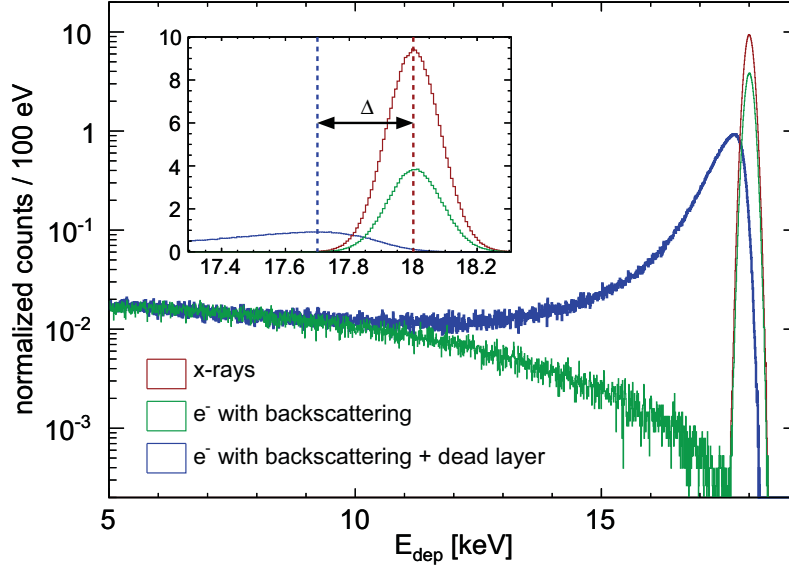


**Figure 4.1:** The simulated detector response to x-rays and electrons with the same incident energy  $E_I = 18$  keV. The detector has an energy resolution  $\Delta E_{\text{FWHM}} = 0.2$  keV.  $E_{\text{dep}}$  is the deposited energy. **(red)** Response to x-rays. **(green)** Response to electrons considering backscattering. **(blue)** Response to electrons considering backscattering and a step function dead layer  $\lambda_D = 300$  nm. The inlay shows the difference  $\Delta$  between the most probable energy deposit for x-rays and electrons. The difference between (red) and (green) shows the influence of backscattering. The difference between (green) and (blue) shows the influence of a dead layer.

detector. The energy resolution is a random contribution to the signal through

- Fano noise, describing the statistical variation of the charge carriers produced for an incident energy  $E_I$ ,
- other intrinsic noise contributions from the detector (e.g. thermal noise, leakage current), and
- electronic noise from the signal amplification chain.

This results in an effective smearing of the expected delta function at the x-ray energy  $E_I$  into a Gaussian function with the full width at half maximum  $\Delta E_{\text{FWHM}}$  and the mean  $E_I$ .

Low-energy electrons hitting the detector are generally close to the detector surface. During elastic and inelastic collisions, the direction of the electron is changed. Therefore, the electrons can exit the detector at the surface again. This effect is called backscattering. The inclusion of backscattering effects changes the detector response (Fig. 4.1). Below the incident energy peak, a rising count rate towards lower energies is visible, which is caused by the partial energy depositions of backscattered electrons. It is obvious from this distribution that backscattering is a random effect.

The peak at the incident energy is caused by electrons depositing their full energy and is effectively lowered in comparison to the peak caused by x-rays.

Silicon semiconductor detectors have a thin surface layer, where created charge carriers are not collected. This insensitive layer is called dead layer and has a typical thickness of a few 100 nm. Energy deposited in the dead layer does not contribute to the detector signal. Since most electrons entering the detector will deposit energy in this dead layer, the detector response is changed (Fig. 4.1). The inclusion of a dead layer results in a broad low-energy tail of the the observed peak. The total peak height is lowered by 85% and the most probable energy deposited is shifted by  $\Delta = -0.3 \text{ keV}$  when compared to the x-ray peak. The distribution also shows that energy deposits in the dead layer are random.

To successfully describe the detector response of silicon semiconductor detectors, the following has to be modeled precisely:

- The energy loss of low-energy electrons in silicon,
- the trajectory of the electron, which can lead to backscattering,
- the energy deposition in the detector,
- the charge collection efficiency, where dead layers lead to partial charge collection,
- the amplification chain of the detector signal, and
- the analysis of the detector signal (i.e. data acquisition system).

### 4.1.2 Efficiency of the focal plane detector

During neutrino mass measurements, the focal plane detector is used to detect electrons with an incident energy  $18.3 < E_I < E_0 \approx 18.6 \text{ keV}$ . The detector response is given by the *energy deposited* by the electrons in the sensitive detector volume. The processes influencing this signal were described above. To exclude a majority of background and noise events, an energy region of interest (ROI) is defined. The detection efficiency  $\varepsilon$  for a mono-energetic electron beam is then defined as

$$\varepsilon = \frac{N_{\text{ROI}}}{N_I} \quad (4.1)$$

where  $N_I$  is the number of incident electrons and  $N_{\text{ROI}}$  is the number of counts in the region of interest assumed to be free of background.

Energy deposition in the dead layer results in a shift of the peak from the incident energy to lower energies, and in a broad low-energy tail (Sec. 4.1.1 and Sec. 5.3). Thus, the unaccounted for energy deposits in the dead layer can lead to an energy deposition in the sensitive detector volume that is below the lower edge of the region of interest.

Incident electrons have a probability to be backscattered from solids (Sec. 5.2). They may enter the silicon, effectively change their direction by  $90^\circ < \Delta\theta \leq 180^\circ$  and exit the detector again. Electrons are deflected by scattering with the silicon atoms or the silicon shell electrons (Sec. 4.2). Depending on the total energy loss in the sensitive detector region, they can also deposit energy below the lower edge of the region of interest. Electrons can be backscattered by elastic collisions only suffering negligible energy losses. Thus, they do not deposit any energy. This effect is closely correlated to the effective dead layer of the detector. If the backscattered electron only deposits energy in the dead layer, no detector signal is observed.

To first approximation, the probability of backscattering depends on the charge number of the solid, as well as the angle and kinetic energy of the incident electron. The maximum incident angle  $\theta_{\text{det,max}}$  of electrons at the focal plane detector is determined by

$$\theta_{\text{det,max}} = \arcsin \sqrt{\frac{B_{\text{det}}}{B_{\text{max}}}} \quad (4.2)$$

with the magnetic field at the detector  $B_{\text{det}}$  and the maximum magnetic field in the setup  $B_{\text{max}}$ . For the design values of  $B_{\text{det}} = 3 \text{ T}$  and  $B_{\text{max}} = 6 \text{ T}$  the maximum incident angle is  $\theta_{3 \text{ T}} = 45^\circ$ . For a setup where the magnetic field in the source is equal to the magnetic field at the detector  $B_{\text{det}} = 3.6 \text{ T}$  the maximum incident angle is  $\theta_{3.6 \text{ T}} = 50.77^\circ$ .

Electrons backscattered from the focal plane detector are guided towards the main spectrometer by the magnetic field lines. Depending on their backscattering angle and energy, they can be transmitted back to the source, or they can be reflected either by the magnetic mirror effect or the electrostatic main spectrometer potential. In case of reflection, they re-enter the detector and can deposit energy again. While travel times in the detector are on the magnitude of picoseconds, travel times in the spectrometer can be on the order of tens of microseconds. Depending on the DAQ shaping time, which is typically a few  $\mu\text{s}$ , this can lead to a further decrease in detection efficiency. Even the lowest energy backscattered electrons can be important in the KATRIN beam line setup. The combination of magnetic and electric fields can, in rare cases, cause Penning traps, in which electrons are localized. These traps can be filled even by the lowest-energy electrons and can contribute to backgrounds by the ionization of residual gas molecules [49].

The detector efficiency  $\varepsilon$  influences the measurement time needed to reach the statistical uncertainty on the neutrino mass measurement (Eq. 2.12). To first approximation, each percentage loss in detector efficiency requires an increase in the measurement time of 0.5 months in order to achieve the same statistics [57]. To maximize the detection efficiency, a low- $Z$  detector material, a thin dead layer, high incident energies and close to normal incident angles are preferable (Sec. 5.2). The results of simulations describing these phenomena are contained in Section 6.2.2.

In general, the detector efficiency  $\varepsilon$  does not enter directly into the neutrino mass analysis of KATRIN. Its true value is hidden in the analysis by unconstraining the

fit with regard to the total number of counts. The analysis is insensitive to a varying detector efficiency over time. It is, however, sensitive to the *shape* of the measured  $\beta$ -decay spectrum. A detector efficiency depending on the energy of the  $\beta$  electrons, which would change the shape of the spectrum, introduces a systematic uncertainty on  $m_\nu^2$ .

Studies on the analysis of  $m_\nu^2$  define the need that an incident energy dependent detection efficiency  $d\varepsilon/dE$  is known down to a level of  $d\varepsilon/dE < 10^{-4}/\text{eV}$ . This can be achieved either by measurements or simulations. The analysis is described in more detail in Sections 6.2.2 and 2.4.

### 4.1.3 Simulation of the detector response

Charged particles in solids lose energy along their trajectory through coulomb interactions. The mean free path between two interactions and the energy loss is small compared to e.g. photon or neutron interactions with matter. The total energy loss is the sum of all radiative and collisional energy losses. For electrons in silicon, the critical energy, at which radiative and collisional energy losses per path length are equal, is  $E_C \approx 40 \text{ MeV}$  [56]. For the KATRIN experiment, the maximum expected electron incident energy  $E_{1,\text{max}} \approx 40 \text{ keV}$ . This includes an optional post-acceleration of the  $\beta$ -electrons. As shown in [56, 58] radiative energy losses through electron-nucleus and electron-electron bremsstrahlung are a  $10^{-4}$  effect and are neglected for this simulation.

The *average* inelastic energy loss of charged particles per path length is usually described by the Bethe formula (Eq. 4.4). In the case of electrons, the incident and the target particle have the same rest mass and are indistinguishable. The maximum energy transfer in a single collision of an electron with kinetic energy  $E$  then is

$$\Delta E_{\text{max}} = \frac{1}{2}E, \quad (4.3)$$

and the angular deflection can not be neglected. Additionally, an added shell correction takes into account effects arising when the speed of the incident electron becomes comparable to the orbital velocity of the shell electrons. The density correction describes the polarization of electrons far away from the incident electron trajectory and becomes important at high incident energies.

Finally, an expression for a small mean energy loss  $dE$  per path length  $dx$  for electrons, known as the stopping power  $S(E)$ , is given by Bethe [56] as

$$S(E) = -\frac{dE}{dx} = 2\pi N_a r_e^2 m_e c^2 \rho \frac{Z}{A} \frac{1}{\beta^2} \left[ \ln \frac{\tau^2(\tau + 2)}{2(I/m_e c^2)^2} + F(\tau) - \delta - 2\frac{C}{Z} \right] \quad (4.4)$$

where  $\tau$  is the kinetic energy of the incident electron in  $m_e c^2$  and

$$F(\tau) = 1 - \beta^2 + \frac{\tau^2}{8} - \frac{(2r + 1) \ln 2}{(\tau + 1)^2}$$

with

$r_e$ :	classical electron radius	$m_e$ :	electron mass
$N_a$ :	Avogadro's number	$I$ :	mean excitation potential
$Z$ :	atomic number of absorber	$A$ :	atomic weight of absorber
$\rho$ :	density of absorbing material	$\beta$ :	$v/c$ of the incident electron
$\delta$ :	density correction	$C$ :	shell correction.

The mean excitation potential  $I$  represents all possible contributions of all excitation processes to the energy loss and can be calculated or extracted from experimental data<sup>4</sup>.

The stopping power  $S(E)$  can be used to calculate the *average* energy loss  $\Delta E_{\text{CSDA}}$  in the continuous-slowing-down-approximation (CSDA) by

$$\Delta E_{\text{CSDA}} = \int_0^x S(E) dx. \quad (4.5)$$

This method does not describe the fluctuations in energy loss (*straggling*). These are especially important for very thin layers with only a few inelastic collisions. For an electron with energy  $E = 18$  keV and a path length  $l = 100$  nm, the simulation gives an average of only 3.8 inelastic collisions. For very thin layers (*dead layers*), the energy losses are completely random [60]. In both inelastic and elastic collisions the electrons also change direction of travel due to angular deflections (*multiple scattering*). Total angular deflections may exceed  $90^\circ$ , leading to *backscattering*.

As shown in Chapter 6, the detailed modeling of the backscattering coefficient and the backscattered electron energy distribution are crucial in finding possible systematic effects of the KATRIN experiment. The cascade of secondary electrons observed in experiments [61, 62] can not be generated in the continuous-slowing-down-approximation. These arguments are independent of how  $S(E)$  was derived. Therefore, the continuous-slowing-down-approximation should not be used for low-energy electrons or thin layers [63, 64, and see Fig. 4.2]. Values for the total, radiative and collisional stopping power, as well as the continuous-slowing-down-approximation range can be conveniently obtained from [58] for electrons with energies from 1 keV to 10 GeV. The relative error on the stopping power is stated as 5-10% for electrons with energies from 10-100 keV, and larger below 10 keV.

General purpose codes like `Geant4` [65] and `Penelope2008` [66] use mixed and detailed (event-by-event) modeling of particle interactions with matter, and are applicable for many particles, materials and energy regimes. Results obtained with `Geant4` and its low-energy package suffered from an unacceptable dependency on

---

<sup>4</sup> $I = 173$  eV for silicon [56]. More recent calculations state  $I = 164$  eV [59]

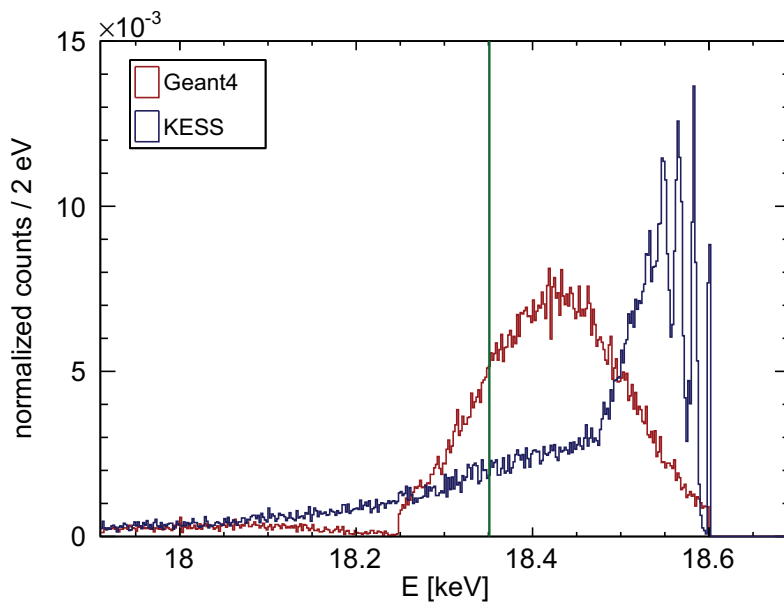


**Figure 4.2:** Energy distribution of a mono-energetic electron beam with energy  $E_I = 18.6$  keV after 100 nm of silicon. KESS simulations are compared to the results obtained with Geant4.9.1 and its low-energy package [65]. The vertical green line is the energy distribution obtained with the continuous-slowing-down approximation excluding energy loss straggling. See Sec. 5.3 for more details.

simulation parameters (see also [67, 68]) and artifacts of the condensed inelastic scattering approach, when dealing with nanometer scale dead layers.

The energy distribution of electrons with incident energy  $E_I = 18.6$  keV after traversing 100 nm of silicon calculated with Geant4 is compared to results from the simulation created in this study (KESS) (Fig. 4.2). In Geant4, the losses in the silicon slab with 100 nm thickness are approximated by energy straggling around an average energy loss. With KESS, the detailed description of single energy losses is visible (Sec. 5.2.3 and Sec. 5.3 for details). Additionally, below incident energies of  $E_I \approx 2$  keV, backscattering was no longer obtained in Geant4 (Fig. 5.4).

Results obtained with Penelope2008 for the energy distribution of backscattered electrons for incident electrons with energy  $E_I = 1$  keV are compared to an experiment (Fig. 4.3). They were calculated with the detailed simulation mode of Penelope2008. Artifacts resulting from an almost discrete most probable energy loss in a single collision are visible in the high energy peak. This is either caused by the binning of the Penelope2008 inelastic cross section tables or, more likely, by the use of a delta function as an approximation for the generalized oscillator strength (Sec. 4.2.1 and Sec. [69]). Almost no elastically backscattered electrons are observed, which are of high importance for the focal plane detector efficiency (Sec. 6.2.2). Additionally, electrons with an energy less than 50 eV can not be treated by Penelope2008. For more details, see Section 5.2.

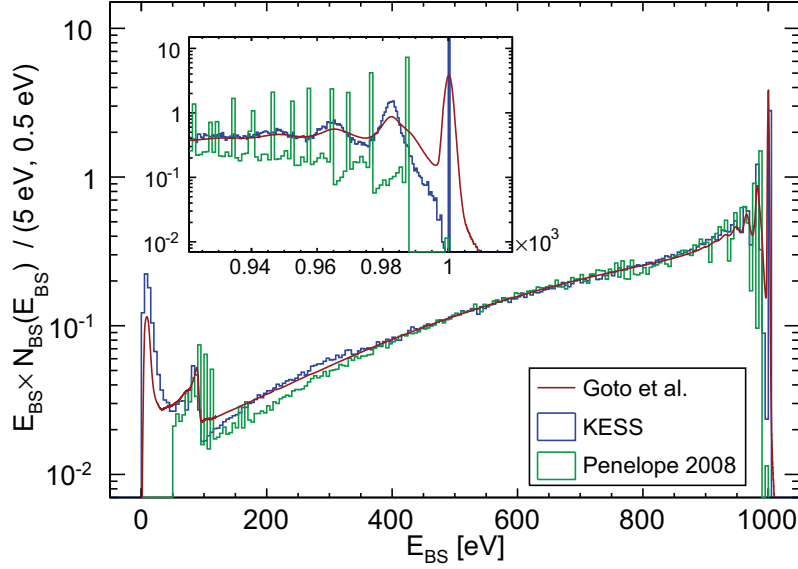


**Figure 4.3: Energy distribution of backscattered electrons for 1 keV incident electrons.** Simulation results obtained with KESS and Penelope2008 [66] are compared to experimental data [61]. The simulated distributions were normalized to the number of incident electrons and multiplied by the backscattered energy  $E_{\text{BS}}$ , while experimental values are normalized to match the average counts of KESS in the interval  $450 < E_{\text{BS}} < 550$  eV. The experimental energy resolution was *not* applied to both simulations to emphasize the artifacts of Penelope2008. For more details and results see Sec. 5.2.

It should however be noted here that Geant4 and Penelope2008 are very valuable simulation tools. Penelope2008 generally produces good results even at low energies. It is only the combination of a very thin dead layer and the need for detailed backscattered electron energy distributions that is preventing the application for KATRIN.

To fulfill the requirements for KATRIN, a specialized event-based Monte Carlo approach will be used to describe the electron trajectories and energy losses. The energy loss mechanisms are inelastic collisions with shell electrons and collective excitations (Sec. 4.2.1). The scattering angle depends on the energy loss and can be large. A second process is elastic Coulomb scattering with the atoms (Sec. 4.2.2). Although the energy loss in elastic collisions is very small<sup>5</sup> and can in first approximation be neglected, the sum of all angular changes is important for the trajectory and the comparison to experimental results. For example, electrons backscattered without having done any inelastic scattering produce the elastic peak which is visible in experiments [70, 71, 61] and is for example shown in Figure 4.3.

<sup>5</sup>An electron with incidence energy  $E_I = 18$  keV loses  $\Delta E_{\text{BS}} \approx 1.4$  eV when being fully elastically reflected by a free silicon atom.

The energy lost by the incident electron can cause inner-shell ionization. A so called knock-on electron is eventually emitted, leaving the atom in an excited state. The relaxation of the atom creates further particles. As these processes repeat, a cascade of secondaries is produced. Finally, to escape the silicon, electrons have to overcome a potential barrier between the minimum of the conduction band and the vacuum potential.

## 4.2 Electron scattering in silicon

### 4.2.1 Inelastic collision cross sections

Collision cross sections (CCS) are differential in energy loss  $\Delta E$  and are used to describe the inelastic collisions. They are derived by integrating doubly differential cross sections in  $\Delta E$  and in momentum transfer  $q$ :

$$\sigma(\Delta E) = \int_{q_{min}}^{q_{max}} \sigma(\Delta E, q) dq \quad (4.6)$$

The total inelastic cross section then is

$$\sigma_I = \int_0^{\infty} \sigma(\Delta E) d(\Delta E) \quad (4.7)$$

The Moments  $M_\nu$  of Eq. 4.7 are defined as

$$M_\nu = N_a \int_0^{\infty} (\Delta E)^\nu \sigma(\Delta E) d(\Delta E), \quad \nu = 0, 1, \dots \quad (4.8)$$

where  $N_a$  is the number of atoms per unit volume. Thus,  $n = tM_0$  is the average number  $n$  of collisions in an absorber of thickness  $t$ . The Moment  $M_1$  is the stopping power.

Two different theoretical approaches to calculate these cross sections derived from first principles are used in **KESS**. One is based on a model dielectric function proposed by Penn [72], the other is based on the first Born approximation for inelastic scattering on free atoms [73]. Both are described below.

The probability for an energy loss  $\Delta E$  in an inelastic collision for an electron with kinetic energy  $E$  is represented by the cumulative probability density function (PDF)  $P(\Delta E; E)$ , which can be derived from the collision cross section  $\sigma(\Delta E; E)$  by

$$P(\Delta E; E) = \frac{\int^{\Delta E} \sigma(\Delta E'; E) dE'}{\int^{\infty} \sigma(\Delta E'; E) dE'}. \quad (4.9)$$

To speed up the simulation, the probability density functions for various kinetic energies are pre-calculated and used in a tabulated form, from which KESS samples in the following steps:

1. The two pre-calculated probability density functions,  $P_1(\Delta E; E)$  and  $P_2(\Delta E; E)$ , closest to the kinetic energy  $E$  are found.
2. A uniformly distributed random number  $R \in [0, 1]$  is thrown.
3. The two closest values for the tabulated  $P_1(\Delta E; E) \in [0, 1]$  to  $R$  are found.
4. The two associated energy losses  $\Delta E$  are linearly interpolated to find  $\Delta E_1(R)$ .
5. Steps 3 and 4 are repeated for  $P_2(\Delta E; E)$  to find  $\Delta E_2(R)$ .
6. Finally, the values  $\Delta E_1(R)$  and  $\Delta E_2(R)$  are linearly interpolated to find  $\Delta E(R)$  for  $E$ .

### Bethe-Fano's cross sections

A cross section for a single collision doubly differential in energy loss  $\Delta E$  and momentum transfer  $K$  was derived by Bethe [74] using the first Born approximation for free atoms, which was later extended to solids by Fano [73].

The cross section is given as

$$d\sigma(\Delta E, Q) = \frac{2\pi e^4 z^2}{mv^2} Z |F(\Delta E, K)|^2 \frac{dQ}{Q^2} \quad \text{non - relativistic} \quad (4.10)$$

$$d\sigma(\Delta E, Q) = \frac{2\pi e^4 z^2}{mv^2} Z \left( \frac{\xi(\Delta E, K) + \tau(\Delta E, K)}{Q} \right) \left( 1 + \frac{Q}{mc^2} \right) dQ \quad (4.11)$$

where  $Q = q^2/2m$ , with  $q = \hbar K$  is the momentum transferred from the incident particle to the absorber and  $v$  is the particle speed.  $\xi(\Delta E, K)$  is the longitudinal excitation function and  $\tau(\Delta E, K)$  is the transverse excitation function. They are defined by

$$\xi(\Delta E, K) = \frac{|F(\Delta E, K)|^2}{(1 + Q/2mc^2)^2} \quad (4.12)$$

$$\tau(\Delta E, K) = \frac{|\beta_t G(\Delta E, K)|^2}{[1 + Q/2mc^2 - \Delta E/(2mc^2 Q)]^2} \quad (4.13)$$

with the matrix elements  $F(\Delta E, K)$  and  $G(\Delta E, K)$  for longitudinal and transverse excitations and the component  $\beta_t$  of  $\beta = v/c$  perpendicular to  $K$ .

The matrix elements can be expressed through the generalized oscillator strength

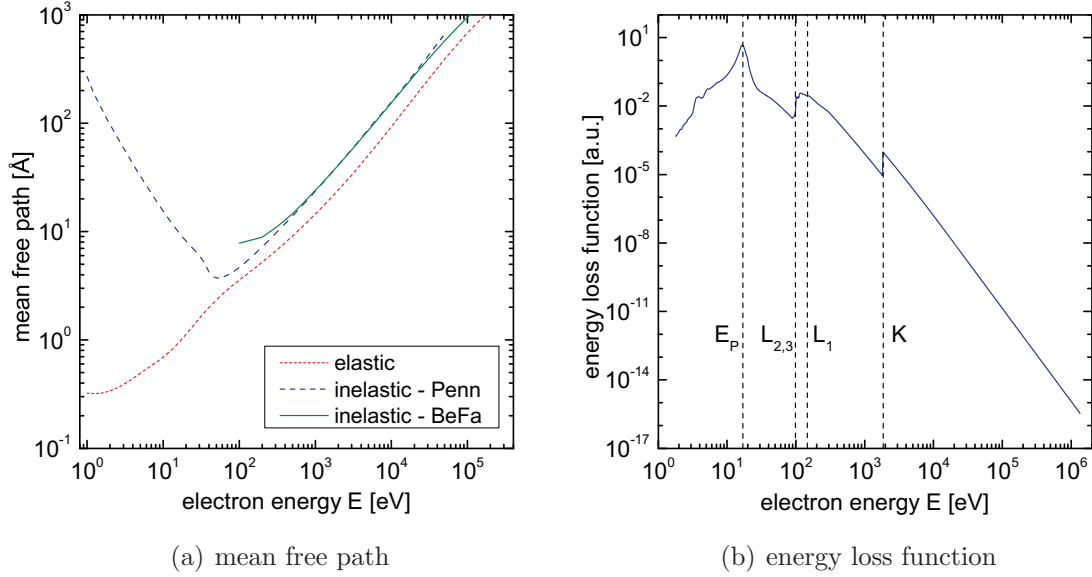


**Figure 4.4: Mean free path and energy loss function.** (a) Elastic and inelastic mean free path over the electron energy  $E$ . Results from Bethe-Fano's cross sections (BeFa) and Penn's dielectric formalism (Penn) are shown. Above 100 eV, the inelastic mean free path is dominated by inner-shell ionization. Below 100 eV, only valence band excitations are possible. (b) The energy loss function  $\text{Im}\{-1/\epsilon(\omega)\}$  from Penn's dielectric formalism over the electron energy  $E$ . The plasmon energy  $E_p$  and the K- and L-shell binding energies are shown as vertical lines [75].

$f(\Delta E, K)$  by

$$|F(\Delta E, K)|^2 \propto \frac{Qf(\Delta E, K)}{\Delta E} \quad (4.14)$$

$$|\beta_t G(\Delta E, K)|^2 \propto \frac{\beta_t^2 \Delta E f(\Delta E, K)}{2mc^2} \quad (4.15)$$

which becomes the dipole oscillator strength  $f(\Delta E, 0)$  in the limit  $K \rightarrow 0$ . For solids, the dipole oscillator strength is replaced by the complex dielectric function  $\epsilon(\Delta E) = \epsilon_1(\Delta E) + i\epsilon_2(\Delta E)$ .

The first order Born approximation is only valid for electron energies larger than the energies of the shell electrons. For silicon, this model is accurate for electrons with an energy of a few keV and more.

The full model for solids is described by Fano [73]. The corresponding probability density functions  $P(\Delta E; E)$  are shown in Figure 4.5(a), and the mean free path in Figure 4.4(a). A review and evaluation of Bethe-Fano's cross sections, as well as the theoretical and experimental sources to calculate them for silicon is found in [64]. The data tables for electron energies  $0.1 < E < 400$  keV available in KESS were supplied in electronic format by the author of [64], H. Bichsel.

### Penn's dielectric formalism

The inelastic scattering of electrons in solids can be described by the dielectric formalism [76, 72]. The doubly differential cross section is given by

$$\frac{d^2\lambda_{\text{in}}^{-1}}{d(\hbar\omega)dq} = \frac{1}{\pi a_0 E} \text{Im} \left\{ \frac{-1}{\epsilon(q, \omega)} \right\} \frac{1}{q} \quad (4.16)$$

where  $\lambda_{\text{in}}$  is the inelastic mean free path (MFP),  $\Delta E = \hbar\omega$  is the energy loss,  $\hbar q$  is the momentum transfer for an electron with kinetic energy  $E$ ,  $\epsilon(q, \omega)$  is the dielectric function,  $a_0$  is the Bohr radius and  $\text{Im} \left\{ \frac{-1}{\epsilon(q, \omega)} \right\}$  is the energy loss function.

The optical energy loss function  $\text{Im} \left\{ \frac{-1}{\epsilon(\omega)} \right\}$  can be extended to the electron energy loss function  $\text{Im} \left\{ \frac{-1}{\epsilon(q, \omega)} \right\}$  by

$$\text{Im} \left\{ \frac{-1}{\epsilon(q, \omega)} \right\} = \frac{\omega_0}{\omega} \text{Im} \left\{ \frac{-1}{\epsilon(\omega_0)} \right\} \quad (4.17)$$

with  $\omega_0$  being the positive solution of the dispersion relation

$$\omega_q^2(q, \omega_p) = \omega_p^2 + \frac{1}{3} v_f^2(\omega_p) q^2 + \left( \frac{\hbar q^2}{2m} \right)^2 \quad (4.18)$$

where  $v_f(\omega_p)$  is the Fermi-velocity of a free-electron gas with plasma frequency  $\omega_p$ .

A model dielectric function is proposed, which for  $q = 0$  is set equal to the measured optical dielectric function  $\epsilon(\omega)$ . Equation 4.16 then becomes

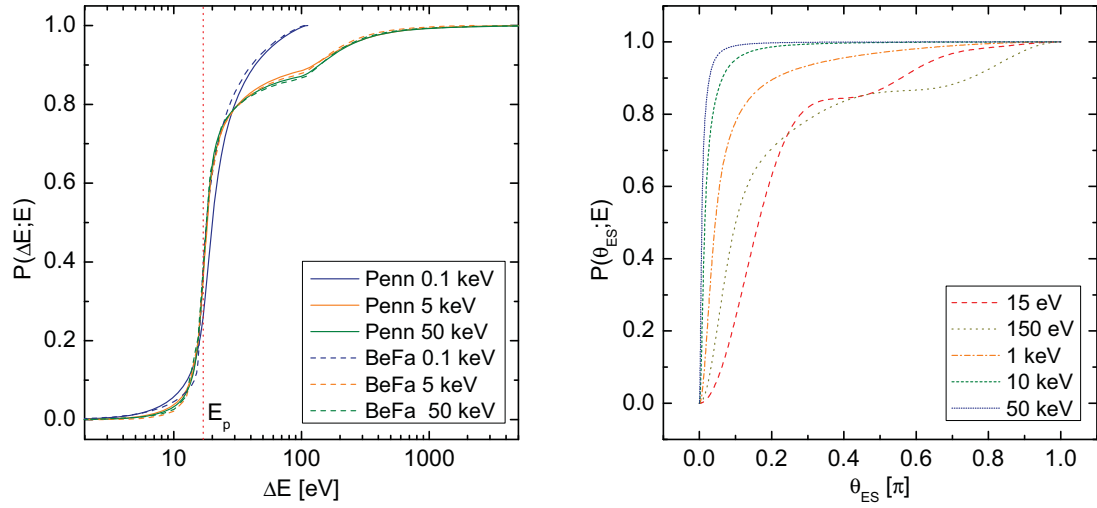
$$\begin{aligned} \frac{d^2\lambda_{\text{in}}^{-1}}{d(\Delta E)} = \frac{1}{2\pi a_0 E \Delta E} \int_0^\infty \frac{\hbar\omega_p}{\Delta E - \hbar\omega_p} \text{Im} \left\{ \frac{-1}{\epsilon(\omega_p)} \right\} d(\hbar\omega_p) \\ \times \Theta \left( \frac{\hbar^2}{2m} (2k\bar{q} - \bar{q}^2) - \Delta E \right). \end{aligned} \quad (4.19)$$

The dependence of the energy loss function on  $q$  is given by a single plasmon pole dispersion

$$\bar{q} = \sqrt{2m/\hbar(\omega - \omega_p)} \quad (4.20)$$

This expression gives the probability for an electron with energy  $E$  to suffer an energy loss  $\Delta E$  and is equivalent to the inelastic collision cross section  $\sigma(\Delta E; E)$ . The corresponding probability density functions  $P(\Delta E; E)$  are shown in Figure 4.5(a).

The accuracy of Penn's model cross sections depends on the optical dielectric constants. Experimental and theoretical sources can be used, but are not guaranteed to exist or to be accurate for every solid. For silicon, many sources exist and the optical



(a) inelastic probability density function

(b) elastic probability density function

**Figure 4.5: Probability density functions for scattering.** (a) Inelastic probability density functions  $P(\Delta E; E)$  for an energy loss  $\Delta E$  by an electron with kinetic energy  $E$ . The plasmon energy  $E_p = \hbar\omega_p \approx 17$  eV with the plasma frequency  $\omega_p$  is shown as a vertical line. For all  $E$ , energy losses around  $E_p \pm 10$  eV are the most probable energy losses. (b) Elastic probability density functions  $P(\theta_{ES}; E)$  for an elastic scattering angle  $\theta_{ES}$  by an electron with kinetic energy  $E$ . The average scattering angle increases with lower electron energies.

dielectric constants to calculate the optical energy loss function were compiled by Bichsel [64]. Penn's model cross sections describe the effects of bulk plasmon excitations, interband transitions and inner-shell ionization. The first moment of the doubly differential cross section is the inelastic mean free path, the second moment is the stopping power (SP). The mean free path is shown in Figure 4.4(a). The probability density functions are available for electron energies  $1 \text{ eV} < E < 50 \text{ keV}$  in KESS and were supplied in electronic format by Z. Chaoui [75].

## 4.2.2 Elastic scattering cross sections

To describe elastic scattering in KESS, the elastic differential cross sections (DCS) per unit solid angle  $d\sigma/d\Omega$  and the total elastic cross section

$$\sigma(E) = \int_0^\pi \frac{d\sigma}{d\Omega} 2\pi \sin \Theta d\Theta \quad (4.21)$$

are needed.

While many sources for elastic differential cross sections are available [77], a recent code (ELSEPA) can compute the elastic differential cross sections based on first principles over an incident electron energy range of 50 eV to 100 MeV [78]. The differential cross sections are calculated from the solution of the Schrödinger or Dirac equation, using the partial wave expansion method for the direct scattering amplitude  $f(\Theta)$  and the spin-flip scattering amplitude  $g(\Theta)$ , to finally yield

$$\frac{d\sigma}{d\Omega} = |f(\Theta)|^2 + |g(\Theta)|^2. \quad (4.22)$$

The elastic scattering between incident electron at  $\vec{r}$  and the target is described by a optical-model potential

$$V(r) = V_{\text{st}}(r) + V_{\text{ex}}(r) + V_{\text{cp}}(r) - iW_{\text{abs}}(r) \quad (4.23)$$

where  $V_{\text{st}}(r)$  is the electrostatic interaction potential,  $V_{\text{ex}}(r)$  is the electron exchange potential,  $V_{\text{cp}}(r)$  is the correlation-polarization potential, and  $iW_{\text{abs}}(r)$  is the magnitude of the imaginary absorption potential. Spherical symmetry is assumed for the atomic charge distribution and the potential from Eq. 4.23. For  $V_{\text{st}}(r)$  the static exchange approximation is completely determined by the adopted nuclear and electronic charge-density models. Various options are included in the code. Following the recommendation of the authors [79, 78],  $V_{\text{st}}(r)$  was calculated with the Fermi distribution for the nuclear and the numerical Dirac-Fock densities for the electronic charge-density.

Finally, for  $V_{\text{cp}}(r)$ , the local-density-approximation correlation-polarization potential can be used. The imaginary absorption potential  $iW_{\text{abs}}(r)$  as proposed by Salvat [78] can be used to account for the loss of particles from the elastic to inelastic channels. For solids however, no accurate approaches for the absorption potential and the correlation-polarization potential exist. The authors of the code compare calculated atomic differential cross sections with measurements obtained from solids [79]. They conclude that *atomic* differential cross sections with the potentials from Eq. 4.23 but without the exchange potential  $V_{\text{ex}}(r)$  can be used for electrons in solids.

The differences between the cross section models for different interaction potentials are below 8%. The cross sections were evaluated and compared to measurements [80, 79]. Differential cross sections computed with this code are also included in the NIST database [81]. Probability density functions for electron energies from  $1 \text{ eV} < E < 400 \text{ keV}$  are included in KESS. The data tables containing the probability density functions  $P(\theta_{\text{ES}}; E)$  are used in a similar way as described in Section 4.2.1 and are shown in Figure 4.5(b).

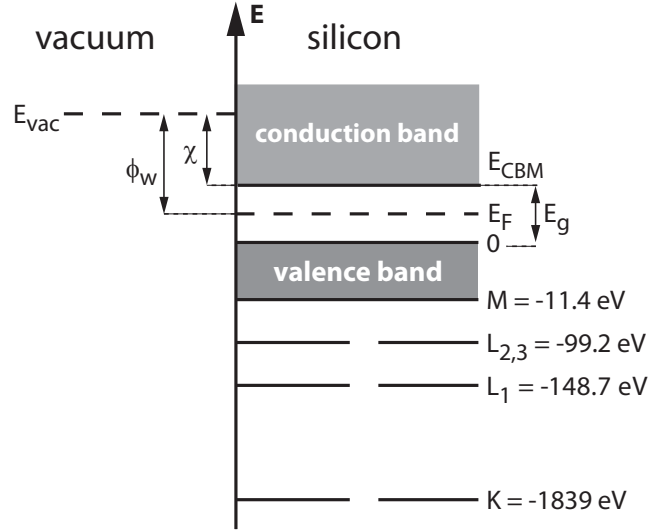


**Figure 4.6: Schematic energy levels of solid silicon** with the silicon shell binding energies, the silicon electron affinity  $\chi$  and workfunction  $\phi_w$ , the Fermi energy  $E_F$ , the vacuum energy  $E_{vac}$ , the indirect silicon band gap  $E_g$  and the conduction band minimum  $E_{CBM}$ .

## 4.3 Secondary electron production

### 4.3.1 Ionization and knock-on electrons

It is assumed that each inelastic collision with an energy loss  $\Delta E$  ionizes an inner shell or excites the valence band. Furthermore, each inelastic collision creates a knock-on electron (KE), which continues to interact with the silicon. This electron is also called delta ray in the literature. From a simulation point of view, it is not treated different from a simulation primary. It has to be emphasized here that generally an energy loss is not equal to an energy deposition, since most of the lost energy is transferred to a knock-on electron. Although the primary electron lost energy in the sensitive detector region, secondaries can escape the silicon (Sec. 5.2) or travel to insensitive detector regions like the dead layer (Sec. 5.3). The influence of secondary electrons on the detector response and backscattering is discussed in Section 5.1.

A knock-on electron produced from an inner shell has an energy  $E_{KE} = \Delta E - E_b$  where  $E_b = E_K, E_{L1}, E_{L2,L3}$  is the corresponding binding energy of the shell electron (Fig. 4.6). For M-shell excitations,  $E_b$  is randomly sampled from a uniform distribution in an interval  $0 < E_b < E_M$ , since the M-shell in crystalline silicon is broadened to a continuous valence band.

To find the probability to ionize a certain shell in dependence on  $\Delta E$ , the interaction of the incident electron and the shell electron is described via a virtual photon. The ionization probability is taken from [82] and shown in Figure 4.7. For all  $\Delta E > E_K$ ,

there is a constant 92% probability to ionize the K-shell and 8% for the L<sub>1</sub>-shell. For  $E_{L2,L3} < \Delta E < E_K$  the probabilities for L<sub>1</sub>, L<sub>2</sub>, L<sub>3</sub> and M-shell ionization are strongly dependant on  $\Delta E$ . Note that the L<sub>2</sub>- and L<sub>3</sub>-shell are are treated separately here, although they are energetically degenerate. Finally, all  $\Delta E < E_{L2,L3}$  excite the valence band. The actual number of ionizations per simulated track for different energies is shown in Tab. 4.1.

The scattering angle  $\Theta_{IS}$  of the incident electron is determined by the energy loss  $\Delta E$  from Eq. 4.42. For the polar emission angle of the knock-on electron, two approaches can be used. Both are included as an option in **KESS**. One is based on *momentum conservation*: the polar angle  $\Theta_{KE}$  is correlated with the incident electron trajectory, the energy loss  $\Delta E$  and the incident energy  $E$  by

$$\sin \Theta_{KE} = \cos \Theta_{IS} \quad (4.24)$$

where  $\Theta_{IS} = \arcsin \sqrt{\Delta E/E}$  is the angle between the incoming and outgoing trajectory of the the incident electron. Since this implies a binary collision, the scattering can be described on one plane. Therefore, the azimuthal angle is

$$\Phi_{KE} = \pi + \Phi_{IS}, \quad (4.25)$$

with  $\Phi_{IS}$  being the azimuthal scattering angle of the incident electron from Eq. 4.41.

The second approach included as an option assumes *spherical symmetry* for the emitted knock-on electron. Since the emission is taking place in a solid, the emission angle can be influenced by interactions of the knock-on electron with shell electrons, the nucleus or the crystal lattice. Therefore, one can assume that its emission is not correlated with the incident electron trajectory at all and thus violates momentum conservation in a classical two-body sense. The corresponding angles are then sampled with two uniformly distributed random numbers  $R_1, R_2 \in [0, 1]$  with

$$\cos \theta_{KE} = 1 - 2R_1 \quad (4.26)$$

$$\phi_{KE} = 2\pi R_2. \quad (4.27)$$

A second approach to shell ionization is to use ionization cross sections (ICS). While only limited experimental data for the low energy range is available, theoretical approaches exist. One expression was derived by Gryzinski [84] from the classical theory of atomic collisions. A second expression was derived by Casnati et al. [85, 86] from fits to measured K-Shell ionization cross sections. Seah and Gilmore [87] showed that the given expression can also be used for L-shell ionizations. Bote and Salvat proposed a theoretical model from distorted-wave and plane-wave Born approximations [88] yielding ionization cross sections from the shell binding energies up to 1 GeV. These cross sections were approximated by fits with an accuracy of  $\sim 1\%$  [89].

A review showing the relative differences of these three ionization cross sections models and their comparison to data was recently published [90, 91]. These Ionization cross sections are not yet implemented in **KESS**. However, all three approaches

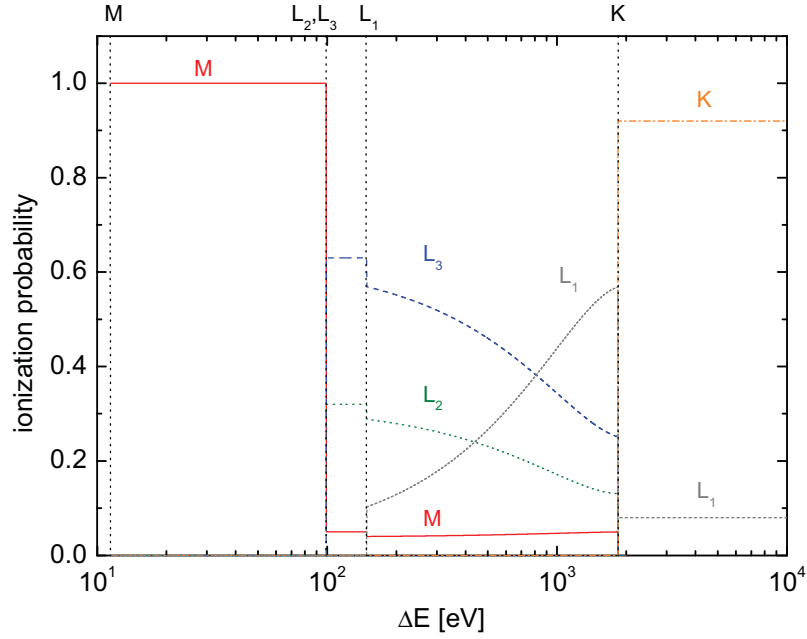


**Figure 4.7: Ionization probabilities** for the silicon K-, L- and M-shell over the energy loss  $\Delta E$  for electrons, assuming an interaction via a virtual photon [83].

to ionization cross sections from the models described above were calculated and are available in tabulated form.

### 4.3.2 Auger electrons

Each ionization of an inner shell leaves the silicon atom in an excited state. During the subsequent rearrangement of shell electrons, the atom can relax through the Auger and Coster-Kronig effect. The empty shell is filled by electrons from other shells (Auger) or from sub-shells (Coster-Kronig) with lower binding energies. The surplus energy is transferred to another electron, which is then emitted. This process continues until all inner shells are filled and all vacancies are transferred to the valence band. The result is a cascade of Auger electrons<sup>6</sup> (AE) [83].

A competing process is relaxation through fluorescence. The empty shell is directly filled with an electron from the valence band and the surplus energy is emitted by a photon. The probabilities for fluorescence are small compared to the Auger effect. They are 4.4% for K-shell, 0.01‰ for  $L_1$ -shell and 0.1% for  $L_2$ ,  $L_3$ -shell vacancies. Since inner shell ionizations are already rare (Tab. 4.1), fluorescence is omitted and a 100% Auger emission is assumed for KESS.

The transition chains and their corresponding probabilities for all shell vacancies are listed in tables 4.3 and 4.4. They are named in a  $123$  scheme, where  $1$  is the

<sup>6</sup>Auger electrons *and* Coster-Kronig electrons are both included in the term 'Auger electrons'.

vacant shell which is filled from shell 2; the Auger electron is emitted from shell 3.  $E_1, E_2$  and  $E_3$  are the binding energies of the corresponding shell. The Auger electron energies are

- $E_{\text{AE}} = E_1 - E_2 - E_3$  for KLL transitions,
- $E_{\text{AE}} = E_1 - E_2 - E_{\text{H}}$  for KLM and LLM transitions, and
- $E_{\text{AE}} = E_1 - (1 + S)E_{\text{M}}$  for KMM and LMM transitions.

$E_{\text{H}}$  is randomly uniformly distributed in  $0 \leq E_{\text{H}} \leq E_{\text{M}}$ , and  $S$  is randomly distributed in  $-1 \leq S \leq 1$  with a probability  $P(S) = 1 - |S|$  [92].

The emission of Auger electrons is spherically symmetric. The polar angle  $\theta_{\text{AE}}$  and the azimuthal angle  $\phi_{\text{AE}}$  can be sampled from

$$\cos \theta_{\text{AE}} = 1 - 2R_1 \quad (4.28)$$

$$\phi_{\text{AE}} = 2\pi R_2. \quad (4.29)$$

with two uniformly distributed random numbers  $R_1$  and  $R_2$ .

After the ionization of an atom or after emitting an Auger electron, the central atomic potential is abruptly changed and an electron can be emitted from the outer shells. Shakeoff probabilities and electron energies for each shell are shown in Tab. 4.2. Again, this process is not included in KESS due to the rare inner-shell ionizations and the low shakeoff electron energies (Tab. 4.1).

## 4.4 The surface escape process

The silicon detector surface is the interface from vacuum to bulk silicon. In metals, the kinetic energy lost while overcoming the potential barrier to exit the solid is the workfunction  $\phi_{\text{w}}$ . It is the difference of the vacuum potential  $E_{\text{vac}}$  and the Fermi level  $E_{\text{F}}$  inside the solid (Fig. 4.6). Since the Fermi level in semiconductors is not accessible, the relevant quantity is the electron affinity  $\chi$  defined as

$$\chi = E_{\text{vac}} - E_{\text{CBM}}, \quad (4.30)$$

with the conduction band minimum  $E_{\text{CBM}}$ . A second characteristic property of the silicon-vacuum interface is the shape of the potential inside the silicon. Potential walls, wells or smooth curves are possible in the first few nanometers. Furthermore, the Fermi level can slowly change throughout the complete depth of a material. All these properties are influenced by surface contamination, temperature, doping and applied electric fields [93, 94].

The KATRIN detectors (Sec. 3) are not metalized on the surface to minimize energy losses and thus ensure a maximum detection efficiency for electrons. The silicon crystal is only passivated by a natural thin layer of  $\text{SiO}_2$ . Since multiple re-entries of

**Table 4.1: Average number of ionized shells per track** caused by electrons with kinetic energy  $E$ . Electrons are tracked until they reach an energy of 4 eV. The values were computed with  $10^5$  incident electrons and include ionization by secondary electrons.

<b>E [keV]</b>	<b>K</b>	<b>L<sub>1</sub></b>	<b>L<sub>2</sub></b>	<b>L<sub>3</sub></b>	<b>M</b>
5	0.03	1.5	3.1	6.2	1281
15	0.5	4.6	9.8	19.4	3837
18	0.64	5.6	11.8	23.4	4604
25	1.0	7.8	16.5	32.8	6392
35	1.6	10.9	23.5	46.3	8948

**Table 4.2: Shakeoff probability**  $P_{SO}(x)$  to emit an electron with energy  $E_{SO}(x)$  after an ionization in shell  $x$  for silicon [83].

<b>shell x</b>	<b>K</b>	<b>L<sub>1</sub></b>	<b>L<sub>2,3</sub></b>	<b>M</b>
<b>P<sub>SO</sub>(x) [%]</b>	19.75	9.45	9.65	4.4
<b>E<sub>SO</sub>(x) [eV]</b>	19.2	6.25	6.65	2.2

**Table 4.3: Transition probabilities for K-shell vacancies.** The transition chain with their relative probability and the remaining vacancies are listed [83].

	<b>KL<sub>1</sub>L<sub>1</sub></b>	<b>KL<sub>1</sub>L<sub>2,3</sub></b>	<b>KL<sub>2,3</sub>L<sub>2,3</sub></b>	<b>KL<sub>1</sub>M</b>	<b>KL<sub>2,3</sub>M</b>	<b>KMM</b>
<b>probability (%)</b>	19.2	38.9	23.3	7.5	10.4	0.8
<b>vacancies</b>	L <sub>1</sub> , L <sub>1</sub>	L <sub>1</sub> , L <sub>2,3</sub>	L <sub>2,3</sub> , L <sub>2,3</sub>	L <sub>1</sub> , M	L <sub>2,3</sub> , M	M, M

**Table 4.4: Transition probabilities for L-shell vacancies.** The transition chain with their relative probability and the remaining vacancies are listed [83].

	<b>L<sub>1</sub>MM</b>	<b>L<sub>1</sub>L<sub>2,3</sub>M</b>	<b>L<sub>2,3</sub>MM</b>
<b>probability (%)</b>	2.5	97.5	100
<b>vacancies</b>	M, M	L <sub>2,3</sub> , M	M, M

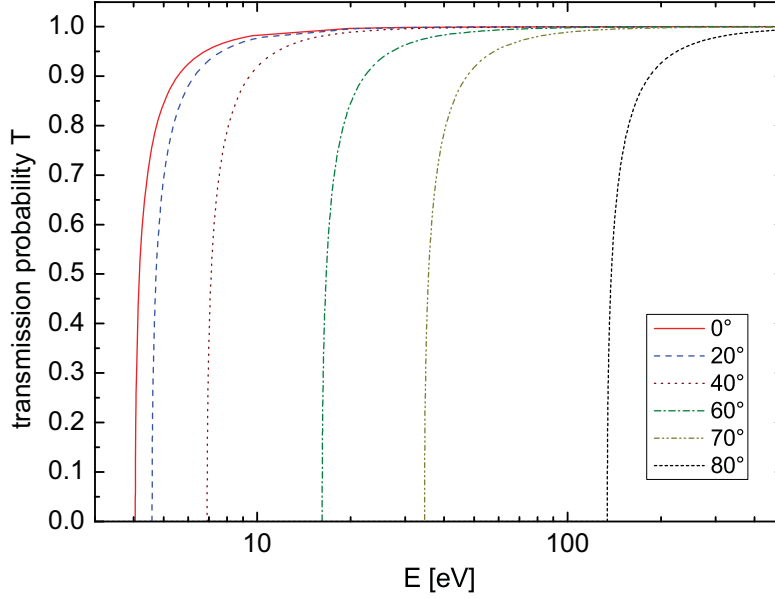


**Figure 4.8:** The transmission probability at the silicon-vacuum interface in dependence on the electron energy  $E$  and the incident angle  $\theta$ . A step potential of  $\chi = 4.05$  eV was assumed.

backscattered electrons occur through the electromagnetic design of the spectrometers, great care is taken in surface preparation and general detector handling. The detectors are only cooled and operated in ultra-high vacuum conditions to prevent contamination.

As a basic and general model for the vacuum-to-solid border, a potential step with height  $V$  at  $z = 0$  is assumed for KESS. Furthermore, the conduction band minimum  $E_{\text{CBM}}$  (Fig. 4.6) inside the silicon is assumed to be constant [95] and independent from the temperature. Electrons crossing the step have a probability  $T$  to be transmitted and  $1 - T$  to be reflected depending on their incident energy  $E$  and incident angle  $\theta$  at the surface barrier.

The transmission probability is derived from the continuity of the wave function at  $z = 0$  as

$$T = \begin{cases} 4A / (1 + A)^2 & \text{if } E \cos^2 \theta \geq V \\ 0 & \text{otherwise} \end{cases} \quad (4.31)$$

$$\text{with } A = \sqrt{1 - \frac{V}{E \cos^2 \theta}},$$

and is shown in Figure 4.8.

For each crossing of the barrier, a uniformly distributed random number  $R$  is thrown. The electron is transmitted if  $R < T$  and a new polar angle  $\theta_T$  is derived from the

momentum conservation parallel to the surface:

$$\cos^2 \alpha = \frac{E \cos^2 \theta - V}{E - V} \quad (4.32)$$

and

$$\theta_T = \begin{cases} \alpha & \text{if } \theta < \frac{\pi}{2} \\ \pi - \alpha & \text{if } \theta > \frac{\pi}{2} \end{cases}. \quad (4.33)$$

For  $R > T$ , the electron is reflected with a new angle  $\theta_R$

$$\theta_R = \pi - \theta. \quad (4.34)$$

Since the potential energy is changed for transmitted electrons, the new kinetic energy  $E_T$  is

$$E_T = E - \chi. \quad (4.35)$$

Equations 4.31 to 4.35 are valid for both directions approaching a step function, if  $V = \chi$  for entering and  $V = -\chi$  for leaving the silicon is used. For pure crystal silicon, the electron affinity is  $\chi = 4.05$  eV [95].

The influence of the surface barrier on the backscattering yield and the energy distribution is only observable below  $\sim 500$  eV as indicated by Figure 4.8. It will be shown in Section 5.2 that the transmission probability and the electron affinity are important for the 'true' secondary electron peak ( $E_{BS} < 50$  eV) in the energy spectrum of backscattered electrons.

The detector response is not influenced significantly by the transmission probability  $T$  *itself*, since reflected electrons have only a small chance to travel from the dead layer to the sensitive detector regions. However, the *electron affinity* does influence the complete detector response, since it is shifted by  $\chi$  following Eq. 4.35. The tracking of reflected electrons is continued, since they have a chance to escape the silicon in subsequent attempts.

## 4.5 Electron track generation

It can be assumed that electron scattering is a stochastic process. In traversing a path of length  $s$  the mean number of collisions is  $y = s/\lambda$ . The probability for a number of collisions  $k$  along  $s$  is given by the Poisson distribution

$$P_k(y) = \frac{y^k}{k!} e^{-y}. \quad (4.36)$$

For  $k=0$  (no collision), Equation 4.36 becomes the exponential distribution  $P_0(y) = e^{-y}$ . Then  $s$  is the free path or *step length*, and  $\lambda$  is the *mean free path*. The probability density function (PDF)  $p(s)$  of this exponential distributions is

$$p(s) = -\frac{1}{\lambda} e^{-\frac{s}{\lambda}} \quad (4.37)$$

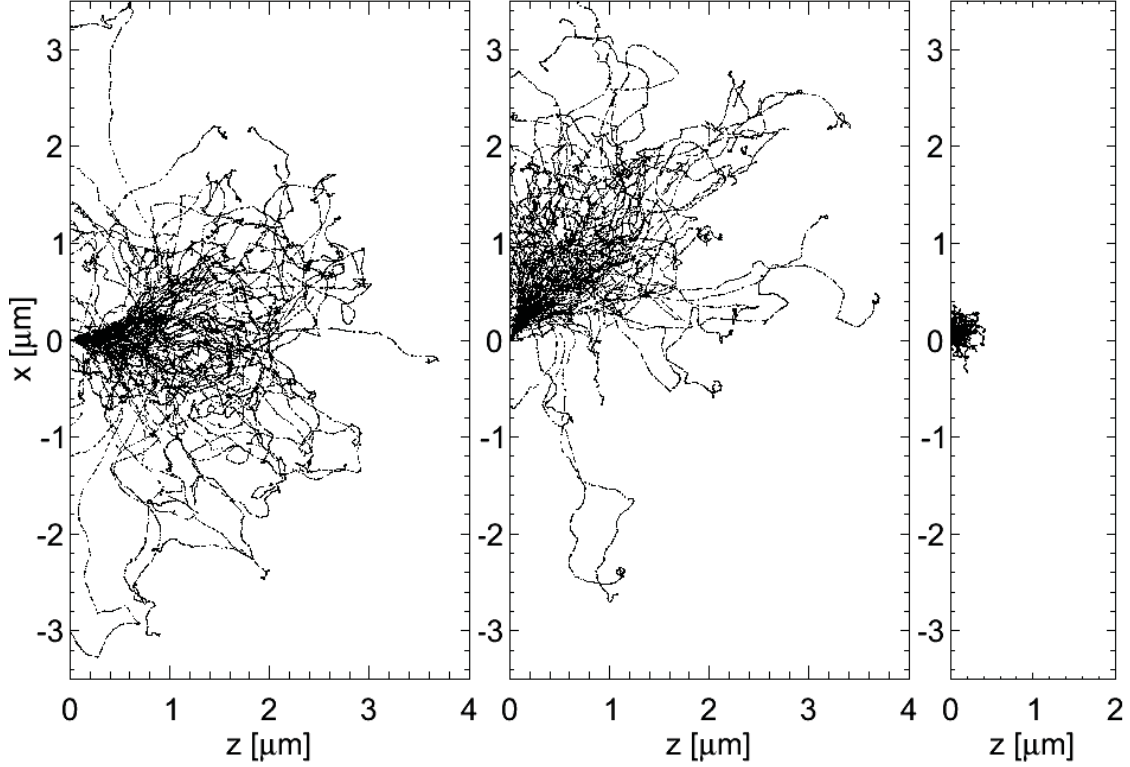


**Figure 4.9: Simulated tracks of electrons in Si** mapped to the  $x$ - $z$ -plane. The points represent the position of inelastic collisions. Elastic collisions are simulated but not marked in the plot. Electrons enter the detector at  $x = z = 0$  in  $z$ -direction. Backscattered electrons exit the detector at  $x \neq 0$ . **(left)** Incident angle  $\theta_I = 0^\circ$  and incident energy  $E_I = 18$  keV, **(center)**  $\theta_I = 60^\circ$  and  $E_I = 18$  keV, **(right)** a typical backscattered electron re-entering the detector with  $\theta_I = 45^\circ$ ,  $E_I = 5$  keV.

The cumulative distribution function (CDF) is

$$F(s) = \int_0^s p(s') ds' = 1 - e^{-s/\lambda} \quad (4.38)$$

Using the inverse transform method to replace  $F(s)$  with random numbers  $R$  uniformly distributed in  $[0,1]$  and solving for  $s$  yields the sampling formula

$$s(R) = -\lambda \ln(1 - R) \equiv -\lambda \ln R \quad (4.39)$$

The total mean free path  $\lambda$  is related to the inelastic mean free path  $\lambda_{\text{in}}$  and the elastic mean free path  $\lambda_{\text{el}}$  by

$$\lambda^{-1} = \lambda_{\text{el}}^{-1} + \lambda_{\text{in}}^{-1}. \quad (4.40)$$

For each step, a random number  $R_1$  is thrown determining the steplength  $s$  from Eq. 4.39. The collision is elastic, if  $R_1 < \lambda_{\text{el}}/\lambda$ . Otherwise, the collision is inelastic.

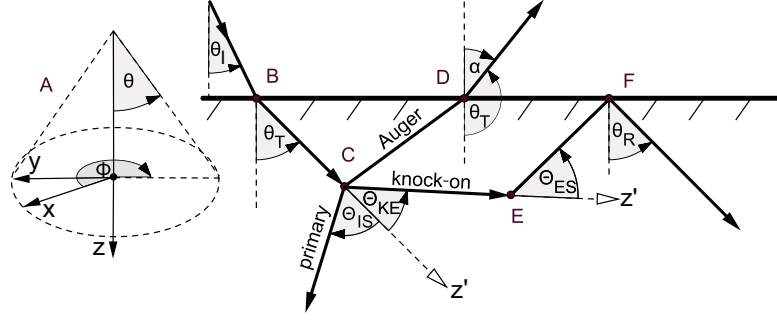


**Figure 4.10: Overview of angles used in the simulation.** (A) Solid sample coordinates  $(x, y, z, \theta, \phi)$  with the surface at  $z = 0$ . The moving electron frame is  $(x', y', z', \Theta, \Phi)$ . (B) Refraction of the electron when entering silicon with transmitted electron angle  $\theta_T$ . (C) Inelastic scattering deflects the primary electron by  $\Theta_{IS}$ . A knock-on electron is emitted with an angle  $\Theta_{KE}$ . The silicon atom relaxes by isotropically emitting an Auger electron at  $\theta_{AE}$ . (D) Electron leaving the silicon with angle  $\theta_T = \pi - \alpha$ . (E) Elastic scattering deflects the electron by  $\Theta_{ES}$ . (F) Reflection of an electron at the silicon surface with emergent angle  $\theta_R$ .

In case of elastic scattering, the polar scattering angle  $\Theta_{ES}$  relative to the incident electron direction is sampled from the probability density function obtained from Eq. 4.22. The relative azimuthal scattering angle  $\Phi_{ES}$  is sampled isotropically from

$$\Phi_{ES} = 2\pi R_2 \quad (4.41)$$

with a random number  $R_2$ , because there is no distinguished plane for the scattering. The direction of the electron is changed and the step is finished.

In case of inelastic scattering, the energy loss  $\Delta E$  is determined by Eq. 4.9 and is subtracted from the kinetic electron energy  $E$ . After each inelastic collision, the polar scattering angle  $\Theta_{IS}$  is calculated from

$$\sin(\Theta_{IS}) = \sqrt{\frac{\Delta E}{E}}, \quad (4.42)$$

following the binary collision model. The relative azimuthal angle  $\Phi_{IS}$  is sampled following Eq. 4.41. The direction and energy of the electron is changed, secondary electrons are produced and the step is finished.

Scattering angles  $\Phi_{sc}$  and  $\Theta_{sc}$  in the reference frame moving with the electron  $(x', y', z', \Theta, \Phi)$ , with  $z'$  parallel to the electron momentum, are transformed to the reference frame of the silicon solid  $(x, y, z, \theta, \phi)$  by calculating the new direction  $\vec{p}$  with

$$p_z = A \cos \theta + \cos \Phi_{sc} \cos(\Theta_{sc} + \theta) \quad (4.43)$$

$$p_x = A \sin \theta \cos \phi + \cos \Phi_{sc} \sin(\Theta_{sc} + \theta) \cos \phi + \sin \Phi_{sc} \sin \Theta_{sc} \sin \phi \quad (4.44)$$

$$p_y = A \sin \theta \sin \phi + \cos \Phi_{sc} \sin(\Theta_{sc} + \theta) \sin \phi - \sin \Phi_{sc} \sin \Theta_{sc} \cos \phi \quad (4.45)$$

and

$$A = \cos \Theta_{\text{sc}}(1 - \cos \Phi_{\text{sc}}) \quad (4.46)$$

Several simulated tracks for electrons in silicon are shown in Figure 4.9. An overview of the various angles used in this chapter and in the simulation is given in Figure 4.10.

## 4.6 KESS in the global KATRIN simulation framework Kassiopeia

To simulate stand alone components, commissioning experiments and the complete KATRIN setup, the global simulation framework *Kassiopeia* was developed by the KATRIN collaboration. It consists of three logical parts:

1. particle generation (e.g. *KPAGE*)
2. particle tracking (e.g. *KTRACK*)
3. particle detection (e.g. *KESS*)

Particles can be generated with given distribution of angles and energies from various sources, such as electrons emitted from e-guns and spectrometer walls, and especially  $\beta$ -decay from the WGTS [96, 97, 98, 99]. Pre-calculated electric and magnetic fields from the actual experimental geometry are used as the input for the Lorentz equation (Eq. 4.47), which is solved with *KTRACK* [100, 99, 101]. The motion of the electron in an electric field  $\vec{E}$  and a magnetic field  $\vec{B}$  is fully described by the Lorentz force

$$\vec{F} = e \left( \vec{E} + \vec{v} \times \vec{B} \right). \quad (4.47)$$

For a MAC-E filter and in the adiabatic approximation, this results in three separate motions (Fig. 4.11), often called magnetron motion:

- An axial movement along the magnetic field line. Electrons are accelerated or decelerated by the electric field (Sec. 2.3).
- A helical cyclotron motion around the magnetic field line.
- A radial magnetron drift around the spectrometer symmetry axis.

Scattering with gas molecules can also be included in the simulation while tracking the particle through the KATRIN beam line.

Particle detection is handled by *KESS* and a DAQ-simulation currently under development. *Kassiopeia* and all its components are written in object-oriented *c++*, which allows for high flexibility and a large area of application. *Kassiopeia* and its predecessors have been successfully used to model various experimental setups and to answer design questions. Two examples for the application of *KESS* in *Kassiopeia* are given in Chapter 6.

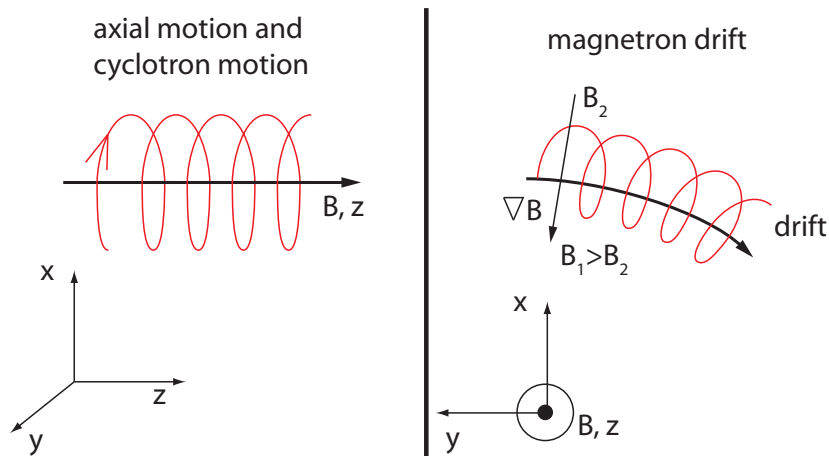


**Figure 4.11: Magnetron motion in inhomogeneous magnetic fields.** No electric field is present. **(left)** Viewed from the side of the spectrometer. The guiding center follows the magnetic field line. The electron performs a cyclotron motion around the  $z$ -axis. **(right)** The cross section of the spectrometer is shown. The cyclotron motion around the magnetic field causes an oscillation of the electron between lower ( $B_2$ ) and higher magnetic fields ( $B_1$ ). This results in a magnetron drift  $\vec{B} \times \nabla|\vec{B}|$  of the guiding center around the symmetry axis of the spectrometer.

*Kassiopeia* uses the mathematical functions of the ROOT package [102] as well as the ROOT file format. The random number generator used in *Kassiopeia* (and therefore *KESS*) is based on a Mersenne Twister algorithm [103] and is implemented in ROOT in the `TRandom3` class.

A *KESS* simulation of  $10^6$  primary particles with energy  $E = 18 \text{ keV}$  and normal incidence will take 15 minutes on a single processor core with secondary production disabled. With secondary production enabled and standard settings (Tab. A.1), the computation time is 35 h. The computation time is strongly correlated with the minimum tracking energy. The computation times stated here were obtained with a minimum tracking energy of 4 eV.

## 5 KESS benchmarks and results

Here, the simulation described in Chapter 4 is evaluated and compared to published experimental data. Included are the influence of secondary electrons (delta rays, Sec. 5.1), backscattering (Sec. 5.2) and dead layer effects (Sec. 5.3) on the detector response.

While primary electrons are losing energy along their track, not all energy is deposited where it is lost. It can be carried away by secondary electrons produced by ionization or Auger effect and deposited elsewhere. This is especially important for dead layer and backscattering effects. Here, the influence of the detailed modeling of secondary electrons on the energy deposition in the dead layer and the sensitive volume, as well as on the backscattered electron energy distribution is shown. Apart from the application in KATRIN, the ability to model very thin layers and produce secondary electrons in an event-based way allows the use of KESS for transmission electron energy-loss spectroscopy (TEELS)

The absolute electron backscattering is usually described by two ratios. The *primary* backscattering coefficient is the ratio of the number of incident electrons to the number of backscattered electrons with energies *greater* than 50 eV. The *secondary* backscattering yield is defined as the ratio of the number of incident electrons to the number of backscattered electron with energies *less* than 50 eV. Both ratios are calculated with KESS and are compared with several experiments for different incident energies. The secondary backscattering yield depends strongly on the electron affinity of the specimen and the associated surface escape process. This well known fact is the base of the x-ray photoelectron spectroscopy (XPS) technique to examine surfaces. Additionally, to validate KESS, the dependence of the primary backscattering yield on the electron angle of incidence is compared to experimental data. While the results are generally in good agreement with the experiments and do reflect the trends observed in experiments well, some systematic offsets can be observed. Unfortunately, the available experimental results are published without an estimate of systematic errors. The measurements are from the sixties and seventies, thus it has not been possible to discuss experimental questions. Comparable, more recent experiments [104] with non-silicon specimen estimate a relative systematic error of 10% on the primary backscattering coefficient. With this uncertainty, results from simulation and experiment are in agreement.

The situation is better for the energy distribution of backscattered electrons. High quality data of a spectroscopic measurement with a relative energy resolution of  $\Delta E_{\text{FWHM}} = 0.24\%$  are available [61]. The corresponding simulation shows all

effects observed in the experiment: Fully elastic backscattering, plasmon peaks, Auger peaks and the 'true' secondary electron peak. The detailed description of the backscattered energy spectrum means that **KESS** can be used to model results from Auger electron spectroscopy (AES) or reflective electron energy-loss spectroscopy (REELS).

Another important parameter for KATRIN is the angular distribution of backscattered electrons. The polar angle of backscattering defines the component of the kinetic electron energy parallel to the magnetic field. As mentioned before, the electromagnetic design of the main spectrometer and focal plane detector region is very sensitive to this component. The observed polar and azimuthal angles of backscattering, as well as the energy distribution of backscattered electrons with respect to the polar angle are discussed in Section 5.2.4. Angular-resolved electron energy-loss spectroscopy (AREELS) exploits this dependence of the backscattered energy distribution on the polar backscattering angle.

To investigate the influence of dead layers on the detector response, several models for their geometry (i.e. spatial charge collection efficiency) are presented and evaluated.

## 5.1 The influence of secondary electrons

Secondary electrons are created by ionization or excitation of silicon atoms (knock-on electrons or delta rays) and the subsequent re-arrangement of the shell electrons (Auger electrons). As discussed in Section 4.1, secondary electrons can deposit energy away from the primary particle track.

To give an overview of quantities needed for the detailed description of the detector response, the tracks of primary electrons with  $E_1 = 18 \text{ keV}$  were simulated. The distribution of the kinetic energy of outgoing backscattered electrons (Fig. 5.2), and the energy deposited by those backscattered electrons in the dead layer (Fig. 5.1(a)) and sensitive volume (Fig. 5.1(b)) has been calculated with simulations. The energy deposited in the sensitive volume folded with the energy resolution is the detector response of a detector. The three distributions in each figure are:

- **Primary electrons (PE):** Only the incident (primary) electrons are followed in the simulation. No secondary electrons are created. The energy lost by the primary in a single collision is deposited locally. The individual *energy losses* are treated as deposited energy and are summed along the track of the primary electron.
- **Individual electrons (IE):** Additionally to the primary electrons, secondary electrons from ionization and the Auger effect are included and followed. For all electrons, only that part of the energy lost in a single inelastic collision is deposited locally, which is *not* carried away by the emitted knock-on electron

and Auger electrons. The individual, localized *energy deposits* along an electron track are summed for each electron. Primary and secondary electrons are treated equally.

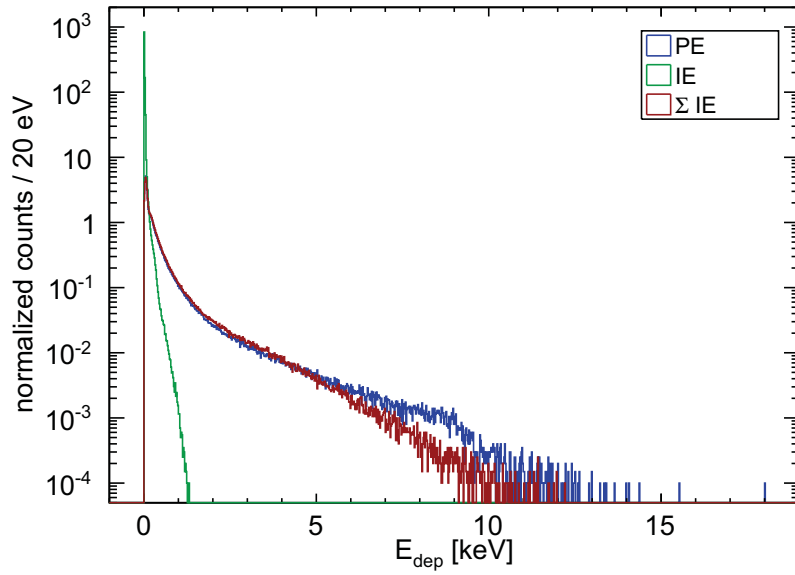
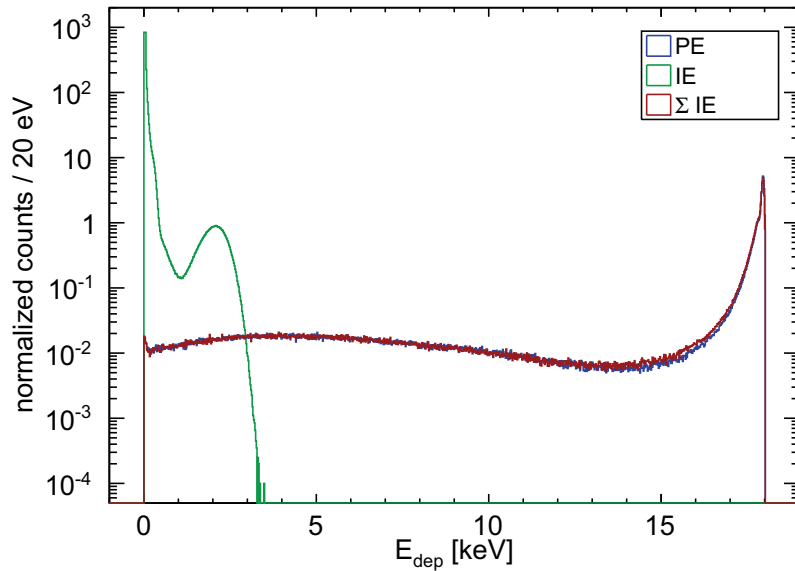
- **Sum over individual electrons ( $\Sigma$ IE):** Secondary electrons from ionization and the Auger effect are created and followed. The *energy deposits* described above are summed for each individual electron track. However here, all energy deposits of the primary electron and all secondaries it produced are again summed up. Therefore, only one entry in the energy distribution is produced per primary, which is the effect observed in real detectors: All energy deposits from the primary and its secondaries are collected and analyzed as one signal.

For the dead layer and the sensitive volume, the categories PE and  $\Sigma$ IE can therefore be seen as a simulation neglecting secondary electrons (PE), or including secondary electrons ( $\Sigma$ IE). Note that in the simulation, the energy is deposited at the point of the collision. A single energy deposit can thus be assigned either to the dead layer or to the sensitive volume

Figure 5.1(b) shows the distribution of the energy deposited in the sensitive volume. The distributions of PE and  $\Sigma$ IE show the expected behavior also observed in measurements. In the sensitive volume, a strong peak at the incidence energy is observed. Its low-energy tail is caused by energy losses in the dead layer. A plateau of partial energy deposits by backscattered electrons is visible for  $E_{\text{dep}} < 10$  (see also Fig. 4.1). Differences in these distributions are only found for the low-energy tail of the peak which are described below. The distribution of individual electrons (IE) is not of practical interest for measurements. However, it shows the total energy deposited for each individual electron in the simulation, including the incident primary. The absence of energy deposits above 4 keV per electron emphasizes that the distribution PE is based on energy loss and not energy deposit. It is clear from IE that the primary electron too does not deposit more than  $E_{\text{dep}} < 4 \text{ keV}$  along its track, although it does lose all its energy  $E_1$ . The difference of  $E_1 - E_{\text{dep}}$  for the primary was transferred to secondary electrons.

The energy deposit in a step function dead layer  $\lambda_D = 100 \text{ nm}$  for electrons with energy  $E_1 = 18 \text{ keV}$  is shown in Figure 5.1(a). While the distributions of PE and  $\Sigma$ IE agree for the low-energy peak, they show a different slope towards higher deposited energies  $E_{\text{dep}}$ . The distribution of energy deposited by PE is generally greater for  $E_{\text{dep}} > 5 \text{ keV}$ . This is again understandable from the difference of lost and deposited energy. For both distributions the primary electron loses the same energy in the dead layer, but the energy deposition differs. For  $\Sigma$ IE, the created secondary electrons take a part of the energy lost by the primary with them, and move into the sensitive volume or leave the detector. It is easier for high-energy secondary electrons to escape the dead layer, since their range is longer. Therefore, the difference is more pronounced at larger energy losses.

The competing effect is seen for  $E_{\text{dep}} < 5 \text{ keV}$ . Secondary electrons created in the

(a) energy deposited  $E_{\text{dep}}$  in the dead layer(b) energy deposited  $E_{\text{dep}}$  in the sensitive volume

**Figure 5.1: Energy deposit by electrons with energy  $E_I = 18$  keV in a detector** for three simulation modes. Shown are primary electrons (PE), individual electrons including secondary electrons (IE), and the sum of individual electrons ( $\Sigma$ IE). For  $\Sigma$ IE, all energy deposits by the primary and secondary electrons are summed and assigned to the primary electron. IE is only of scientific interest here. **(a)** Energy deposited in a step function dead layer with thickness  $\lambda_D = 100$  nm (for definition see Sec. 5.3.1). **(b)** Energy deposited in the sensitive volume. IE or  $\Sigma$ IE folded with the energy resolution is the detector response.

sensitive volume move to the dead layer and deposit energy there. These secondary electrons can come from a depth more than one dead layer thickness deeper into the sensitive volume, although with a lower average energy. Thus, the slope of the distribution  $\Sigma\text{IE}$  is steeper than PE for  $E_{\text{dep}} < 5 \text{ keV}$ .

The overall influence of the simulation of secondary electrons is thus also visible in the energy deposit in the sensitive volume in the low-energy tail (Fig. 5.1(b)). The tail for PE has a steeper slope; on average, less energy is deposited in the dead layer. In conclusion, a simulation *not* including the creation of secondary electrons effectively decreases the dead layer effect.

In Chapters 5 and 6, a region of interest (ROI) with  $15 < E_{\text{dep}} < 21 \text{ keV}$  is used to obtain the detection efficiency  $\varepsilon$ . The efficiency  $\varepsilon$  is defined as the number of electrons  $N_{\text{ROI}}$  in the region of interest, normalized to the number of incident electrons  $N_{\text{I}}$ . To investigate the influence of secondary electrons on the detection efficiency,  $\varepsilon$  was calculated for a simulation with primaries only (PE) and the creation of secondaries ( $\Sigma\text{IE}$ ):

$$\varepsilon_{\text{PE}} = 0.8049 \pm 9 \times 10^{-4} \text{ for PE} \quad (5.1)$$

$$\varepsilon_{\Sigma\text{IE}} = 0.8040 \pm 9 \times 10^{-4} \text{ for } \Sigma\text{IE}. \quad (5.2)$$

The detection efficiencies agree inside their statistical errors. This agreement does not depend on the incident energy  $E_{\text{I}}$ , since secondary electrons can only have a maximum kinetic energy of  $E_{\text{I}}/2$ . The inclusion of a reasonable energy resolution ( $\Delta E_{\text{FWHM}} < 4 \text{ keV}$ ) does not change this agreement.

The creation of secondaries can thus be neglected for *detection efficiency* calculations, which is a big advantage with regard to CPU time (Sec. 4.6). Secondary electrons should be included for the simulation of the *detector response*, since they effectively change the shape of the energy spectrum. Of course, the need for the simulation of secondaries depends on the energy resolution and therefore the lower detection threshold of the detector.

For the energy distribution of backscattered electrons, the situation is different. While all the charge carriers created by energy deposits in the detector are collected to form the signal, electrons leaving the detector have to be treated individually. Thus,  $\Sigma\text{IE}$  is not useful here and is only shown for consistency. The energy distribution for backscattered electrons produced by incident electrons with  $E_{\text{I}} = 18 \text{ keV}$  is shown in Figure 5.2. As shown in Section 5.2.3, the distribution of individual electrons including secondary electrons (IE) shows very good agreement with measurements. The distribution of primary electrons (PE) and individual electrons (IE) show good agreement above 9 keV. At lower backscattered energy  $E_{\text{BS}}$ , the differences increase. This is due to the fact that the primary electrons can only lose half of their energy in a single collision. Therefore the contribution of secondary knock-on electrons to the backscattered electron energy spectra starts at 9 keV and increases to lower energies. At 1.8 keV an Auger K-Shell peak is visible. Since PE does not produce any secondary electrons, the contribution of secondary electrons is

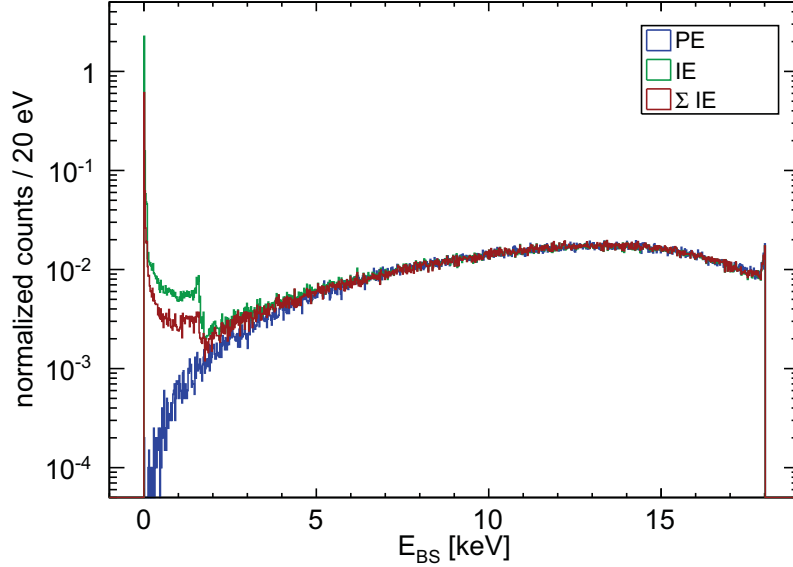


**Figure 5.2: Simulated energy distribution of backscattered electrons** for incident electrons with  $E_I = 18$  keV. The backscattered electron energy  $E_{BS}$  is shown for primary electrons (PE), individual electrons (IE) including secondary electrons, and the sum of individual electrons ( $\Sigma$ IE). For  $\Sigma$ IE, all energy deposits by the primary and secondary electrons are summed and assigned to the primary electron.  $\Sigma$ IE is not useful for backscattered electrons. The difference between the distributions IE and PE is the contribution of secondary electrons. At  $E_{BS} \approx 1.8$  keV, a K-Shell Auger peak is visible. Note the magnitude of the 'true' secondary electron peak at  $E_{BS} < 50$  eV.

the difference between IE and PE. Note the magnitude of the 'true' secondary electron peak at  $E_{BS} < 50$  eV. In conclusion, for backscattering effects, electrons should be treated individually (IE). Simulating primary electrons (PE) only is a valid approximation, if only the highest backscattered electron energies are of interest.

## 5.2 Backscattering from the detector surface

Incident electrons have a probability of being backscattered from solids, depending on the absorber material, the electron incident angle  $\theta_I$  and the electron incident energy  $E_I$ . From a simulation point of view, the probability depends on the energy losses, the associated deflection and the elastic deflection. For energies  $E < 500$  eV, the surface escape effect has to be included and the electron affinity becomes important (Fig. 4.8).

The literature distinguishes between primary electron backscattering and 'true' secondary electron backscattering [105]. It has to be noted that this nomenclature is coming from experiments, where it is impossible to know the origin of backscattered

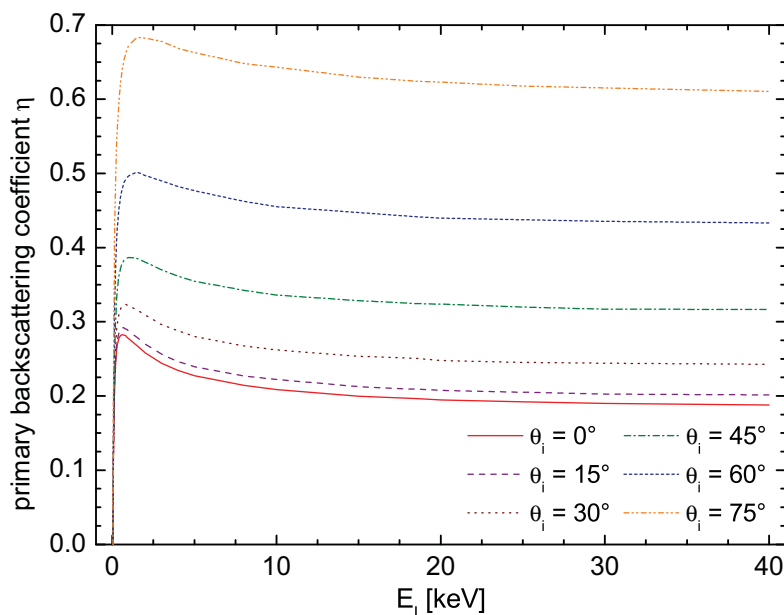


**Figure 5.3:** The primary backscattering coefficient  $\eta$  for electron incidence on silicon calculated with KESS.  $\eta$  is shown for incident energies  $E_I < 40$  keV and incident angles  $\theta_I < 75^\circ$ .

particles<sup>1</sup> and must not to be mistaken with primary and secondary electrons in simulations. The primary backscattering coefficient  $\eta$  is defined as the ratio of the incident electrons to the sum of all electrons emitted from the specimen surface with an energy  $E_{BS} > 50$  eV (Sec. 5.2.1). The secondary backscattering yield  $\delta$  is defined respectively for backscattered electrons with  $E_{BS} < 50$  eV (Sec. 5.2.2). With the initial electron, additional knock-on and Auger electrons, these ratios are allowed to be greater than one.

Energy spectra of backscattered electrons show the characteristics of the physics processes used in the simulation. The elastic peak, plasmon peaks, Auger lines and the 'true' secondary peak ( $E_{BS} < 50$  eV) can be observed and compared to experiments (Sec. 5.2.3).

### 5.2.1 Primary backscattering coefficient $\eta$

The primary backscattering coefficient  $\eta$  is the ratio of electrons emitted from silicon with an energy  $E_{BS} > 50$  eV to the number of incident electrons. Figure 5.3 shows the primary backscattering coefficient  $\eta$  for different incident angles  $\theta_I$  and incident energies  $E_I$  calculated with KESS. For incident energies  $15 < E_I < 40$  keV the primary backscattering coefficient  $\eta$  is almost constant. However, especially for  $\theta_I > 30^\circ$  a strong correlation of  $\eta$  with the incidence angle  $\theta_I$  can be observed. For a typical

<sup>1</sup>With the exception of Auger electron peaks and electrons with backscattered energy  $E_{BS} > E_I/2$ .

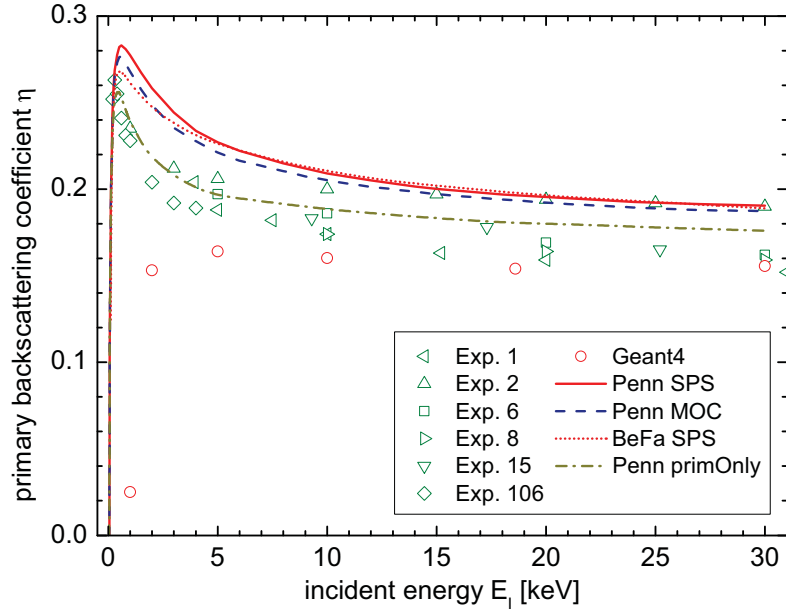


**Figure 5.4: The primary backscattering coefficient  $\eta$**  in dependence on the electron incident energy  $E_I$  for normal incidence. KESS results obtained with Penn’s (Penn) and Bethe-Fano’s (BeFa) inelastic collision cross sections, and knock-on secondary angle models based on spherical symmetry (SPS) and momentum conservation (MOC) are compared to experimental results collected in the D.C. Joy database [62]. Results from simulations with the **Geant4.9.1** low-energy package are shown. To emphasize the contribution of secondary electrons with a backscattered energy  $E_{BS} > 50$  eV, KESS results neglecting secondaries are also shown (PrimOnly). The numbers of the experiments given in the legend correspond to the references found in the database [62].

tritium  $\beta$  electron hitting the focal plane detector with  $E_I = 18.6$  keV and  $0^\circ < \theta_I < 45^\circ$ , the primary backscattering coefficient  $\eta$  ranges from 20% to 32%.

For evaluation, KESS is compared to a collection of experimental data. The D.C. Joy database on electron-solid interactions [62] covers primary and secondary backscattering for over 40 elements. Figure 5.4 shows a comparison of  $\eta$  between available experiments and KESS for incident energies  $0.06 < E_I < 30$  keV and  $\theta_I = 0^\circ$ .

To show the influence of the different models on how to determine the emittance angle of knock-on electrons during ionization processes (Sec. 4.3.1), results obtained with the spherical symmetry (SPS) and the momentum conservation (MOC) model are shown in Figure 5.4. Both use Penn’s inelastic cross sections (Penn). The relative difference of SPS to MOC is 3.8% at  $E_I = 2$  keV and is 1.8% on average over the whole energy range shown. SPS results are generally higher, since the SPS knock-on electrons are not focused in the direction of the ionizing electron. Therefore, electrons travelling from the detector surface into the silicon also contribute to backscattering through knock-on secondaries.

Simulations with the Bethe-Fano inelastic collision cross sections (BeFa) are shown in Figure 5.4. The average relative difference of Penn to BeFa results for  $E_I > 4$  keV is 0.6%. However, this agreement is misleading. It must be noted again that the primary backscattering coefficient  $\eta$  sums over the number of *all* backscattered electrons with energy  $E_{BS} > 50$  eV. Apart from that,  $\eta$  is not sensitive to  $E_{BS}$ . The distribution of backscattered electron energies is discussed in Section 5.2.3. With Bethe-Fano's inelastic collision cross sections, tracking is feasible down to electron energies of  $E_{min} \approx 100$  eV (Sec. 4.2.1). Thus, no electrons below  $E_{min}$  are created or backscattered. Since the contribution of electrons with  $50 < E_{BS} < 100$  eV becomes larger towards lower incident energies, the agreement below 4 keV is worse.

The contribution of knock-on and Auger electrons to the primary backscattering coefficient  $\eta$  is the relative difference between the KESS results including secondary production (Penn SPS) and the ones neglecting it (PrimOnly) (Fig. 5.4). The maximum relative contributions of secondary electrons to  $\eta$  is 15.6% at  $E_I = 2$  keV and is 8% on average. The contribution of secondary electrons to the backscattered electron energy distribution is discussed in Section 5.1.

Simulation results obtained with the **Geant4** low-energy package are shown in Figure 5.4. While in the incident energy region  $E_I > 5$  keV  $\eta$  shows agreement with experimental results, the characteristic rise at lower energies was not produced in **Geant4**. Additionally,  $\eta$  is no longer observable below 2 keV. This is caused by the fact that **Geant4** only tracks electrons with  $E > 250$  eV [106]. More importantly, a strong correlation on **Geant4** simulation parameters describing electron transport was found (see also [67, 68]). These are the step size limitation, the fraction of the allowed step size of the assumed particle range, and the parameter controlling the step size after a boundary crossing. With still reasonable parameter settings, it was possible to shift values from  $\eta$  over the whole range of experimental results. This indicates an intolerable systematic dependence on simulation parameters. KESS uses the physics models described in Chapter 4 where no such dependencies on technical simulation parameters can emerge.

The peak of  $\eta$  below incident energies of 5 keV observed in experiments is produced in all KESS simulation settings. This rise is caused by the decrease of the electron range (Fig. 4.4(a)). Additionally, the deflections in elastic collisions become larger at lower energies (Fig. 4.5(b)). Due to the wide spread of experimental values and missing experimental errors in [62] and other references, no statement can be given on the single simulations settings. Recent experiments with non-silicon specimen report relative errors larger than 10% [104]. In general, a good agreement with the data can be stated. To overcome the insensitivity of  $\eta$  on the backscattered energy  $E_{BS}$ , complementary comparisons to experimental energy distributions of backscattered electrons are needed (Sec. 5.2.3).

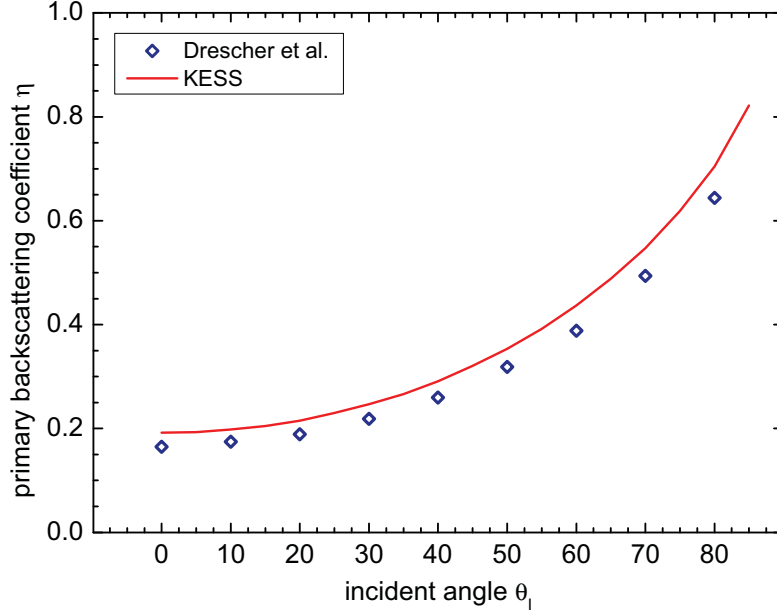


**Figure 5.5:** The primary backscattering coefficient  $\eta$  over the incident angle  $\theta_I$  with fixed incident energy  $E_I = 25$  keV. Results obtained with KESS are compared to experimental values from [107]. No experimental errors are stated in [107].

### Dependence of the primary backscattering coefficient $\eta$ on the electron incident angle $\theta_I$

One of the experiments [107] included in the D.C. Joy database also measured the primary backscattering coefficient  $\eta$  for different incident angles  $\theta_I$  at a fixed incident energy  $E_I = 25$  keV. Figure 5.5 compares the experimental results to KESS simulations. A very strong correlation of  $\eta$  on  $\theta_I$  is found in the experiment and simulation. For high incident angles, electrons are generally close to the surface (Fig. 4.9) and the primary backscattering coefficient becomes as large as  $\eta = 0.8$ . The detectors in the KATRIN experiment and especially the focal plane detector will see electrons with incident angles  $\theta_I \gg 30^\circ$ . Thus, it is crucial to know the angular distribution of the incident electrons in order to obtain a detailed detector response from simulations.

This is of importance, as most calibration measurements at KATRIN are made with artificial electron sources with fixed angle of emittance [108, 109]. On the other hand, this means that calibration data must be extrapolated to isotropic emission, e.g. as it is the case for the tritium source. While the shapes of simulation and experimental results are in good agreement, an average relative systematic difference between KESS results and the experimental values of  $-12.5\%$  is observed. Assuming an estimated relative systematic error larger than 10% given for a similar experiment [104], the agreement is acceptable.

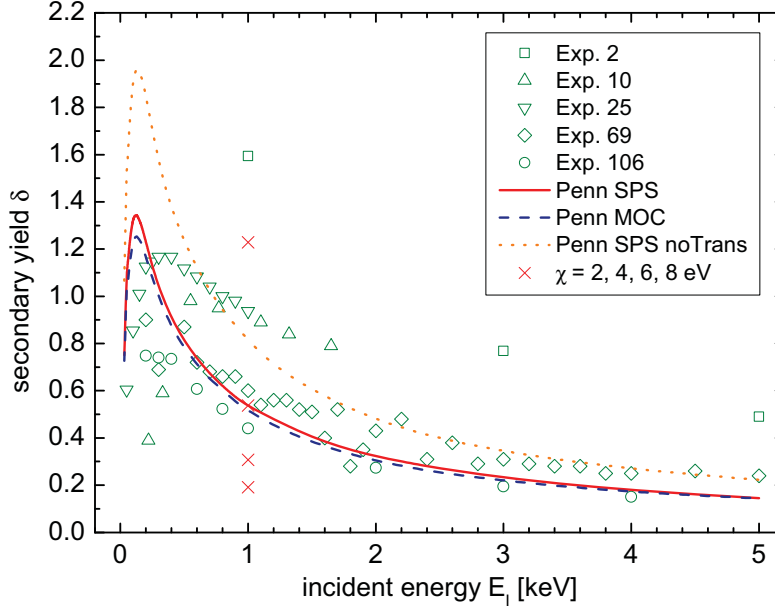


**Figure 5.6:** The secondary backscattering yield  $\delta$  over the electron incident energy  $E_i$  for normal incidence. KESS results obtained with the spherical symmetry (SPS) and momentum conservation model (MOC) for the generation of knock-on electrons during inelastic collisions are compared to experimental results included in the D.C. Joy database [62]. To show the influence of the surface escape process, results with a transmission probability  $T = 1$  are also plotted (noTrans). Additionally,  $\delta$  for different electron affinities  $\chi = 2, 4, 6, 8$  eV for  $E_i = 1$  keV are included.  $\delta$  increases with  $\chi$ . The numbers of the experiments given in the legend correspond to the references found in the database [62].

### 5.2.2 Secondary backscattering yield $\delta$

As mentioned above, the secondary backscattering yield  $\delta$  is the ratio of electrons emitted from silicon with a backscattered energy  $E_{BS} < 50$  eV to the number of incident electrons. Data for the secondary backscattering yield  $\delta$  from four experiments available in the D.C. Joy database [62] are compared to simulations (Fig. 5.6). KESS results with the spherical symmetry (SPS) and momentum conservation model (MOC) for the generation of knock-on electrons during inelastic collisions are shown. Similar to the primary backscattering coefficient, a peak of  $\delta$  at low incident energies is visible. It is explained by the decreasing electron range and increasing average deflection angles in elastic collisions with decreasing incident energy. For electron energies  $E < 100$  eV, the electron range increases again (Fig.4.5(a)).

One simulation was made without taking into account the surface escape process and thereby assuming a transmission probability from silicon to vacuum of  $T = 1$  (Fig. 5.6). The others include the surface escape process with an electron affinity  $\chi = 4.05$  eV. While the relative difference of the two simulations including surface

effects is 4.7% on average, it is 33% to the simulation neglecting it. This shows the influence of the surface escape process on  $\delta$  as expected from Figure 4.8 and hints to a strong dependence on the electron affinity  $\chi$ . The dependence is shown in Figure 5.6 for  $2 < \chi < 8$  eV and  $E_I = 1$  keV.

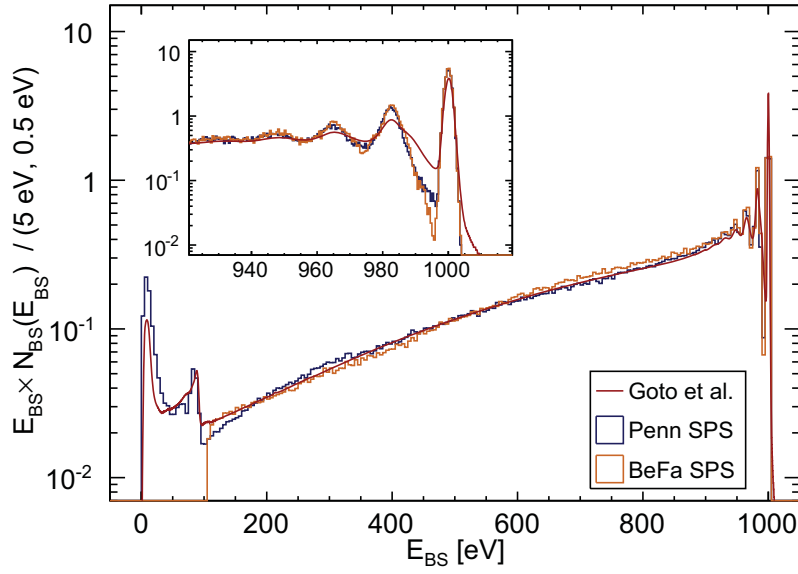
While the comparison to data shows the importance of including the surface escape process (Sec. 4.4), it also shows the strong dependence on the electron affinity  $\chi$ . Reasonable agreement for  $\delta$  between KESS simulations including the surface escape process and the experiments can be stated.

It should however be noted that the secondary backscattering yield is not a good benchmark. It depends strongly on surface effects, which makes it difficult to compare to simulations or even compare experiments among each other. The electron affinity (Sec. 4.4) is temperature dependent. It changes if, for example, a silicon oxide layer is passivating the silicon surface [110]. The electron affinity as well as the shape of the potential barrier of the surface are unknown parameters, until measured or calculated. For the KESS simulations, the literature value  $\chi = 4.05$  eV for clean crystalline silicon is used [95].

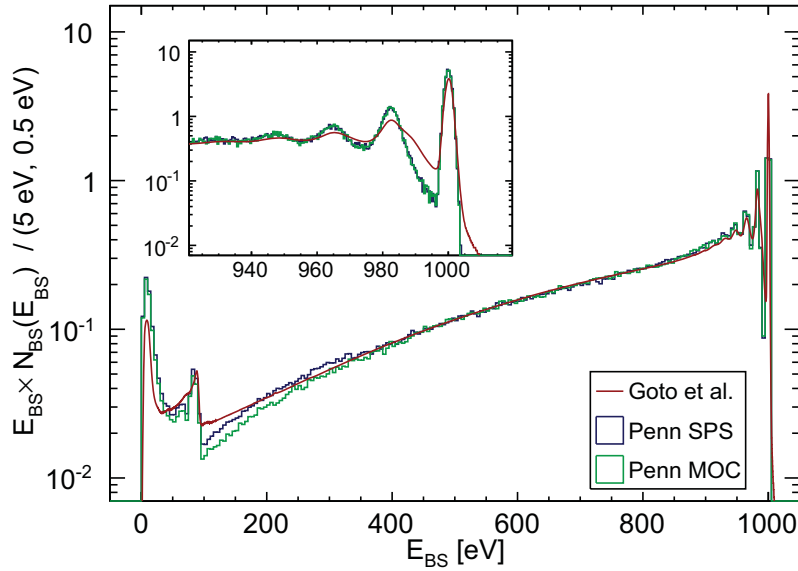
### 5.2.3 Energy spectra of backscattered electrons

The energy distribution of electrons emitted from silicon due to electron incident shows many physics effects and can be used as a check for simulations. Elastically backscattered electrons, plasmon peaks, inelastic energy loss, ionization and the Auger effect can be compared to experiments.

In Figure 5.7(b) a comparison is shown between simulated and experimental results for the number of backscattered electrons  $N_{BS} = N(E_{BS})$  in dependence on the backscattered electron energy  $E_{BS}$  for  $E_I = 1$  keV. The experimental results from [61] were obtained with a cylindrical mirror analyzer with an energy resolution of 0.24% and a faraday cup with an efficiency greater than 99%. To show the structures in the energy spectra, the  $N_{BS}$  spectrum is multiplied by  $E_{BS}$ . KESS results obtained with Penn's inelastic collision cross sections and spherical symmetry (SPS) and momentum conservation (MOC) model for the knock-on secondary electron angle are shown. Results obtained with Bethe-Fano's collision cross section are also included. Good agreement can be found in the higher energy region where the elastic peak and plasmon peaks are visible. The elastic peak is formed at  $E_I$  by electrons that were backscattered elastically only. The peaks visible at multiples of the plasmon energy  $E_P \approx 17$  eV below the elastic peak reflect the fact that plasmon excitations are the most probable energy loss mechanism in a single collision (Fig. 4.5(a) and [111, 112]). Below  $E_{BS} < 100$  eV, a pronounced L-shell Auger electron peak followed by the corresponding plasmon resonance is visible. The so-called 'true' secondary electron peak is observed below  $E_{BS} < 50$  eV. Penn's inelastic collision cross sections with SPS and MOC models show all effects visible in the experimental spectrum. However, the SPS model produces better agreement in the energy regime  $100 < E_{BS} < 500$  eV.



(a)



(b)

**Figure 5.7: Energy spectrum of backscattered electrons** with incident energy  $E_I = 1$  keV. KESS simulation results are compared to measurements from [61]. **(a)** Results obtained with Bethe-Fano's (BeFa) and Penn's (Penn) inelastic collision cross sections are shown. **(b)** Additionally, the influence of the *spherical symmetry* (SPS) and *momentum conservation* (MOC) model for the knock-on electron emittance angle is shown. Simulation counts were normalized to the number of incident electrons and multiplied by  $E_{BS}$ . Experimental values are normalized to match the average Penn SPS model counts in the interval  $450 < E_{BS} < 550$  eV.

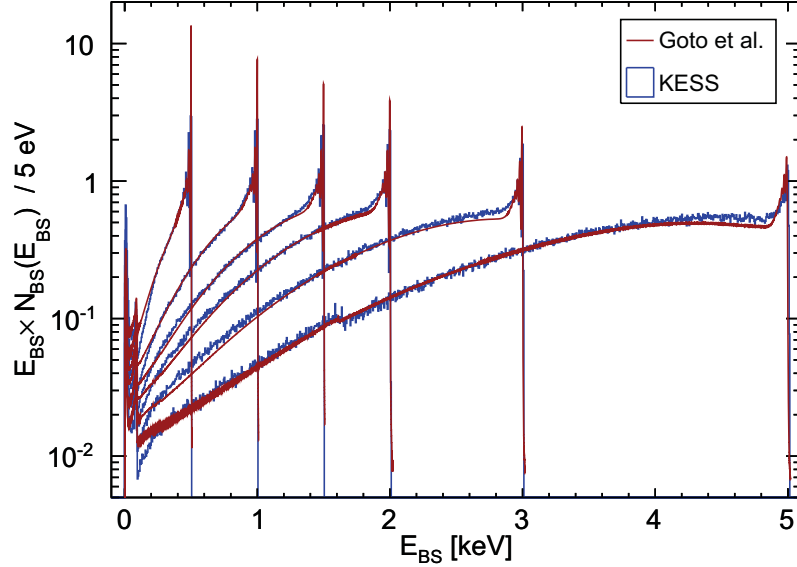


**Figure 5.8:** Energy spectrum of backscattered electrons in dependence on the electron incident energy  $E_I = 0.5, 1, 1.5, 2, 3, 5$  keV for normal incidence. KESS results obtained with Penn’s inelastic collision cross sections, and knock-on secondary angle model based on spherical symmetry (SPS) are compared to measurements from [61].

To evaluate the two inelastic collision cross section models examined in this study, results obtained with Penn SPS and Bethe-Fano SPS model are compared to an experiment (Fig. 5.7(a)). While reasonable agreement over the whole energy range is found, no backscattered electrons can be produced below 100 eV when using the Bethe-Fano model. Therefore, L-shell Auger electrons and the true secondary peak can not be described.

The simulation underestimates the count rate in the region between the elastic peak and the first plasmon peak ( $E_I - 17$  eV). In the experiment, a peak at  $E_I - 10$  eV is observed. The difference between experiment and simulation gets smaller with increasing incident energy  $E_I$ . Therefore, this difference is probably caused by energy losses through surface excitations which are not included in KESS. At the detector surface, surface plasmons with  $E_S = \hbar\omega_S \approx 11$  eV and surface-state transitions with  $E_{ST} \approx 2$  and 7.5 eV are expected. Obtained spectra from reflective electron energy-loss spectroscopy for a clean surface and after an exposure to  $O_2$  are shown in [113, Fig. 1]. The surface plasmon could explain the observed peak at  $E_I - 10$  eV.

In summary, Penn’s inelastic collision cross sections with the spherical symmetry model for knock-on electron generation produced the best results for backscattered electrons and should be preferred for incident energies  $E_I < 40$  keV.

More energy spectra of backscattered electrons [61] are shown in Figure 5.8. They cover an incident energy range from  $0.5 < E_I < 5$  keV. The agreement is reasonable for all available data. In the peak region, energy shifts by a few eV are observed.

Additionally, the simulation overestimates the number of backscattered electrons with an energy a few hundred eV below the elastic peak for high  $E_I$ . Note that the simulated spectra are normalized to match the experimental results around  $E_I/2$  since no absolute calibration is available from the measurement. Therefore, it is not certain at which  $E_{BS}$  the differences arise. Also it is unclear, if these differences are caused by simulation or experimental uncertainties. In conclusion, KESS shows good agreement with the available data and reproduces all observed features. However, more measurements are desirable to further evaluate KESS. Since such data are rarely published, a measurement campaign investigating the backscattering effects in detail is proposed.

### Spatial distribution of the energy of backscattered electrons

Besides the energy distribution of all backscattered electrons, the spatial distribution of the backscattered energy is of interest. Figures 5.9(a) to 5.9(c) show the total energy emitted from the detector surface from a mono-energetic electron beam with  $E_I = 18\text{ keV}$  and three polar incident angles  $\theta_I$ . The azimuthal incidence angle was kept at  $\phi_I = 0^\circ$ . The total energy was normalized to the number of incident electrons  $N_I$ . It can be regarded as an energy density  $dE/dA$ , where  $A$  is a small surface area. The maximum distance of backscattered electrons to the point of incidence ( $x = y = 0$ ) is just below  $5\mu\text{m}$ . The energy density is highest at the point of incidence and decreases towards the edge of the spatial distribution. For higher azimuthal incident angles  $\theta_I$ , the area of highest energy density is enlarged in the direction of the incoming electron beam.

The spatial distribution for increasing  $\theta_I$  is only significantly changed for high  $\theta_I$ , the distribution in  $x$  is not affected at all. The distribution in  $y$  is compressed for  $y < 0$  and marginally stretched for  $y > 0$ . This behavior is expected from the model used to determine the angles of emittance of secondary electrons. The SPS model based on spherical symmetry for knock-on electrons is used and Auger electrons are generally emitted randomly into  $4\pi$ . This means that the point of emittance of secondary electrons depends only on the position they were created. Beyond that, the secondary electron track is not correlated with the trajectory of the primary electron.

Figure 5.9(d) shows the total energy of backscattered electrons  $\Sigma E_{BS}$  normalized to the number of backscattered electrons  $N_{BS}$ . This yields the *average* backscattered electron energy for every position on the detector surface. Note that the energy distribution of backscattered electrons is broad and reaches from 1 eV to  $E_I$ . At the point of incidence, mostly low-energy secondaries are emitted. However, it is clear from Figure 5.9(a) that at this point the energy density is largest, too. It can be concluded that at the point of incidence a large number of low-energy electrons are backscattered.

Around the point of incidence, the average backscattered energy suddenly rises due

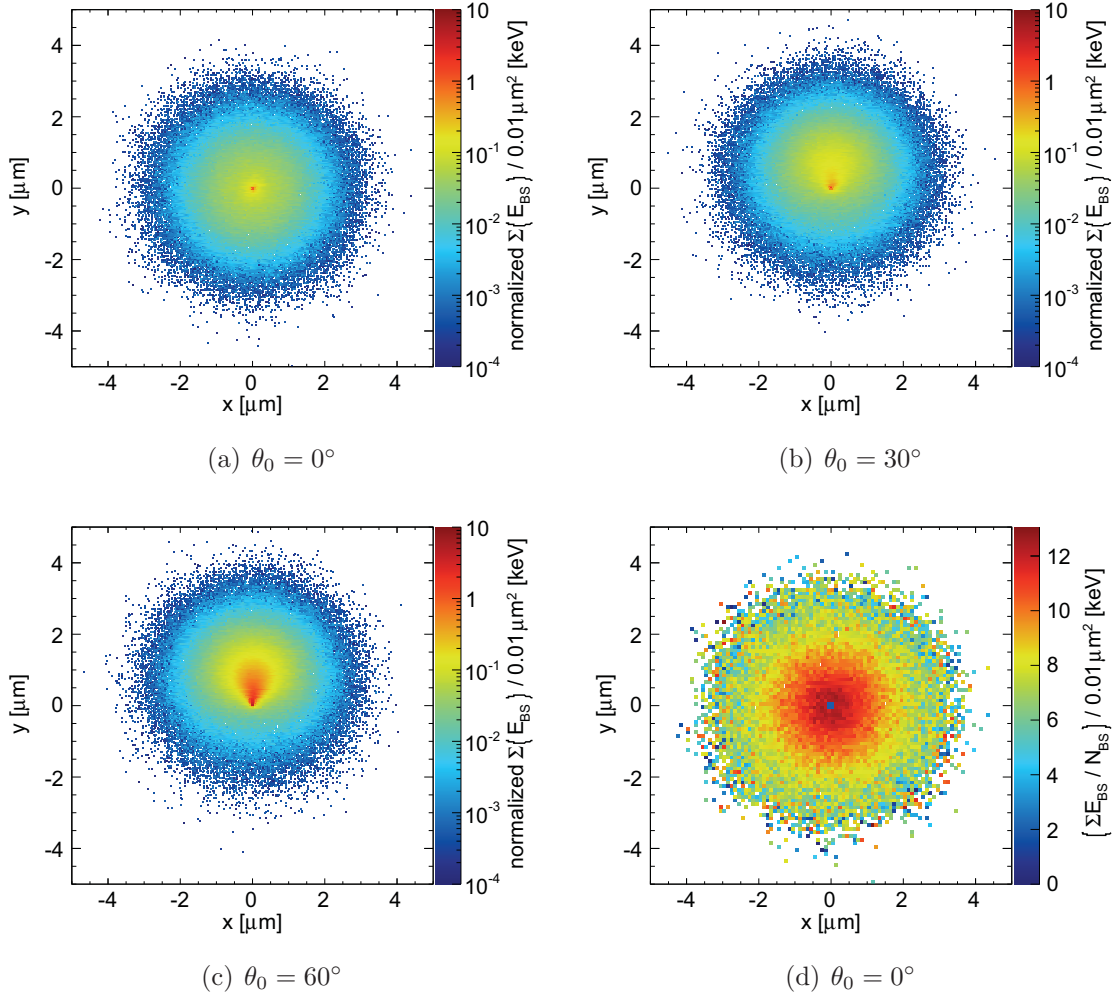


**Figure 5.9:** The spatial distribution of the total backscattered energy  $\Sigma E_{BS}$  at the detector surface for a mono-energetic electron beam with energy  $E_I = 18$  keV, azimuthal incident angle  $\phi_I = 0^\circ$ , point of incidence  $x = y = 0$  and (a) a polar incidence angle  $\theta_I = 0^\circ$ , (b)  $\theta_I = 30^\circ$  and (c)  $\theta_I = 60^\circ$ . (a)-(c) were normalized to the number of incident electrons  $N_I$  resulting in the energy density per area. (d) The ratio of  $\Sigma E_{BS}$  to the number of backscattered electrons  $N_{BS}$ , resulting in the average backscattered energy. Backscattered electrons exit the detector up to  $3 \mu\text{m}$  away from the point of incidence with  $E_{BS} > 12$  keV. The comparison of (a) and (d) at the point of incidence shows that here a large number of low-energy electrons (mainly secondary electrons) are backscattered.

to the contribution of primary electrons (see Figure 5.9(d)). It then slowly decreases towards the edge of the distribution. At the outer edge, the number of backscattered electrons  $N_{\text{BS}}$  decreases and single electrons gain a large influence on the average backscattered energy. Electrons with  $E_{\text{BS}} > 12 \text{ keV}$  are observed here, which proves that they are primary electrons. Primary electrons are able to travel up to  $3 \mu\text{m}$  in  $x$ - $y$ -direction before they are emitted from the silicon solid. And, more importantly, they still have a large part of their incident energy.

At the surface of the focal plane detector, the point of emittance of a backscattered electron is in a first approximation also the point of re-entry, since electrons are guided magnetically. Electrons can be backscattered and re-enter the detector up to 14 times (Sec. 6.2.2). Therefore, the position of re-entry may move multiples of the generally assumed  $5 \mu\text{m}$ . As described above, this is also true for high-energy electrons. This effect is small compared to a cyclotron radius of  $126 \mu\text{m}$  for electrons with  $E = 18 \text{ keV}$  and  $B = 3.6 \text{ T}$ . However, both effects should be considered when investigating electron impact close to the border of adjacent detector pixels.

## 5.2.4 Angular distribution of backscattered electrons

For the KATRIN experiment, the energy distribution *and* the angular distribution of backscattered electrons is important. The polar angle of backscattered electrons  $\theta_{\text{BS}}$  determines the ratio of the transversal energy  $E_{\perp}$  to the longitudinal energy component  $E_{\parallel}$ . If  $E_{\parallel}$  is greater than the main spectrometer retarding potential  $U_{\text{R}}$ , the electron may be transmitted towards the source region and is lost for the measurement. Electrons can be magnetically reflected at the detector or pinch magnet depending on  $\theta_{\text{BS}}$ . The path along a magnetic field line in one cyclotron gyration and therefore the time difference between sequential detector impacts of the electron is also defined by  $E_{\parallel}$ .

$\theta_{\text{BS}}$  and  $\phi_{\text{BS}}$  are the polar and azimuthal angles of backscattered electrons. The distribution  $\theta_{\text{BS}}$  over  $\phi_{\text{BS}}$  for three different polar angles of incidence  $\theta_{\text{I}}$  is shown in Figures 5.10(a)-5.10(c). For  $\theta_{\text{I}} = 0^{\circ}$ , the distribution of  $\theta_{\text{BS}}$  is uniform over  $\phi_{\text{BS}}$ , but gets more focused for larger  $\theta_{\text{I}}$ . The most probable values (MPV) for  $\theta_{\text{BS}}$  are

$$\begin{aligned}\theta_{\text{MPV}}(\theta_{\text{I}} = 0^{\circ}) &= (137 \pm 0.5)^{\circ} \\ \theta_{\text{MPV}}(\theta_{\text{I}} = 30^{\circ}) &= (135 \pm 0.5)^{\circ} \\ \theta_{\text{MPV}}(\theta_{\text{I}} = 60^{\circ}) &= (124 \pm 0.5)^{\circ}\end{aligned}$$

To investigate the dependence of the backscattered electron energy  $E_{\text{BS}}$  on the polar angle of backscattering  $\theta_{\text{BS}}$ , the energy distributions for small, medium and large  $\theta_{\text{BS}}$  for  $\phi_{\text{I}} = \theta_{\text{I}} = 0^{\circ}$  are shown in Figure 5.10(d). The distributions are normalized to the number of incident electrons. Their integral reflects the distribution of  $\theta_{\text{BS}}$  in Figure 5.10(a). Therefore, the energy distribution for medium  $\theta_{\text{BS}}$  ( $120^{\circ} < \theta_{\text{BS}} < 150^{\circ}$ ) is dominating over the whole energy range. While the spectral shapes of large and

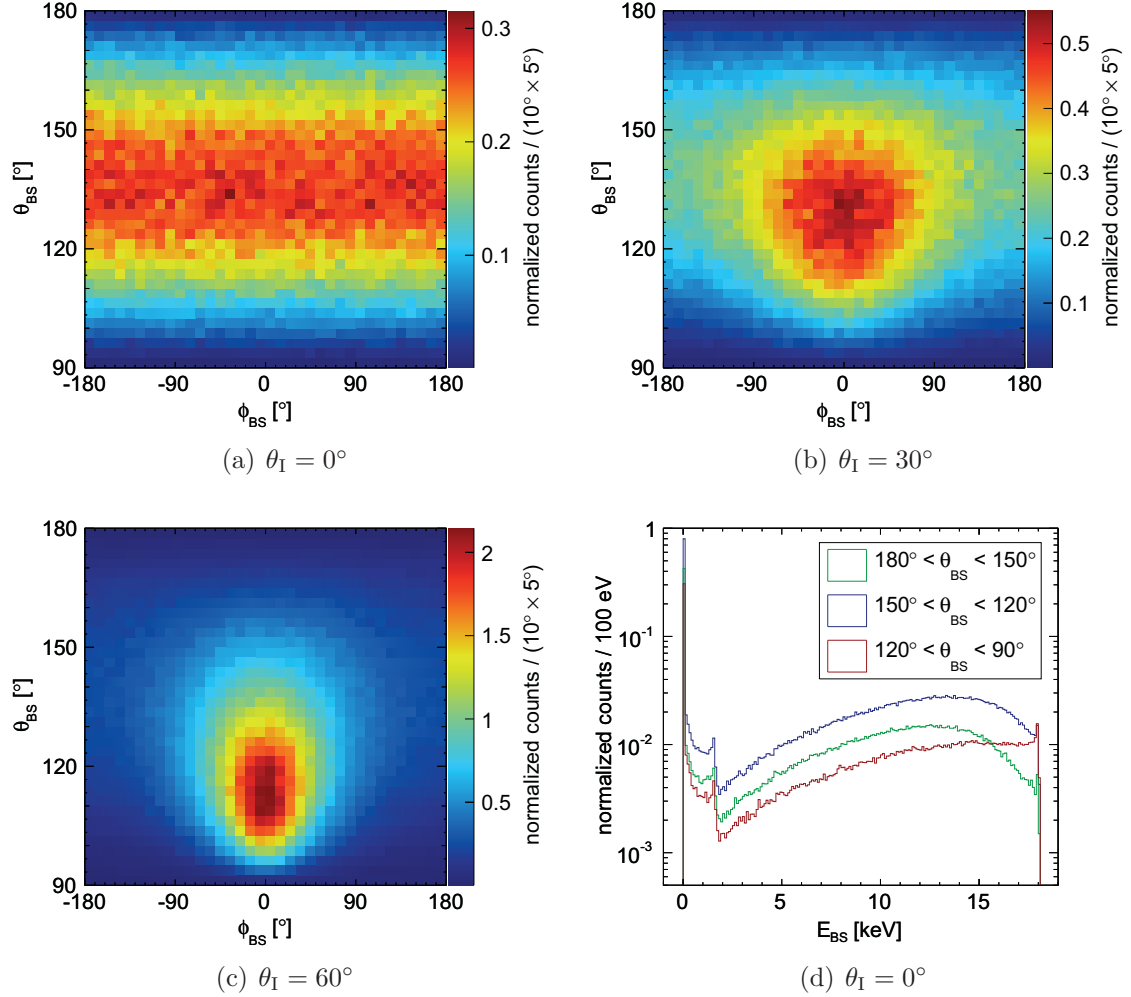


**Figure 5.10: Angular distribution of backscattered electrons** for an electron beam with incident energy  $E_I = 18$  keV, azimuthal incident angle  $\phi_I = 0^\circ$  and polar incident angle (a)+(d)  $\theta_I = 0^\circ$ , (b)  $\theta_I = 30^\circ$  and (c)  $\theta_I = 60^\circ$ . All plots are normalized to the number of incident electrons  $N_I$ . In (a)-(c) the polar angle of backscattered electrons  $\theta_{BS}$  is plotted over the azimuthal angle  $\phi_{BS}$ . (d) The energy spectrum of backscattered electrons with respect to their polar angle  $\theta_{BS}$  for  $\theta_I = 0^\circ$ . It can be concluded from (d) that primary electrons are preferentially scattered into shallow  $\theta_{BS}$ .

medium  $\theta_{\text{BS}}$  agree, a surplus of high-energy electrons is visible for small  $\theta_{\text{BS}}$ . The high energy part of the spectrum with  $E_{\text{BS}} > E_I/2$  is fully characterized by incident primary electrons (Sec.5.1). It can therefore be concluded that the high-energy primary incident electrons are preferentially scattered into shallow polar angles  $\theta_{\text{BS}}$ .

This is important for the KATRIN experiment, since this shallow  $\theta_{\text{BS}}$  translates to low values of  $E_{\parallel}$ . As mentioned before,  $E_{\parallel}$  defines the point of reflection in the KATRIN electromagnetic setup and therefore also defines the travel times between two subsequent detector hits. While the distribution of  $\phi_{\text{BS}}$  is of less importance here, the distribution of  $\theta_{\text{BS}}$  should not be approximated. Both, the detailed description of the polar angle and of the energy of backscattered electrons have to be used for the KATRIN beam line simulations to account for the sensitivity of the electromagnetic design on  $E_{\parallel}$ .

## 5.3 Dead layer effects

A first approach to quantify the influence of the dead layer of silicon detectors is to study it separately. Figure 5.11 shows the energy distribution of mono-energetic electrons with  $E_I = 18$  keV having traveled through a slab of silicon with a thickness  $\lambda_{\text{D}} = 100$  nm. The energy distribution of the mono-energetic beam is broadened towards lower energies after passing the silicon slab.

Primary electrons are found in an interval of the transmitted electron energy  $9 < E_t < 18$  keV, secondary electrons in  $E_t < 8$  keV. This is explained by the low average number of inelastic collisions  $\langle N \rangle = 3.8$  in the slab and the fact that electrons *can* lose a maximum of half their kinetic energy in one collision. For thicker slabs, the distribution of primary electrons would stretch to lower energies. A K-shell Auger electron peak is visible at around 1.8 keV.

The inlay in Figure 5.11 shows the region of the transmitted energy  $E_t$  close to  $E_I$ . Electrons without energy loss, plasmon peaks and the contribution of L-shell ionizations ( $E_t < 17.9$  keV) are visible. This shows that it is crucial to describe the energy loss straggling of electrons in detail to describe thin layers (see also [114, 111, 64, 69]).

### 5.3.1 Dead layer models

Ideally, all energy deposited in a silicon detector creates charge carrier pairs (CC), which are then separated by the electric field. The charges are collected and eventually becomes an entry in a histogram after amplification and analog-to-digital conversion (ADC). The resulting ADC spectrum would show a strong and sharp peak at the electron incident energy  $E_I$  and an almost flat contribution of backscattered electrons only depositing a part of their energy (see  $C(z) = 1$  in Fig. 5.13).

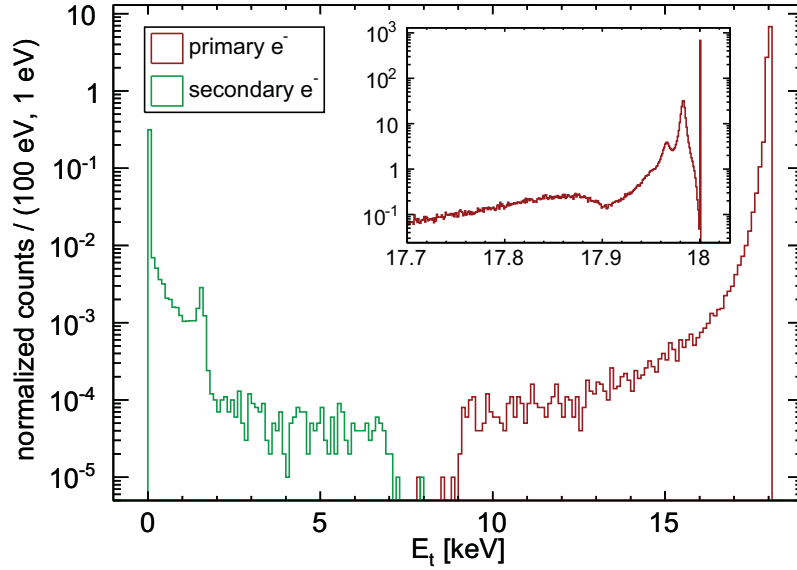


**Figure 5.11:** Energy distribution of an  $E_1 = 18$  keV electron beam after traversing a dead layer with thickness  $\lambda_D = 100$  nm normalized to the number of incident electrons. Primary (PE) and secondary electrons (SE) are shown. A K-shell Auger peak is visible at  $E_t \approx 1.8$  keV. The inlay shows the region close to  $E_1$  in a 1 eV binning. Electrons without energy loss, plasmon peaks and the contribution of L-shell ionizations ( $E_t < 17.9$  keV) are seen.

Depending on the electronic readout performance, the energy deposits would have to be convoluted with the electronic noise contributions. However, the charge collection efficiency  $C(z)$  is not equal to one for every position within the detector, even when neglecting thermal noise contributions or crystal lattice defects.

The opposing surfaces of semiconductor detectors are n-type and p-type doped to create an electric field and thereby deplete the material of free charge carriers. An external field is usually applied to maximize this effect. However, the depletion zone can not be extended to the very end of the solid because of the doping profile and its intrinsic field. Typically, the dopant ions are shallow implanted into the substrates, leading to a finite depth profile. Therefore, free charge carriers remain in the surface area. This layer is usually a few 100 nm and is called the dead layer. Charge carriers created here have a chance to recombine with free intrinsic electrons or holes. Additionally, the electric field is low compared to the full bias voltage which makes separation of charge carriers slow. The dopant does however not introduce additional trapping or recombination centers, because the energy levels are close to allowed energy bands.

The charge collection efficiency  $C(z)$  depending on the depth  $z$  is defined as the ratio of charge reaching the read-out pads to the charge created by the incident particle at  $z$ . While no charge carriers are explicitly created in KESS, it is possible to include  $C(z)$  into the simulation, since the relation between charge carriers created

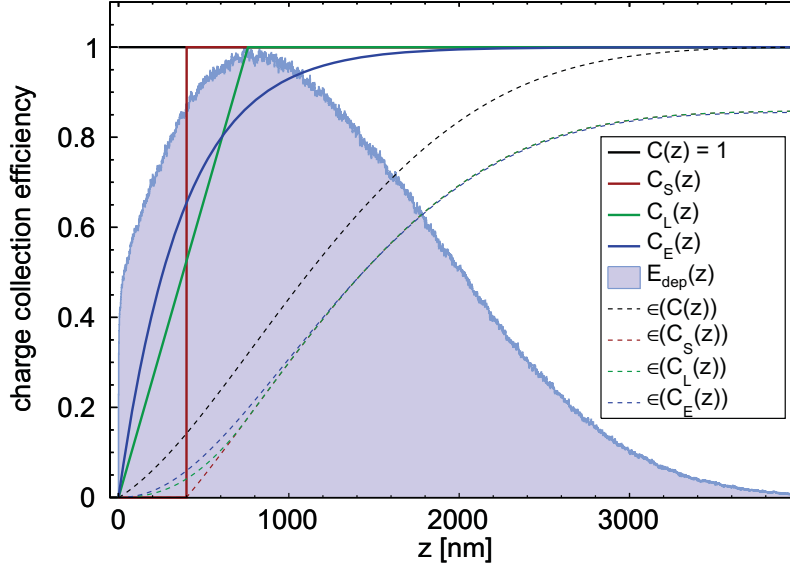


**Figure 5.12: Overview of dead layer models** represented by charge collection efficiencies  $C(z)$  described in the text and plotted over the detector depth  $z$ . The energy deposition  $E_{\text{dep}}(z)$  is normalized to its maximum for incident electrons with  $E_{\text{I}} = 18 \text{ keV}$ . The integrated charge detection efficiencies  $\epsilon(C(z))$  for each  $C(z)$  were determined by integrating  $E_{\text{dep}}(z) \cdot C(z)$  over  $z$ . The depth of partial charge collection is exaggerated to emphasize the arising effects. The parameters used to calculate each  $C(z)$  were chosen to yield the same total charge detection efficiency  $\epsilon_{\text{T}}(C(z))$ .

and energy deposited is linear.

The effect described above can be approximated as a Heaviside step function in  $C_{\text{S}}(z)$  with

$$C_{\text{S}}(z) = \Theta_{\lambda}(z), \quad (5.3)$$

where  $\lambda$  is the step function dead layer thickness  $\lambda_{\text{D}}$ . This approach is widely used in the literature [115, 116, 54].

A second, simple model  $C_{\text{L}}(z)$  can be applied describing a linear increase from 0 to 1 over the depth  $L$ :

$$C_{\text{L}}(z) = \begin{cases} \frac{z}{L} & \text{if } z < L \\ 1 & \text{otherwise} \end{cases} \quad (5.4)$$

More realistically, the charge collection efficiency  $C(z)$  depends on doping strength, implantation depth, the crystal structure and the bias voltage. With detailed calculations, it is possible to derive the charge collection efficiency even for complicated structures. To see the influence of such an exponential dead layer model [117] on the detector response, the charge collection efficiency shown in [118] for a  $\langle 100 \rangle$  silicon crystal with a shallow  $\text{p}^+$  implant is approximated by a charge collection efficiency

$C_E(z)$  following

$$C_E(z) = 1 - e^{-z/\tau}. \quad (5.5)$$

The *relative* charge collection efficiency  $\epsilon(C(z))$  representing the ratio of deposited and collected charge in dependence on  $z$  is given by

$$\epsilon(C(z)) = \int_0^z E_{\text{dep}}(z') \cdot C(z') dz'. \quad (5.6)$$

With  $z$  equal to the detector thickness, Eq. 5.6 yields the *total* charge collection efficiency  $\epsilon_T(C(z))$ .

The charge collection efficiency, the relative charge collection efficiency and the depth profile of the energy deposition  $E_{\text{dep}}(z)$  of electrons with incident energy  $E_I = 18$  keV are shown in Figure 5.12. To emphasize the visible effects, a 400 nm step dead layer was assumed. The parameters for linear and exponential charge collection efficiencies were chosen that  $\epsilon_T(C(z))$  agrees for all  $C(z)$  within a 0.1% uncertainty. This however, does not necessarily indicate the same overall detection efficiency  $\epsilon$  for electrons. The shapes of  $\epsilon(C(z))$  below 1000 nm are significantly different. The deposited energy  $E_{\text{dep}}(z)$  shown is the average of  $10^6$  electrons and does not reflect the structures seen in Figure 5.11. Furthermore,  $\epsilon_T(C(z))$  assumes a region of interest over all deposited energies, while the detection efficiency  $\epsilon$  is usually defined as the ratio between incident electrons and counts in region of interest around the incident energy.

### 5.3.2 Influence on the detector response

To analyze the possible effects of the charge collection efficiency models  $C(z)$  on the detector response and the detection efficiency  $\epsilon$ , the energy spectra obtained for  $E_I = 18$  keV with the  $C(z)$  models described above are calculated. In this case, a step dead layer thickness  $\lambda_D = 100$  nm was used. Again, the parameters used to calculate  $C_E(z)$  were chosen to yield the same total charge detection efficiency  $\epsilon_T(C(z))$ . The linear charge collection efficiency is no longer considered for the following, since it showed similar effects as  $C_E(z)$ .  $C_E(z)$  is considered a more realistic approach.

The high energy part of the energy deposition spectrum is shown in Figure 5.13, since here the dead layer effects are visible. While the spectra obtained assuming a step function dead layer show the structure from single inelastic collisions also visible in Figure 5.11, the structure is not visible for  $C_E(z)$ . The exponential distribution affects a thicker layer and therefore the number of inelastic collisions is larger. Together with the folding of this more complex dead layer model, the structures smear out. The assumption of no dead layer does only show the partial energy deposition by backscattered electrons or secondary electrons escaping the silicon wafer.

Again, the efficiency  $\epsilon$  is defined as the ratio between the counts in an energy region of interest (ROI) from  $15 < E_{\text{dep}} < 21$  and the number of incident electrons. The

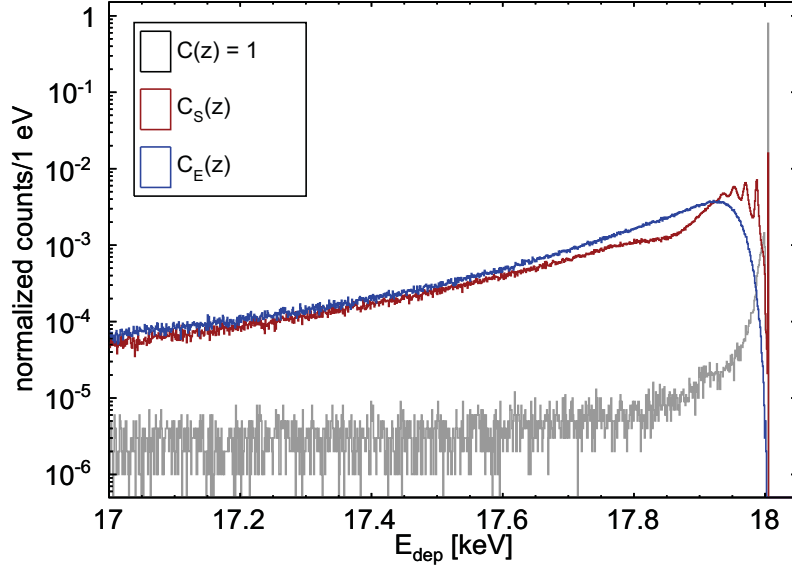


**Figure 5.13:** Energy spectra obtained from different dead layer models represented by the charge collection efficiencies  $C(z)$  for electrons with  $E_I = 18$  keV. A step dead layer of 100 nm was used for  $C_S(z)$ . The parameters used to calculate the exponential charge collection efficiency  $C_E(z)$  were chosen to yield the same total charge detection efficiency  $\epsilon_T(C(z))$ .

results for  $\epsilon$  with incident energy  $E_I = 18$  keV and the different dead layer models are

$$\begin{aligned}\epsilon &= 0.8208 \pm 0.0009 && \text{for } C(z) = 1 \\ \epsilon &= 0.8040 \pm 0.0009 && \text{for } C_S(z) \\ \epsilon &= 0.8088 \pm 0.0009 && \text{for } C_E(z).\end{aligned}$$

The inclusion of a 100 nm dead layer in the simulation results in an absolute 2% decrease in efficiency. This difference increases drastically with decreasing incident energy.

The detection efficiency for the charge collection efficiencies  $C_E(z)$  and  $C_S(z)$  only differs on a per mille level. However, this agreement is not independent from the electron incident energy  $E_I$  and the width of the energy region of interest. The dead layer is a physical property and does not change with  $E_I$ . It is clear from the depth profile of the energy deposition (Fig. 5.13) that a step function and an exponential dead layer will not yield the same detection efficiency for all  $E_I$ . For  $E_I = 10$  keV, the absolute difference is just below 1%, but increases to 5% at 5 keV.

The dead layers of silicon detectors lead to an effective broadening of the incident electron peak. Additionally, when applying an energy resolution, the peak is shifted towards lower energies by the low-energy tail caused by the energy deposits in the dead layer. Therefore, only energy resolutions measured with gamma lines should

be folded with the energy deposition spectra of **KESS** simulations for electrons.

In conclusion, dead layer effects *have* to be included for detection efficiency calculations and especially for simulations of the shape of the detector response. Dead layer effects get more important as  $E_I$  drops. The step dead layer is a valid approximation, as long as sophisticated calculations or measurements of the charge collection efficiency are not available. Especially for measurements with varying incident energies, detailed calculations for the detector used are encouraged. For the focal plane detector in the KATRIN experiment, the interval of incident energies  $18.4 < E_I < 18.6$  keV is small. Thus, the choice of the dead layer model does not introduce systematic uncertainties on the total detection efficiency above a per mille level.

### 5.3.3 Comparison to continuous-slowing-down-approximation dead layers

The continuous-slowing-down-approximation (CSDA, Sec. 4.1.3) is often used by manufacturers and in the literature [115, 116, 54] to determine the step function dead layer thickness of semiconductor detectors. In the measurement, the detector response to electrons with different incident energies  $E_I$  is recorded and the mean energy  $E_m$  of the measured peak is obtained through fitting procedures. The shift of the peak mean to lower energies is then used as  $dE = E_I - E_m$  in Eq. 4.5. The dead layer thickness  $dx = \lambda_{\text{CSDA}}$  is then obtained with a theoretical or experimental stopping power  $S(E) = -dE/dx$ . Usually, this analysis is repeated for different  $E_I$ .

Independent from the choice of the stopping power, the continuous-slowing-down-approximation can not give accurate dead layer thicknesses. The energy loss in a single collision can be up to  $E_I/2$  with a most probable energy loss of  $\sim 17$  eV. With an average number of 3.8 inelastic collisions for electrons with  $E_I = 18$  keV in a 100 nm step function dead layer, the total energy loss is *always* completely random [60]. The simulated, broad energy distribution after a 100 nm silicon layer is shown in Figures 5.11 and 4.2. With the continuous-slowing-down-approximation, all primary electrons have a discrete energy and suffered the same energy loss (Fig. 4.2).

Since  $S(E)$  only depends on the incident energy  $E_I$ , the continuous-slowing-down-approximation yields a linear relation of the total energy loss to the dead layer thickness. This strongly contradicts the distribution of deposited energy over the detector depth  $z$  shown in Figure 5.12.

To determine a single value  $dE = E_I - E_m$ , the finite energy resolution of a detector systems is exploited. This introduces more uncertainties, since the peak shift then is a combination of dead layer and backscattering effects (Fig. 4.1 and Fig. 5.13). The influence of each effect then depends on the energy resolution. The influence of backscattering increases with an increasing energy resolution.

Dead layer thicknesses  $\lambda_D$  obtained with **KESS** are compared to dead layer thicknesses

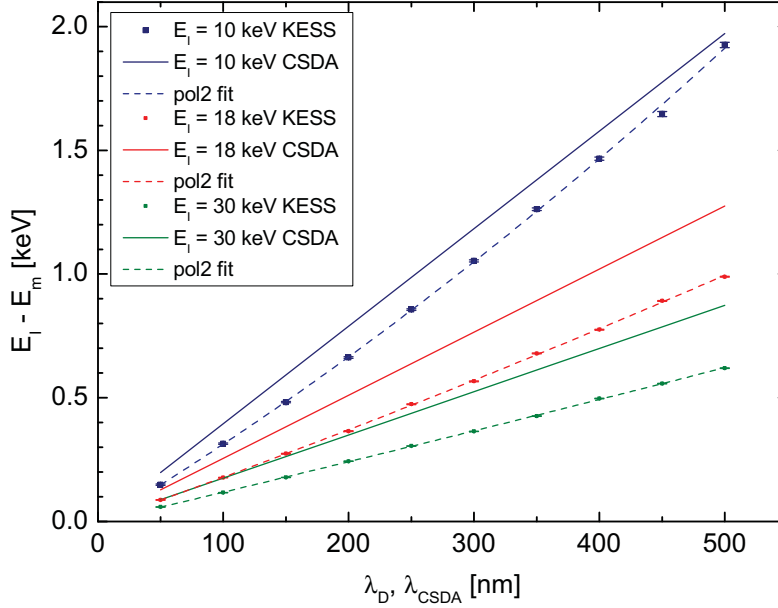


**Figure 5.14: Comparison of KESS and continuous-slowing-down-approximation (CSDA) dead layers.** Spectra of the energy deposit of electrons with incident energy  $E_I$  and dead layer thickness  $\lambda_D$  were simulated with KESS. The difference of incident energy and the peak mean  $E_I - E_m$  is used to calculate the corresponding dead layer thickness  $\lambda_{\text{CSDA}}$  obtained with the continuous-slowing-down-approximation. The KESS result were fitted with a second order polynomial function. The fit parameters are shown in Tab. 5.1

$\lambda_{\text{CSDA}}$  obtained with the continuous-slowing-down-approximation in Figure 5.14. The peak shift  $E_I - E_m$  is plotted over the corresponding dead layer thickness. To obtain this plot, spectra of the energy deposition in the sensitive detector volume were simulated for different  $E_I$  and  $\lambda_D$ . The spectra were folded with an energy resolution of  $\Delta E_{\text{FWHM}} = 1.5 \text{ keV}$  and the peak mean  $E_m$  was obtained by Gaussian fits. As described above,  $dE = E_I - E_m$  was used to calculate the corresponding  $\lambda_{\text{CSDA}}$ . Stopping powers derived from the Bethe formula were used (Eq. 6.3, [58]).

Results obtained with KESS were fitted with a second order polynomial function (Fig. 5.14 and Tab. 5.1). The non-linear relation between  $\lambda_D$  and the energy deposited in the dead layer is clearly visible for low  $E_I$ . For larger incident energies, the distribution is stretched and the relation is almost linear for  $E_I = 30 \text{ keV}$  and  $\lambda_{\text{CSDA}} < 500 \text{ nm}$ . For thicker  $\lambda_{\text{CSDA}}$ , the same behavior as for  $E_I = 10 \text{ keV}$  is observed since it is caused by the average energy deposition along  $z$ .

The difference of  $\lambda_D$  and  $\lambda_{\text{CSDA}}$  increases for increasing  $E_I$ . This is understandable, since the average number of inelastic collisions in the dead layer is decreasing with increasing  $E_I$ . Again, the most probable energy loss in a single inelastic collision is only  $\sim 17 \text{ eV}$  and does not depend strongly on  $E_I$  (Fig. 4.5(a)).

**Table 5.1: Fit parameters for the peak shift  $E_I - E_m$  over the dead layer thickness** obtained with KESS from a second order polynomial fit (pol2)  $f(x) = p_0 + p_1x^1 + p_2x^2$  (Fig. 5.14).

$E_I$ [keV]	$p_0$ [keV]	$p_1$ [keV/nm]	$p_2$ [keV/nm <sup>2</sup> ]
10	$(-9.1 \pm 6.3) \times 10^{-3}$	$(306 \pm 7) \times 10^{-5}$	$(16 \pm 1) \times 10^{-7}$
18	$(-5.1 \pm 4.5) \times 10^{-3}$	$(180 \pm 4) \times 10^{-5}$	$(41 \pm 8) \times 10^{-8}$
30	$(-3.1 \pm 2.7) \times 10^{-3}$	$(120 \pm 2) \times 10^{-5}$	$(9 \pm 4) \times 10^{-8}$

From the points raised above, it is concluded that the complete spectral information of the detector response must be used to determine the dead layer thickness of silicon semiconductor detectors (see also [117]). The simulation of the detector response with KESS including dead layer and backscattering effects is shown in Section 6.1.1.

## 6 KESS application for KATRIN

Having validated **KESS** in the previous section, applications for the KATRIN analysis are presented in this chapter. The higher precision of the simulations permits a detailed study of systematic effects on the analysis of the neutrino mass caused by the focal plane detector.

In the first part of this chapter (Sec. 6.1), the detector response of two different detectors is compared to simulations. Data from the focal plane detector commissioning phase is compared to simulations with the dead layer as a free fit parameter. Furthermore, the variation of the ADC-to-energy calibration inside their generally large errors is used to successfully improve the agreement. Good agreement is found for two of the three analyzed detector pixels (Sec. 6.1.1).

As a second example for the detector response, data from the forward beam monitor detector system are used (Sec. 6.1.2). Since this detector will see rates up to  $10^5$  cps, **KESS** was combined with a simulation, which models the signal amplification and the data acquisition to account for pile-up effects [40]. It will be shown that **KESS** can generally be used as an input for DAQ simulations (i.e. the DAQ simulation for the focal plane detector system currently under development) and is also applicable to silicon drift diode technology.

The second part of the chapter (Sec. 6.2) focuses on the interplay of the electromagnetic design in the spectrometer and detector region, and detector related effects. A drop in count rate for electrons with energies much larger than the retarding potential was measured at the pre-spectrometer [3]. This effect can not be understood from the electromagnetic characteristics of an adiabatically transmitting spectrometer. It will be quantitatively shown that this effect is caused by electron backscattering and a non-adiabatic e-gun by the means of a simulation combining electromagnetic tracking and **KESS** in the *Kassiopeia* framework (Sec. 6.2.1).

Another combined simulation focuses on the main spectrometer, the focal plane detector, and again includes full electromagnetic tracking (Sec. 6.2.2). The detector response is analyzed with regard to the transmission characteristics of the main spectrometer, the electron angle, the electron energy, backscattering effects and dead layer effects. From the results of this simulation, contributions on the systematic and statistical errors on  $m_\nu^2$  are derived. It is generally assumed that backscattered electrons which re-enter the detector and thereby create timely separated energy depositions are analyzed as one event by the DAQ. This assumption will be studied by the simulated time distribution of multiple re-entries of electrons at the focal

plane detector.

## 6.1 The detector response of KATRIN detectors

### 6.1.1 Focal plane detector

The focal plane detector system is currently being completed and operated in stand-alone mode at the University of Washington (UW). The full experimental setup is shown in Figure 3.1. While this effort is ongoing, it is possible to use a focal plane detector wafer in a separate test setup. For this, the detector is housed in a vacuum vessel on a movable mount, which makes it possible to target single pixels. The electrons are yielded from a stainless steel surface by the photoelectric effect, accelerated by an electrostatic potential and focused by an einzel lens onto the desired detector pixel [54]. The KATRIN group at the University of Washington recorded energy spectra for incident electron energies  $10 < E_I < 30$  keV for detector wafer No.76042 and several detector pixels. Three randomly chosen pixels were analyzed and compared to simulation. This section shows the analysis for pixel 141 and the results of all three pixels are summarized.

Due to a vacuum failure, a surface contamination on the detector wafer can not be excluded. Therefore, it is interesting to compare the results of the dead layer thickness with measurements of a comparable detector wafer with a 119 nm dead layer [54].

Since the electro magnetic design of the test setup is simple, KESS can be used as a stand-alone simulation tool. From the test setup geometry, a normal incident angle is assumed. Systematic studies with a tilt between electron beam and detector ( $< 5^\circ$ ) or a Gaussian smearing ( $\sigma = 10^\circ$ ) show no significant effect in the analysis (i.e. shifts and broadenings of the detector response). Figure 5.5 suggests only angles higher than  $20^\circ$  could lead to significant effects. Electrons backscattered from the detector surface are not guided back to the detector and can only contribute once through partial energy depositions.

Although manufacturers of detectors state an approximate dead layer thickness, it can vary because of uncertainties during manufacturing, surface contamination or incomplete depletion. Additionally, the dead layer thickness stated is usually dependent on the measurement technique or theoretical models used (Sec. 5.3). Therefore, the dead layer generally has to be treated as a free parameter. Simulations of dead layers from  $100 \leq \lambda_D \leq 400$  nm in 20 nm steps were prepared for all incident energies  $E_I$ . The incident beam energy is taken from the cathode voltage monitoring and is corrected for the positive bias voltage (+120 V) of the detector, which was applied to the surface of the focal plane detector. The incident energies used are: 30.13 keV, 25.12 keV, 20.12 keV, 17.62 keV, 15.12 keV, 12.62 keV and 10.12 keV. The experimental errors on the incident energies have been neglected in the analysis as

they are expected to be well below a  $10^{-3}$  precision.

The experimental data was provided in calibrated format. The ADC-to-energy calibration was performed with a  $^{241}\text{Am}$  gamma source by fitting the 59.5 keV and 26.3 keV peaks from the  $^{237}\text{Np}$  de-excitation with Gaussian functions and performing a linear regression through the means. The energy calibration used is

$$E(\text{in keV}) = (3.13 \pm 0.05) \cdot 10^{-2} \text{ keV/chan.} \cdot \text{ADC} + (0.39 \pm 0.60) \text{ keV} \quad (6.1)$$

where ADC is the ADC channel.

The energy resolution was obtained by fitting a Gaussian distribution to the 59.5 keV  $^{241}\text{Am}$  gamma line for each pixel. The energy resolution was set to  $\Delta E_{\text{FWHM}} = 1.41$  keV. In a further step, the electronic noise contribution can be added as a free fitting parameter as well. Especially, if fluctuations of the energy resolution over time are found.

### Comparison of simulated and experimental data

To determine the dead layer thickness  $\lambda_{\text{D}}$ , the experimental data are compared to simulations of different  $\lambda_{\text{D}}$ . As a goodness-of-fit indicator,  $\chi^2$  has been used:

$$\chi^2 = \sum \frac{(n_i^{\text{exp}} - n_i^{\text{sim}}(\lambda_{\text{D}}))^2}{n_i^{\text{exp}}} \quad (6.2)$$

For comparison, the simulation results were normalized to the number of experimental events in the peak area. The test was performed over these energy bins  $i$ , with  $n_i^{\text{exp}}$  being the experimental counts in bin  $i$  and  $n_i^{\text{sim}}$  being the expectation from simulations. The corresponding number of degrees of freedom is  $95 < \text{NDF} < 190$  and depends on the peak width.

To find the best fit, this  $\chi^2$ -test was applied for every simulated dead layer and incident energy in the aforementioned energy range. The  $\chi^2$ -value was normalized to the degrees of freedom, i.e. the number of energy bins (minus one) in this energy range. Therefore, all  $\chi^2$ -values stated here are reduced  $\chi^2$ -values. The best  $\lambda_{\text{D}}$  was obtained by determining the minimum of a second order polynomial fit of  $\chi^2$  over  $\lambda_{\text{D}}$ . In Figure 6.2 the two simulations for  $\lambda_{\text{D}}$  closest to the best fit value are shown for two incident energies.

In Figure 6.1(a) the best-fit values for  $\lambda_{\text{D}}$  over the incident energy are shown. The statistical errors for the KESS results are determined from finding the best-fit  $\lambda_{\text{D}}$  with the lowest  $\chi_{\text{min}}^2$ . The statistical margin of error  $\lambda_{\text{D,min,max}}$  is defined by  $\chi^2(\lambda_{\text{D,min,max}}) = \chi_{\text{min}}^2 + 1$ .

Already at this point a contradiction of the extracted dead layers occurs which can not be explained by statistical uncertainties of the measurement. As mentioned above, a constant dead layer value independent of the incident electron energy is

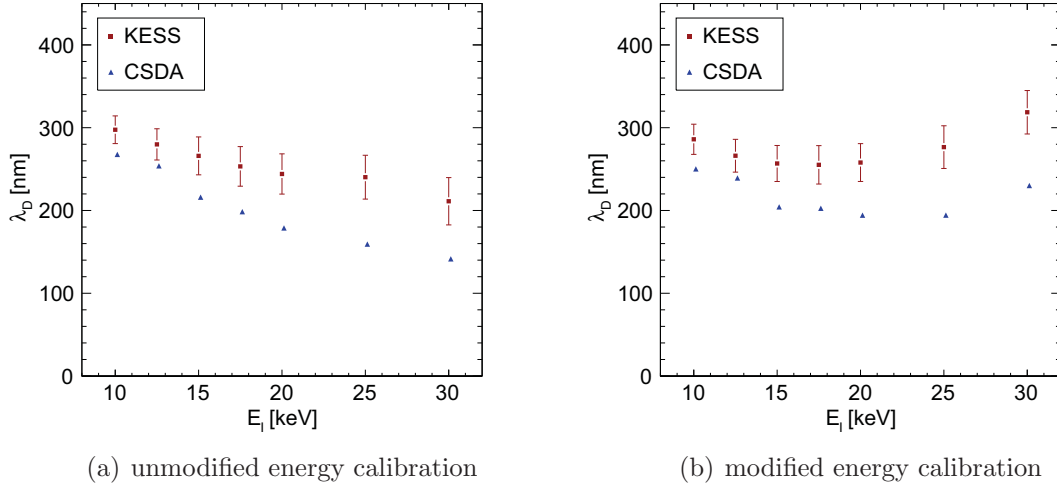


**Figure 6.1: Best-fit dead layer values for pixel 140.** Plotted are the KESS dead layer thicknesses  $\lambda_D$  with lowest  $\chi^2$  over the incident energy  $E_I$ . The error shown is the uncertainty of the  $\chi^2$ -fit. Results obtained with the continuous-slowing-down-approximation (CSDA) are shown for comparison. **(a)** No changes to the central values of the energy calibration were applied. **(b)** The energy calibration offset was changed by  $\delta = -0.19$  keV and the slope by  $\gamma = 0.41 \times 10^{-3}$  keV/channel.

expected. A clear trend of decreasing dead layer thickness with increasing energy is visible.

Calculations using the continuous-slowing-down-approximation (CSDA, Sec. 4.1.3 and Sec. 5.3.3) are shown for comparison in Figure 6.1(a). The dead layer thickness  $\lambda_{\text{CSDA}}$  is derived by

$$\lambda_{\text{CSDA}} = \frac{E_I - E_m}{dE/dx} \quad (6.3)$$

where  $E_m$  is the mean of the measured experimental peak. The mean was found by applying a Gaussian fit at the peak region. The energy dependent stopping powers  $S(E) = -dE/dx$  are derived with the Bethe formula and are taken from the ESTAR database [58].

For dead layers obtained with the continuous-slowing-down-approximation, the trend is even more pronounced (Sec. 5.3.3). The determined dead layers are not compatible to earlier measurements with the pre-spectrometer segmented PIN diode [54], which has undergone the same manufacturing process as the focal plane detector wafer. The earlier measurements resulted in  $\lambda_{\text{CSDA}} = 119$  nm and were performed in the same test setup [54]. Since results from KESS and the continuous-slowing-down-approximation show the same trend, a likely reason is the uncertainty of the experimental energy calibration.

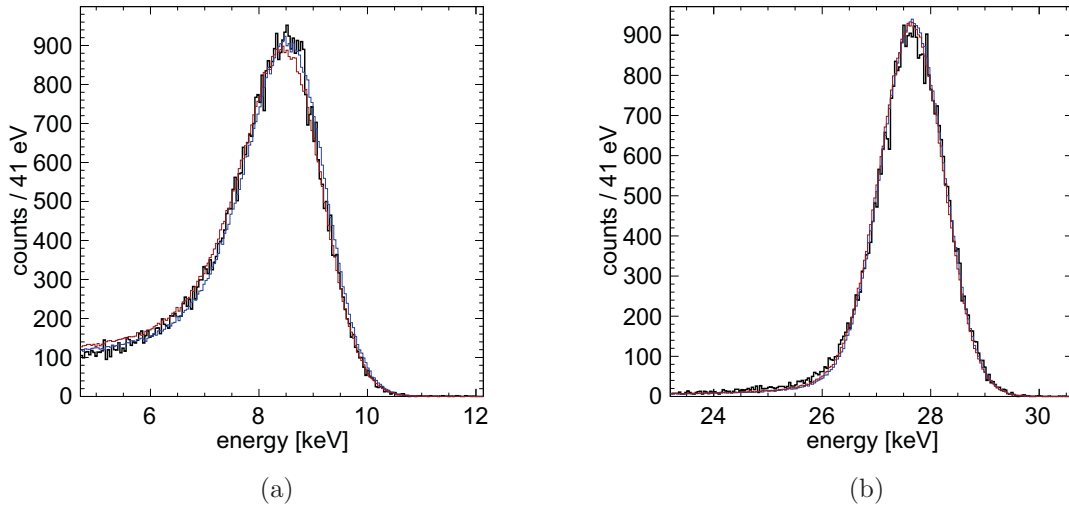


**Figure 6.2: Comparison of KESS simulations to focal plane detector data for pixel 140.** Measurement data (black) is compared to the two simulations with lowest  $\chi^2$ . No modifications to the central values of the calibration were applied. **(a)** incident energy  $E_I = 10.12$  keV (blue) dead layer thickness  $\lambda_D = 280$  nm,  $\chi^2 = 2.39$ , (red)  $\lambda_D = 300$  nm,  $\chi^2 = 1.5$ , and **(b)**  $E_I = 30.13$  keV (blue)  $\lambda_D = 200$  nm,  $\chi^2 = 2.18$  (red)  $\lambda_D = 220$  nm,  $\chi^2 = 2.1$

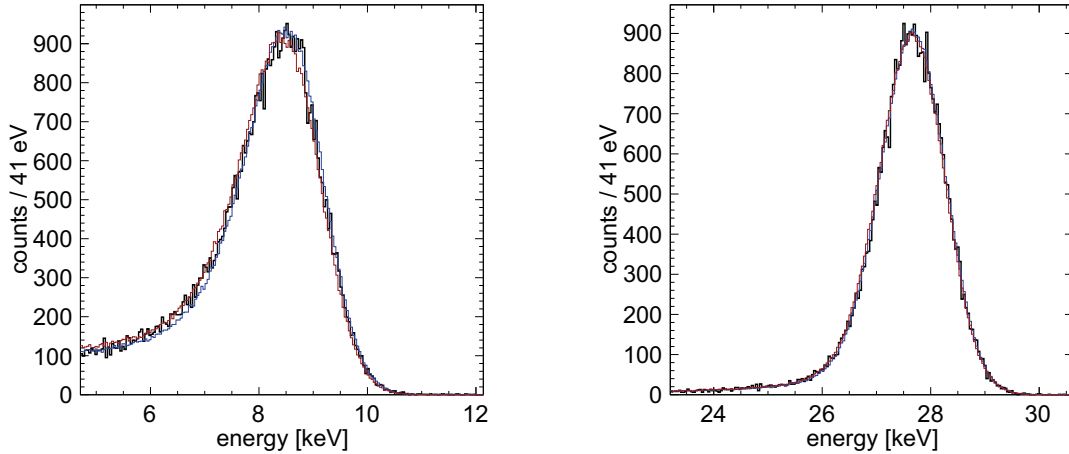


**Figure 6.3: Comparison of KESS simulations to focal plane detector data for pixel 140 with a modified energy calibration.** Measurement data (black) is compared to the two simulations with lowest  $\chi^2$ . The energy calibration offset was changed by  $\delta = -0.19$  keV and the slope by  $\gamma = 0.41 \times 10^{-3}$  keV/channel. **(a)** incident energy  $E_I = 10.12$  keV (blue) dead layer thickness  $\lambda_D = 260$  nm,  $\chi^2 = 1.78$  (red)  $\lambda_D = 280$  nm,  $\chi^2 = 1.77$  and **(b)**  $E_I = 30.13$  keV (blue)  $\lambda_D = 280$  nm,  $\chi^2 = 1.25$  (red)  $\lambda_D = 300$  nm,  $\chi^2 = 1.52$ .

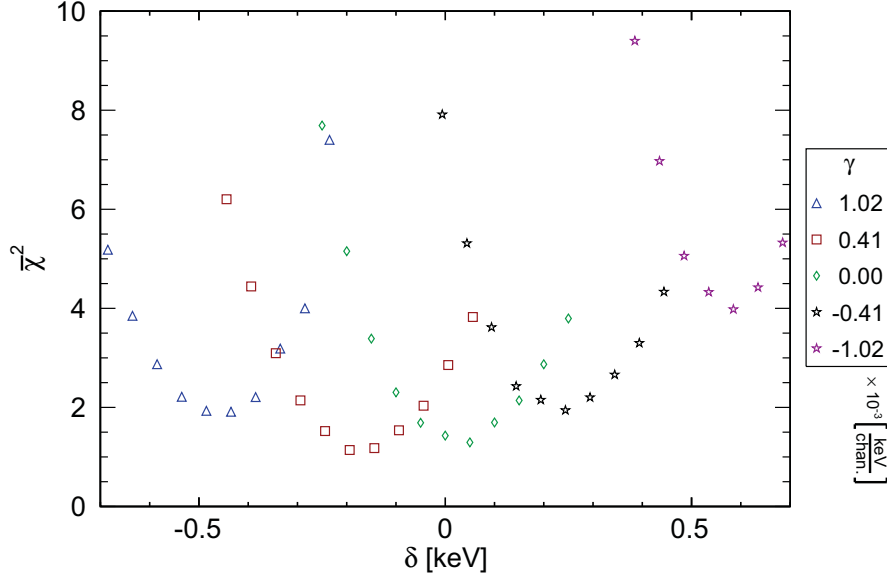


**Figure 6.4:** Averaged  $\bar{\chi}^2$ -values in dependence on the offset variation  $\delta$  and the slope variation  $\gamma$  of the energy calibration of the focal plane detector. The units for  $\gamma$  are  $\gamma \times 10^{-3}$  [keV/channel].

### Influence of ADC-to-energy calibration errors

To take the uncertainty of the energy calibration from Eq. 6.1 into account, the slope of the linear regression  $p_1$  and the offset  $p_0$  were both varied. The slope was varied in the range  $\gamma = p_1 \pm 1.02 \times 10^{-3}$  keV/channel and the offset was varied up to  $\delta = p_0 \pm 700$  eV. This rather large change is reflecting the uncertainty of this fit parameter. We define an energy-averaged  $\bar{\chi}^2$  for the goodness of fits

$$\bar{\chi}^2(\lambda_D) = \sum_i \chi_i^2(\lambda_D) \quad (6.4)$$

with  $\chi_i^2$  being the reduced  $\chi^2$ -value for each incident energy  $E_I$ .

Selected averaged  $\bar{\chi}^2$ -values are shown in dependence on the energy shift  $\delta$  and slope shift  $\gamma$  in Figure 6.4. It is evident that the  $\bar{\chi}^2$ -values depend strongly on the parameters  $\delta$  and  $\gamma$ . A finer grid of  $\delta$  and  $\gamma$  was used to find the lowest  $\bar{\chi}^2$ -value. It is obtained for a change of the energy calibration with  $\delta = -0.19$  keV and  $\gamma = 0.41 \times 10^{-3}$  keV/channel.

For this modified energy calibration, the dead layer thicknesses  $\lambda_D$  with the lowest value of  $\chi^2$  are shown in Figure 6.1(b). For comparison dead layer thicknesses obtained with the continuous-slown-down-approximation  $\lambda_{\text{CSDA}}$  are shown for this modified energy calibration. Considering the errors, the dead layer can be regarded as nearly independent of  $E_I$ . The average dead layers determined and the lowest  $\chi^2$ -values obtained for all analyzed pixels are listed in Table 6.1. In Figure 6.3 the two simulations for  $\lambda_D$  closest to the best fit value are shown for two incident energies.

**Table 6.1: Summary of the comparison of KESS simulations to the detector response of the focal plane detector.** The lowest obtained  $\chi^2$ -values in the comparison of KESS to data are stated for each incidence energy  $E_I$  and detector pixel. The number of degrees of freedom ranges from 95 to 190 and depends on the peak width.  $\chi^2$ -values printed slanted have a  $p$ -value  $p > 0.05$ .  $\bar{\chi}^2$  is the average over all  $E_I$  for each pixel. The errors on  $\bar{\chi}^2$  and the average  $\bar{p}$ -value are the standard deviation from the arithmetic mean. The best-fit dead layers averaged over all  $E_I$  and obtained with KESS  $\lambda_D$  and the continuous-slowing-down-approximation (CSDA)  $\lambda_{\text{CSDA}}$  are given. All values are for a modified energy calibration.

pixel	140	52	61
$\chi^2$ for $E_I = 10.12$ keV	1.03	1.13	1.20
$\chi^2$ for $E_I = 12.62$ keV	1.15	2.30	1.20
$\chi^2$ for $E_I = 15.12$ keV	1.16	2.01	1.12
$\chi^2$ for $E_I = 17.62$ keV	1.03	1.83	1.09
$\chi^2$ for $E_I = 20.12$ keV	1.41	1.59	1.12
$\chi^2$ for $E_I = 25.12$ keV	0.95	1.51	1.21
$\chi^2$ for $E_I = 30.13$ keV	1.23	1.80	1.12
average $\bar{\chi}^2$	1.14 $\pm$ 0.15	1.74 $\pm$ 0.40	1.15 $\pm$ 0.05
average $p$ -value	0.24 $\pm$ 0.24	0.02 $\pm$ 0.05	0.11 $\pm$ 0.7
$\lambda_{\text{CSDA}}$ [nm]	204 $\pm$ 9	275 $\pm$ 11	216 $\pm$ 9
$\lambda_D$ [nm]	<b>260 <math>\pm</math> 8</b>	<b>329 <math>\pm</math> 8</b>	<b>272 <math>\pm</math> 8</b>

## Conclusion

Even with a modification of the central values of the energy calibration within their  $2\sigma$  uncertainty, the obtained dead layer thicknesses (Tab. 6.1) are not compatible with earlier measurements of the pre-spectrometer segmented PIN diode ( $\lambda_{\text{CSDA}} = 119$  nm). This detector was manufactured with the same wafer processing parameters as the focal plane detector wafer and should therefore show the same properties. This supports the hypothesis of surface contamination due to a vacuum incident. A likely reason for this discrepancy was a sudden air leak of the test chamber which lead to a vacuum breakdown [119]. Because the detector is cooled to  $-60^\circ\text{C}$ , water and other molecules have a high probability to stick to the detector surface and thereby enlarge dead layer effects. Further measurements including other detector wafers are being carried out at the University of Washington.

In conclusion, agreement between KESS simulations of the detector response and focal plane detector commissioning data was found, if the parameters of the ADC-to-energy calibration were allowed to vary within their  $2\sigma$  uncertainty. The dead layer values and energy spectra for pixel 52 and 61 are shown in Sec. A.2. The ob-

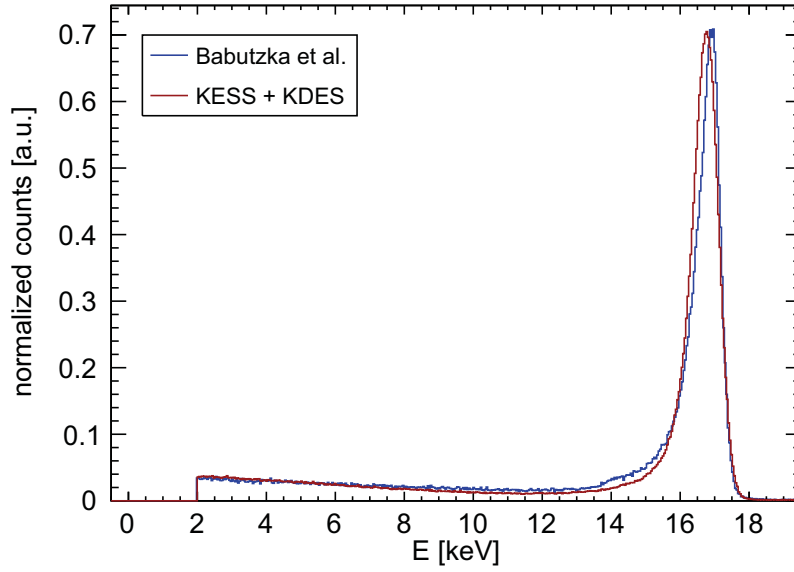
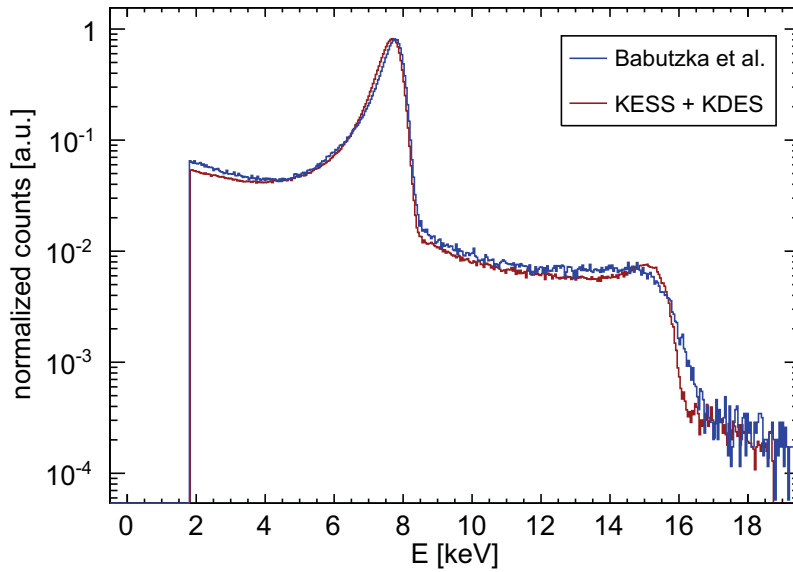
tained reduced  $\chi^2$ -values are given in Table 6.1 for three detector pixels. For pixel no. 52, the agreement is worse for all incident energies. The reasons are unclear at the moment, but are most likely caused by experimental issues. The error on the offset of the energy calibration allows to effectively shift the complete recorded energy spectra. The error on the slope stretches or compresses the energy spectra and thereby effectively changes its shape. Therefore, low uncertainties on these parameters and especially on the slope are preferable. While the focus of this study lies on the simulation of the detector response, this analysis can also be used to determine step dead layer thicknesses for silicon semiconductor detectors without relying on the continuous-slowning-down-approximation. Note that the detailed calculation of an exponential charge collection efficiency and its use in KESS is suggested from Section 5.3.

### 6.1.2 Forward beam monitor detector

The forward beam monitor detector (FBMD) is used to monitor the tritium source activity. More details about the detector and its purpose are found in Section 3.3. Since this detector will be used to spectroscopically measure the complete  $\beta$ -spectrum, it will see rates up to  $10^5$  cps. Simulating the energy deposition in the sensitive volume only will not describe the observed energy spectra, because additional effects (i.e. pile-up) are introduced by the amplification chain and DAQ.

To show that KESS simulations can be used as an input to DAQ simulations, energy spectra with high incident rate are compared to simulations. The DAQ simulation KDES was written by M. Babutzka and is described in detail in [40]. The following effects are described by the KDES package:

- **Electronic noise:** Various sources of electronic noise contribute to the energy resolution of a detector system. The average energy needed to create a charge carrier pair in silicon is  $\omega = 3.6$  eV. The Fano noise reflects the fluctuation of  $\omega$ . It is an intrinsic material property and cannot be overcome. It therefore defines the minimum achievable energy resolution. Further noise sources from the detector wafer and electronics can be divided in serial and parallel noise contributions to the signal. While these contributions can be measured and are included in the simulation, low-frequency 1/f-noise and random noise sources are neglected.
- **DAQ:** The data acquisition digitalizes the analog signal and analyzes it with a 10 MHz sampling rate. The signal is analyzed by differentiating filters. If a signal above an adjustable threshold is found, a trigger is set and a time interval around the trigger is analyzed. This shaping time  $\tau$  has a direct influence on the energy resolution, since its integrating nature allows noise contributions to cancel out.
- **Pile-up:** At high incident rates, the DAQ is no longer able to resolve single

(a) incident energy  $E_I = 17$  keV, incident rate  $10^4$  cps(b) incident energy  $E_I = 8$  keV, incident rate  $4.5 \times 10^4$  cps

**Figure 6.5: Simulated and experimental detector response of the forward beam monitor detector.** Simulation results are obtained with KESS and KDES, experimental results are obtained with a silicon drift diode [40]. (a) The detector response to electrons with incident energy  $E_I = 17$  keV and an incident rate of  $10^4$  cps. (b) The detector response to electrons with  $E_I = 8$  keV and an incident rate of  $4.5 \times 10^4$  cps. Pile-up effects are visible for  $E > 8$  keV.

electrons. When multiple electrons are depositing energy within a time difference lower than the DAQ signal shaping time, the energy of these electrons will be summed and registered as a single electron. This effect leads to counts with energies higher than the single electron energies. This effect also includes partial energy depositions (e.g. from backscattered electrons).

KDES defines the initial time of the electron from the desired event rate at the detector. The parameters defining the electron are handed to *KESS* which performs the simulation inside the silicon and returns the total energy deposited in the sensitive detector volume. The deposited energy is converted to the number of charge carrier pairs  $N_{CC} = E_{\text{dep}}/3.6\text{ eV}$  and the corresponding voltage signal is calculated. From here, KDES simulates the signal chain with the effects described above. Finally, the events are sorted into ADC bins and the energy calibration is applied. The energy calibration from the experiment is used. Similar to the analysis in Section 6.1.1, a step function dead layer was used and the dead layer thickness  $\lambda_D$  was treated as a free parameter. The best agreement with data was found for  $\lambda_D = 115\text{ nm}$ , which corresponds to a dead layer thickness obtained from the continuous-slowing-down-approximation of  $\lambda_{\text{CSDA}} = 80\text{ nm}$ .

The experimental spectra were taken at the e-gun test stand at the Karlsruhe Institute of Technology (KIT) by M. Babutzka et al. [40]. Electrons are produced by the photoelectric effect from a thin gold layer. They are accelerated by an electrostatic potential to their designated incident energy  $E_I$ . Since the gold layer is back-illuminated by UV-light, the electron beam is magnetically bent and refocused to the detector to prevent a direct line-of-sight for the light. Backscattered electrons do not re-enter the detector. Two options for the detector technology used in the forward beam monitor detector system exist. The experimental data presented here is from the silicon drift diode (Sec. 3.3). For details on the measurement see [40].

The simulated and measured detector response of the silicon drift diode to incident electrons with  $E_I = 17\text{ keV}$  is shown in Figure 6.5(a). The incident rate was  $10^4\text{ cps}$ . Effects arising from pile-up are not visible, because the shaping time is a few  $\mu\text{s}$ . Slight disagreement in the energy range  $14 < E < 17\text{ keV}$  and a  $160\text{ eV}$  shift of the peak mean can be observed. This disagreement arises from the uncertainties of the energy calibration (Sec. 6.1.1). The energy calibration for the the forward beam monitor detector suffers from uncertainties in the same order of magnitude as the focal plane detector. The ADC-to-energy calibration used was

$$E(\text{in eV}) = (42.6 \pm 0.3)\text{eV}/\text{chan.} \cdot \text{ADC} + (390 \pm 190)\text{ eV}. \quad (6.5)$$

It is therefore plausible to obtain better agreement if the energy calibration parameters are allowed to vary inside a  $2\sigma$  interval. Since the method to do so is already described and proved successful (Sec. 6.1.1), this approach is not followed here. However, it has to be emphasized that the effective energy resolution of the forward beam monitor detector system is well described by the KDES package. Together with Section 6.1.1, it was shown that *KESS* can describe the detector response of silicon PIN diodes and silicon drift detectors.

To show the influence of high incident rates on the energy spectra, simulations are compared to experimental spectra with  $E_1 = 8 \text{ keV}$  and an incident rate of  $4.5 \times 10^4 \text{ cps}$ . The spectrum (Fig. 6.5(b)) shows the following effects:

- **$2 < E < 5 \text{ keV}$ :** Backscattered electrons only deposit a part of their energy before leaving the sensitive volume of the detector.
- **$5 < E < 8 \text{ keV}$ :** A low energy tail and a shift of the peak mean below the incident energy is observed. This is an expected effect of the dead layer.
- **$8 < E < 16 \text{ keV}$ :** Events registered here are caused by pile-up effects. In first approximation, the energy deposit of two electrons are analyzed and contributed to one event. The flat continuum is caused by the simultaneous analysis of electrons with partial energy deposition. The expected peak of two electrons with full energy deposition at roughly two times  $E_1$  is only visible in the simulation.
- **$E > 16 \text{ keV}$ :** At least three electrons are registered and assigned to one event.

The overall agreement between simulations and experiment is good. This not only shows that KESS and KDES can reproduce experimental data, it also shows that KESS can be successfully used as the input for detector electronics and DAQ simulations.

## 6.2 The detector response including electromagnetic design

### 6.2.1 Pre-spectrometer transmission at high surplus energies

The KATRIN experiment relies on an adiabatic transmission of  $\beta$ -decay electrons from the source region to the analysis plane of the main spectrometer. Each of the components described in Chapter 2 must fulfill this requirement. Especially in the two spectrometers, with their drop in magnetic field strength by many orders of magnitude, test experiments must confirm this property. A first step in checking the adiabatic transmission is to shoot electrons with constant kinetic energy  $E$  through the pre-spectrometer while varying the negative retarding potential  $U_R$ . With a retarding potential  $U_R > qE$  the electrons will be reflected. For  $U_R \ll qE$ , all electrons are transmitted and reach the detector. This experiment was conducted by M. Prall (Universität Münster). All details concerning the measurement can be found in [3, 120]. However, it is not sufficient to obtain 100% transmission through the pre-spectrometer to verify adiabaticity. The adiabaticity has to be measured later together with the main spectrometer and an electron emitter [30].

The pre-spectrometer will be installed between the transport section and the main spectrometer in the final KATRIN setup. In the test setup described here however, an e-gun and a detector system are attached to the ends of the pre-spectrometer

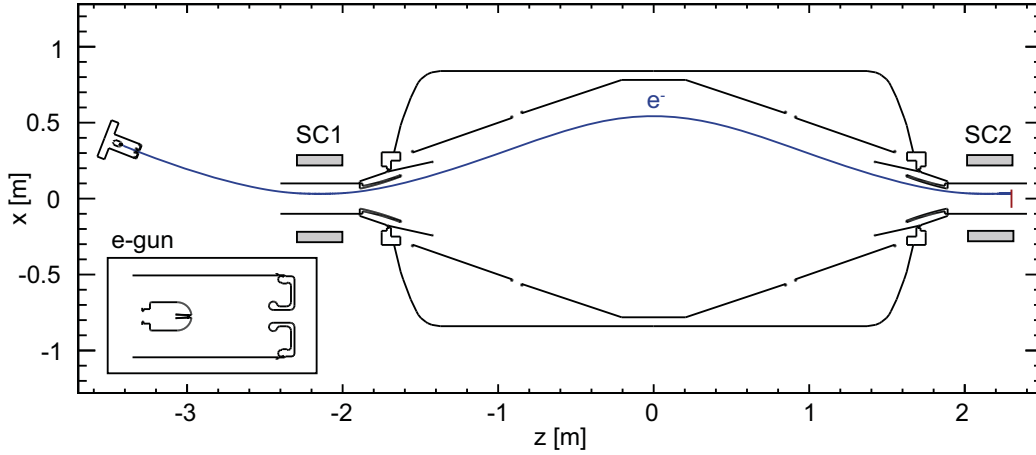


**Figure 6.6: Simulation setup of the pre-spectrometer** with the e-gun, two superconducting coils (SC1,SC2), the pre-spectrometer and the segmented PIN diode (SPD, red). The inlay shows an enlarged view of the e-gun geometry. The e-gun angle towards the  $z$  axis is  $18^\circ$  which corresponds to 72% of the flux tube radius. The segmented PIN diode at  $z = 2.3$  m is not to scale since, in the experiment, it was moved within the  $x$ - $y$  plane to detect the electrons.

(Sec. 3.2 and Fig. 6.6). This permits the measurement of the electromagnetic properties of the pre-spectrometer.

For the measurement [3], the retarding voltage  $U_R$  was varied between -17.5 kV and -0.5 kV in 1 kV steps, while the electron energy was kept constant at  $E = 18$  keV with a precision of  $10^{-4}$ . This measurement was repeated for two different magnetic field strengths ( $B = 4.5$  T and 2.3 T). For each magnetic field, three different e-gun positions corresponding to different areas of the flux tube were used. An e-gun angle of  $\alpha = 0^\circ$  results in an on-axis electron trajectory,  $\alpha = 15^\circ$  corresponds to 45% of the flux tube radius and  $\alpha = 19^\circ$  corresponds to 72% of the flux tube radius. For the recorded energy spectra, a region of interest (ROI) is defined as the energy interval  $15 < E < 21$  keV.

The number of counts in this region of interest for the measurement [3] are shown in Figures 6.7(a) and 6.7(b). For all experimental settings (except  $B = 4.5$  T with an e-gun angle  $\alpha = 0^\circ$ ), a significant drop in count rate for high surplus energies of  $E - qU_R$  can be observed. To understand this effect, backscattering from the detector and a detailed model of the e-gun must be included in the simulations. Note that pure electromagnetic simulations of the pre-spectrometer without e-gun and detector showed adiabatic and 100% transmission for all settings of this experiment [121, 122].

### Backscattering and magnetron drift

Electrons impinging on the detector with an incident energy  $E_I = 18 \text{ keV}$  and an incident angle  $\theta_I = 0^\circ$  have a probability of 20% to be backscattered (Fig. 5.4). Higher incident angles further increase this probability. Most of the backscattered electrons have lost energy in the detector and are again reflected by the spectrometer potential or by the magnetic mirror effect towards the detector. Electrons with only a small total energy loss in the backscattering process have an energy  $E > qU_R$  and can be transmitted towards the e-gun. The electrons enter the e-gun area and are reflected by its electrostatic potential between the e-gun tip and the ground blind. This continues until all energy is finally deposited inside the silicon. Even at high electron surplus energies, the count rate at the detector should be constant. Travel times in the pre-spectrometer are of the order of 10 ns which is far below a  $\mu\text{s}$  shaping time of the DAQ. Therefore, only electrons with large energy losses in the deadlayer will deposit an energy lower than the region of interest in the sensitive volume. This can explain the measurement at  $B = 4.5 \text{ T}$  and  $\alpha = 0^\circ$ , where no loss in count rate is observed.

The description above is also valid for the off-axis e-gun settings with  $\alpha = 15^\circ$  and  $\alpha = 19^\circ$ . But additionally, the full magnetron motion must be considered. On-axis electrons gyrate around the central magnetic field line in a helical cyclotron motion. Since the magnetic field is axially symmetric and the cyclotron radius is changing slowly, the electrons are in a quasi-constant magnetic field. For off-axis electrons however, the magnetic field is asymmetric during a cyclotron motion. This gradient  $\nabla \vec{B}$  results in a radial  $\vec{B} \times \nabla |\vec{B}|$  drift of the guiding center along a plane with constant magnetic field (Fig. 4.11). This axial rotation can cause the electron to eventually hit the electron ground blind depending on  $\nabla \vec{B}$ , the electron energy (i.e. the cyclotron radius) and the total path length. The axial rotation is only dependent on the energy and not on the direction of the speed of the electron. The path for the electrons in the pre-spectrometer is elongated by reflections at the detector, e-gun, magnets and spectrometer potential and can be multiples of the spectrometer length. The higher the surplus energy, the higher the probability for a backscattered electron to overcome the spectrometer potential after energy deposits in the detector. Therefore, the count rate in the region of interest decreases with higher energy. With this, all measurements at  $B = 4.5 \text{ T}$  can be explained.

### Non-adiabatic e-gun and electromagnetic tracking

For  $B = 2.3 \text{ T}$  a loss in count rate is observed for all e-gun settings, including the on-axis one. It is not possible to explain this effect with backscattering and the  $\vec{B} \times \nabla |\vec{B}|$  drift alone.

The electric field gradient in the e-gun is large compared to the pre-spectrometer, since the potential difference of 18 kV is applied across a distance of only a few

cm. Together with the 50% lower magnetic field in the center of the magnets, this can lead to a non-adiabatic transport in the e-gun region [123]. The e-gun itself is located at a magnetic field of  $B \approx 0.018$  T. Thus, a backscattered electron entering the e-gun through the ground blind has a probability to change its angle towards the magnetic field line non-adiabatically. Depending on the new angle and the electron energy, it can be trapped between the e-gun and the closest magnet or the spectrometer potential. Thus, a loss in count rate in the region of interest will also be observed for on-axis measurements. This assumption is therefore able to explain the measurement for  $B = 2.3$  T and  $\alpha = 0^\circ$

## Simulation

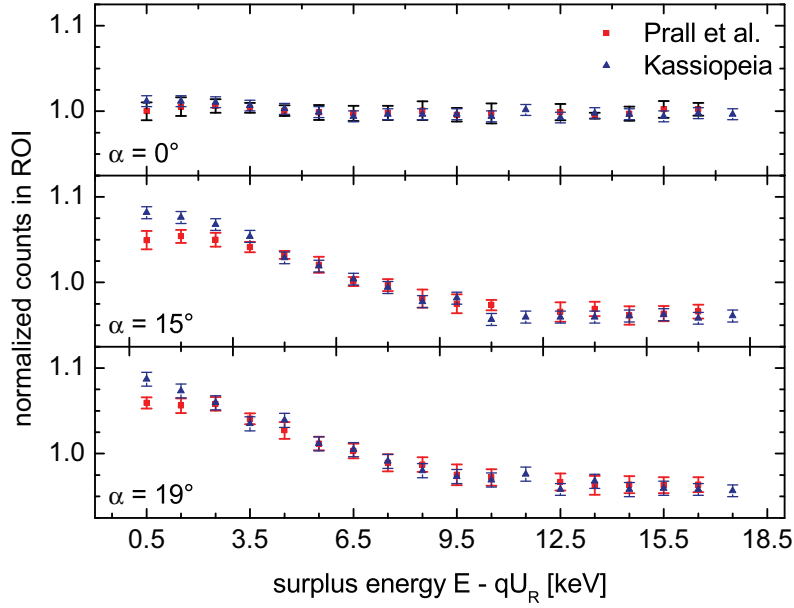
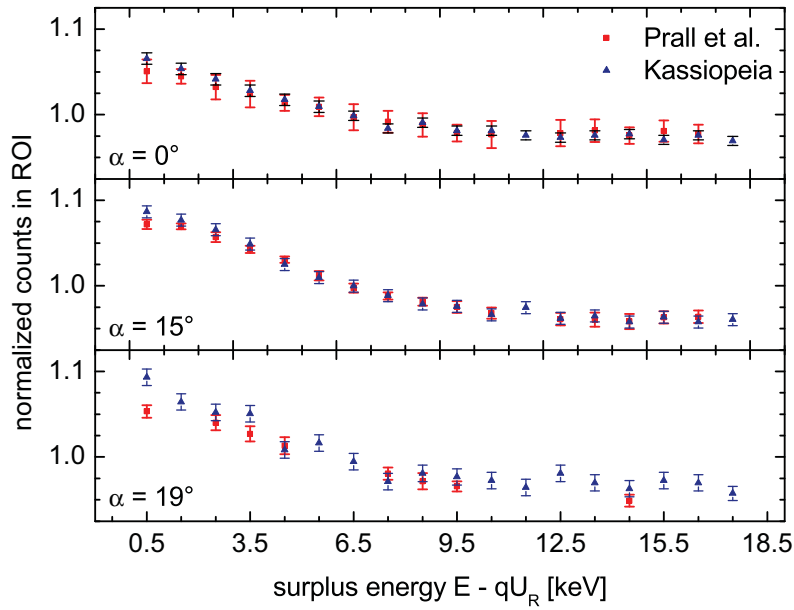
It is difficult to validate the above assumptions analytically. Since it was not clear if these assumptions do explain the observed loss in count rate, a detailed *Kassiopeia* simulation (Sec. 4.6) was set up. The *Kassiopeia* package *KTRACK* was used for electromagnetic tracking and was extended by a detailed and tiltable e-gun model by S. Mertens [124]. *KESS* was responsible for energy loss, detector response and the angular and energy distribution of backscattered electrons.

The electrons were started with a uniform random kinetic energy of  $0 < E < 2$  eV. They were uniformly distributed on a disc with diameter  $d = 1$  mm in front of the actual gold tip. As the angular distribution,  $\theta = \arcsin(R)$  from [51] and  $\phi = 2\pi R$  with a uniformly distributed random number  $R \in [0, 1]$  was used. *KTRACK* was used in the "exact calculation mode" which in contrast to "adiabatic approximation" also allows for non-adiabaticities. However, earlier simulations showed no adiabaticity violations in the pre-spectrometer. This option was chosen to account for non-adiabaticities in the e-gun. The detector with a step-function dead layer of  $\lambda_D = 150$  nm and an energy resolution of  $\Delta E_{\text{FWHM}} = 3.5$  keV was simulated by *KESS*.

As mentioned before, the time an electron travels between two subsequent detector hits is more than two magnitudes smaller than the DAQ shaping time. This means, subsequent hits are analyzed by the DAQ as one hit. Therefore, each energy deposition in the sensitive detector volume per electron was summed up, even for electrons with multiple detector entries. The total deposited energy for each electron was convoluted with the energy resolution. The final detected energy was randomly sampled from a Gaussian distribution with a FWHM of 3.5 keV and with the mean equal to the deposited energy. As in the experimental data analysis, all electrons with energies  $15 < E < 21$  keV were counted.

Possible exit conditions of *KESS* and *KTRACK* were:

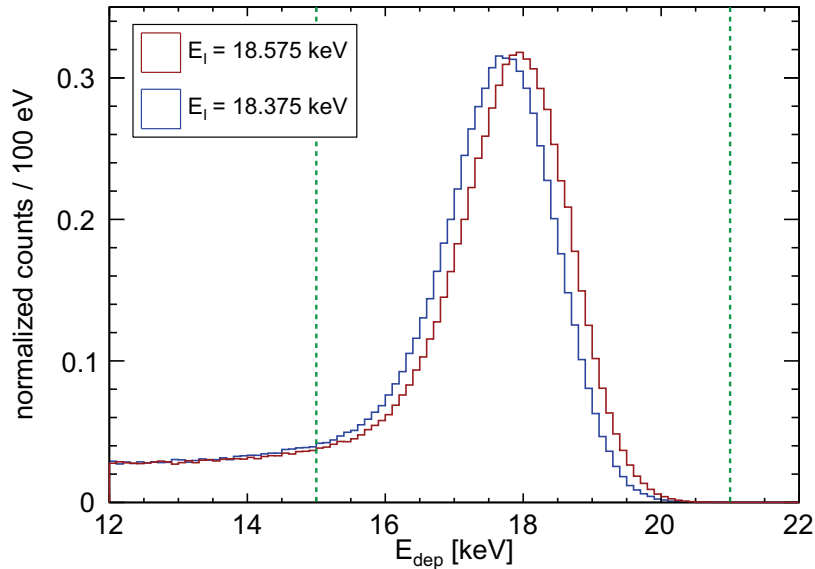
- electron hit e-gun ground blind
- electron energy lower than 100 eV
- electron turned around more than 20 times (trapping)


 (a)  $B = 4.5$  T

 (b)  $B = 2.3$  T

**Figure 6.7: Pre-spectrometer transmission at high surplus energies for (a)  $B = 4.5$  T and (b)  $B = 2.3$  T and various e-gun angles  $\alpha$ .** The experimental data from [3] are compared to Kassiopeia (including KESS) simulations. The statistical uncertainty for the simulation is shown. Experimental errors include statistical and systematic uncertainties [3]. Experimental and simulation results were each normalized that the sum of all counts in the region of interest over all settings of  $U_R$  is equal to one.

## Conclusion

Experimental and simulation results were each normalized that the sum of all counts in the region of interest over all settings of  $U_R$  is equal to one. Figures 6.7(a) and 6.7(b) show the normalized simulation and experimental results. Good agreement for the measurements at  $B = 2.3$  T and  $B = 4.5$  T and all e-gun angles  $\alpha$  is found. Since the pre-spectrometer was designed to transport all electrons adiabatically and the same electromagnetic simulations used here confirmed the adiabaticity, the loss in count rate can be fully accounted by the aforementioned assumptions. All losses in count rate are explained by backscattering from the detector, the  $\vec{B} \times \nabla|\vec{B}|$  drift and a non-adiabatic electron transport inside the e-gun. This example emphasizes the need for detailed simulations of the detector response, backscattering and the electron transport in electromagnetic fields to understand and investigate unexpected effects.



**Figure 6.8: Energy dependent detection efficiency.** The boundaries of the region of interest shown as green dotted lines are calibrated with x-rays, which fully deposit their energy in the sensitive detector volume. Simulated detector response spectra for electron incident with two incident energies  $E_1$  calculated with KESS are shown. Because of the low-energy tail a reduced count rate in the region of interest is measured for the electrons with the lower energy. This leads to an energy dependent detection efficiency  $d\varepsilon/dE$ .

## 6.2.2 Efficiency of the focal plane detector in the final KATRIN setup

In the current picture of systematic error contributions to the neutrino mass measurements, the focal plane detector does not play any role (Sec. 2.4). This is suggested by the fact that the detector efficiency  $\varepsilon$  does not enter directly into the analysis of the neutrino mass. Its true value is hidden in the analysis by unconstraining the fit with regard to the total number of counts. From this point of view, the detection efficiency does not play a role as long as it does not change the spectral distribution of the measured spectrum. This means in particular: the detection efficiency is independent of the kinetic energy ( $\varepsilon \neq f(E)$ ) or any high voltage settings ( $\varepsilon \neq f(U_R)$ ). The efficiency is then even allowed to float over long time scales.

However, the assumption of an energy independent detection efficiency is not correct due to dead layer effects (Fig. 6.8). In practice, one has to define a region of interest (ROI) in which a signal is expected for the energy deposited. Due to backscattering processes and energy losses in the dead layer of the detector, the detector response to a mono-energetic electron will have a low energy tail. It reaches below the energy threshold of the detector system and thus below any lower limit for a region of interest. The detector efficiency then depends on the fraction of energy an electron loses on average in the given region of interest and thus on the incident energy.

In general the detection efficiency for a given region of interest is a function of its value at the center and its boundaries. In addition it depends on the incident electron energies and angles, insensitive detector volumes, the detector resolution and finally the transport mechanism of backscattered electrons. All these effects are included in the `KESS` and `Kassiopeia` simulations.

### Simulation setup

A simulation with `Kassiopeia` including `KESS` was set up which allows the investigation of the influence of the focal plane detector system on the neutrino mass measurement. The setup is geometrically limited to the main spectrometer and the focal plane detector system (Fig. 6.9), but includes all magnets and air coils of the final KATRIN beam line. The simulated detector magnet was set to produce a central magnetic field of  $B_{\text{det}} = 3.6 \text{ T}$ , the magnet between pre- and main spectrometer produces a 4.5 T and the pinch magnet a 6 T center magnetic field, which each corresponds to the design values. Electrons are started in the center of the magnet between pre- and main spectrometer (PMS) and are guided to the detector, if the transmission conditions of Eq. 2.9 are fulfilled.

The following simulation parameters can be varied:

- The electrostatic retarding potential  $U_R$ ,
- the kinetic electron initial energy  $E_{\text{PMS}}$ ,

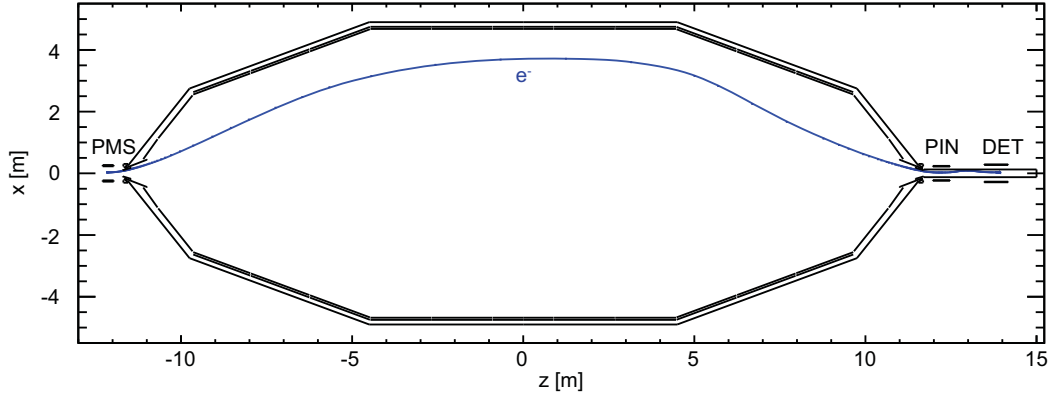


**Figure 6.9: Simulation setup for the mainspectrometer and focal plane detector** with the superconducting magnet between pre- and mainspectrometer (PMS,  $B_{\text{PMS}} = 4.5$  T), the pinch magnet (PIN,  $B_{\text{pin}} = 6$  T) and the detector magnet (DET,  $B_{\text{det}} = 3.6$  T). A retarding potential is applied in the spectrometer with a maximum  $U_{\text{R}}$  near  $z = 0$ . Electrons are started in the center of the PMS magnet with an energy  $E_{\text{PMS}}$  and a polar angle  $\theta_{\text{PMS}}$ . Note that for the first detector incidence of each electron, the incident energy  $E_{\text{I}} = E_{\text{PMS}}$ . The focal plane detector is situated at  $z = 13.94$  m, off-center in the detector magnet. The blue line shows the track of an off-axis electron.

- the initial azimuthal angle  $\phi_{\text{PMS}}$  relative to the  $x$ - $z$ -plane and the initial polar angle  $\theta_{\text{PMS}}$  relative to the  $z$ -axis. Both can be chosen as discrete angles or to have a uniform distribution in a specified interval. The maximum initial polar angle in the center of the magnet between pre- and mainspectrometer transmitted to the focal plane detector is  $\theta_{\text{PMS}} = 60^\circ$  (Eq. 4.2).
- the detector dead layer  $\lambda_{\text{D}}$ ,
- the  $x$ -component of the initial position; the outer edge of the flux tube is  $x_{\text{max}} = 0.036$  m,
- the number of initial electrons  $N_{\text{I}}$ .

Each setting was simulated with  $N_{\text{I}} = 10^6$  electrons. The region of interest was set to  $15 < E < 21$  keV and the statistical errors are determined by the number of counts in the region of interest  $N_{\text{ROI}}$  by  $\sigma_{\text{stat}} = 1/\sqrt{N_{\text{ROI}}}$ . No significant dependence on the  $x$ -position was found. All results shown here were obtained with  $x = 0$ .

For the electromagnetic tracking of the particle (**KTRACK**), the adiabatic approximation was used, since the main spectrometer is designed to transmit fully adiabatic and the retarding potential as well as the initial electron energy are maximally lowered by 200 V (eV) below the assumed tritium  $\beta$ -decay endpoint energy  $E_0 = 18575$  eV. The full magnetron motion including the gyration around the electron guiding center are modeled in detail, so that incident angle and position at the detector are exact (Sec. 4.6). No interactions of the electron with residual gas molecules were taken

into account.

KESS was set up to only consider primary electrons, since only the high energy part of the detector response is of interest (Sec. 5.1). When the combined main spectrometer and focal plane detector commissioning is completed and more experimental information on the systems is available, simulations taking into account secondary electrons must be considered as suggested by Section 5.1.

The energy resolution of the focal plane detector for gamma rays was assumed to be  $\Delta E_{\text{FWHM}} = 1.5 \text{ keV}$ . Other than that, the standard KESS settings described in Table A.1 were used.

### Simulation results concerning statistical uncertainties

As a first step, the dependence of the detection efficiency  $\varepsilon$  on the initial polar angle  $\theta_{\text{PMS}}$  is examined.  $\theta_{\text{PMS}}$  was varied while all other parameters were fixed (Fig. 6.10). The observed effect is an absolute decrease of the efficiency by 5% from  $\varepsilon(0^\circ)$  to  $\varepsilon(60^\circ)$ . This decrease towards higher incident angles is explained by the increasing backscattering probability (Fig. 5.5). Additionally, high incident angles elongate the track length in the dead layer, which increases the effective dead layer thickness. Assuming a uniform distribution of  $\theta_{\text{PMS}}$ , the average efficiency over  $\theta_{\text{PMS}}$  is  $\varepsilon = 0.92$ . This is compatible with the average efficiency of  $\varepsilon = 0.9$  used to calculate the statistical uncertainty on the neutrino mass  $m_\nu^2$ .

Note that the dependence of the detection efficiency  $\varepsilon$  on the initial polar angle  $\theta_{\text{PMS}}$  is of importance, as most calibration measurements at KATRIN are done with electron emitters (i.e. e-gun) with fixed angles of emittance [108, 109]. It is therefore necessary to include  $\varepsilon(\theta_{\text{PMS}})$  in the analysis and when extrapolating to an isotropically emitting source.

To investigate the influence of the dead layer thickness  $\lambda_{\text{D}}$ , the focal plane detector efficiency was simulated for several values of  $\lambda_{\text{D}}$  and two initial polar angles  $\theta_{\text{PMS}} = 0^\circ$  and  $60^\circ$  (Fig. 6.11). For  $\theta_{\text{PMS}} = 0^\circ$  the absolute decrease of  $\varepsilon(\lambda_{\text{D}})$  is 17% and 31% for  $\theta_{\text{PMS}} = 60^\circ$ . In order to reduce the measuring for the KATRIN experiment thin dead layers should be use. Additionally, it should be noted again that the dead layers in KESS are generally larger than the ones quoted by manufacturers or measurements using the continuous-slowing-down-approximation (CSDA, Sec. 5.3.3). A  $\lambda_{\text{CSDA}} = 100 \text{ nm}$  focal plane detector dead layer calculated with the continuous-slowing-down-approximation corresponds to a  $\lambda_{\text{D}} = 142 \text{ nm}$  dead layer in KESS.

To quantify the influence of the dead layer on  $\varepsilon$ , a linear and a second order polynomial fit were applied to the simulation results. From the linear fit, a drop in efficiency of  $\Delta\varepsilon = 7 \times 10^{-3}$  for an increase of  $\Delta\lambda_{\text{D}} = 10 \text{ nm}$  can be derived. The dead layer thickness can slowly increase over time through sticking of residual gas molecules to the cold detector. This has no direct influence on the systematical error on  $m_\nu^2$ , since KATRIN is only sensitive to the shape of the measured spectrum. A

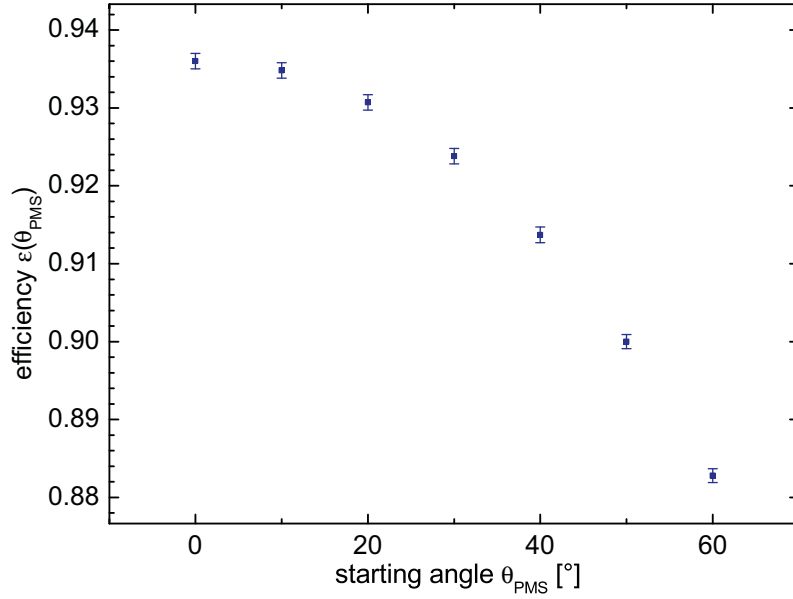


**Figure 6.10:** Simulated focal plane detector efficiency  $\varepsilon(\theta_{\text{PMS}})$  over the initial polar angle  $\theta_{\text{PMS}}$  for a retarding potential  $U_{\text{R}} = -18570$  V, initial energy  $E_{\text{PMS}} = 18575$  eV and a dead layer thickness  $\lambda_{\text{D}} = 100$  nm. The statistical errors are shown. The region of interest is  $15 < E < 21$  keV.

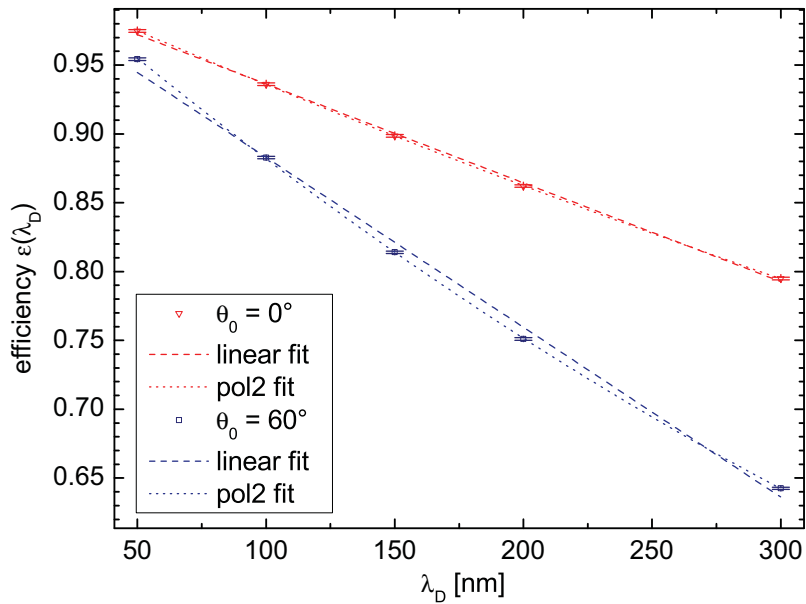


**Figure 6.11:** Simulated focal plane detector efficiency  $\varepsilon(\lambda_{\text{D}})$  over the dead layer thickness  $\lambda_{\text{D}}$  for a retarding potential  $U_{\text{R}} = -18570$  V, initial energy  $E_{\text{PMS}} = 18575$  eV and initial polar angle  $\theta_{\text{PMS}} = 0^\circ$  and  $60^\circ$ . The region of interest is  $15 < E < 21$  keV. The statistical errors are shown.

regular monitoring of the dead layer thickness is advisable to find an optimal compromise between detector re-commissioning and neutrino mass measurement time. A possible systematic effect of an unaccounted for increase in dead layer thickness in combination with an energy dependent detection efficiency is discussed below.

### Simulation results concerning systematic uncertainties

As mentioned before, the focal plane detector efficiency  $\varepsilon$  contributes to the systematic error on  $m_\nu^2$ , if it is not constant over the spectrometer retarding potential  $U_R$  or the electron energy  $E_{\text{PMS}}$ . Figure 6.12 shows the influence of a varying  $U_R$  for a fixed dead layer and incident energy for two initial polar angles  $\theta_{\text{PMS}} = 0^\circ$  and  $60^\circ$ . This simulation is very sensitive to the energy and angle of backscattered electrons due to the retarding potential  $U_R$  again seen by backscattered electrons. If the electron energy and the alignment of its momentum with the magnetic field lines is sufficient, the electron is transmitted through the spectrometer in reverse direction. The electron is transported to the source region and is lost for detection. Obviously, this is only possible for electrons backscattered elastically or with small total energy losses  $\Delta E < E_{\text{PMS}} - qU_R$ .

Therefore, more data points were simulated in the region where  $E_{\text{PMS}} \approx qU_R$ . With higher statistics and a more dense grid of values for  $U_R$ , the structure of the energy spectra of backscattered electrons just below the incident energy shown in Figure 5.7(b) should be visible in  $\varepsilon(U_R)$ . However, no statistical significant slope of the efficiency is observed over the simulated range of  $U_R$  (Fig. 6.12). Since the statistical error is already at the  $10^{-3}$  level, the expected systematic errors on  $m_\nu^2$  are well below the maximum allowed contribution to the systematic error of  $\Delta m_{\text{sys,max}}^2 < 7.5 \times 10^{-3} \text{eV}^2$ .

**Table 6.2: Fit parameters for  $d\varepsilon(E_{\text{PMS}})/dE$  from Fig. 6.13 for a linear fit  $f(x) = p_0 + p_1x$ .**

$\lambda_D$	$p_0 [\times 10^{-2}]$	$p_1 [\times 10^{-5}/\text{eV}]$
100 nm	$39.35 \pm 2.92$	$2.78 \pm 0.16$
150 nm	$12.13 \pm 4.20$	$3.96 \pm 0.23$
200 nm	$-8.05 \pm 3.51$	$4.78 \pm 0.19$
300 nm	$-38.50 \pm 6.54$	$5.94 \pm 0.35$

The dependence of the detection efficiency  $\varepsilon$  on the initial energy  $E_{\text{PMS}}$  is examined in Figure 6.13. Note that the initial energy  $E_{\text{PMS}}$  is equal to the incident energy  $E_I$  at the detector. The results were calculated with a fixed retarding potential  $U_R$  and a uniformly distributed initial polar angle  $\theta_{\text{PMS}}$  between  $0^\circ$  and  $60^\circ$  for various dead layer thicknesses  $\lambda_D$ . A significant slope of  $\varepsilon(E_{\text{PMS}})$  is visible for all  $\lambda_D$ . To

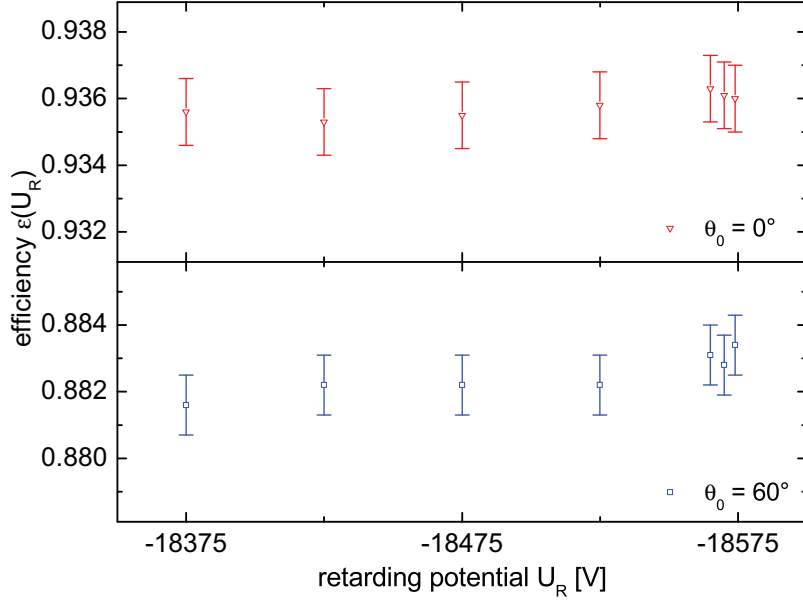


**Figure 6.12:** Simulated focal plane detector efficiency  $\varepsilon(U_R)$  over the retarding potential  $U_R$  for a dead layer thickness  $\lambda_D = 100$  nm, initial energy  $E_{PMS} = 18575$  eV and polar initial angle  $\theta_{PMS} = 0^\circ$  and  $60^\circ$ . The statistical errors are shown. The region of interest is  $15 < E < 21$  keV.

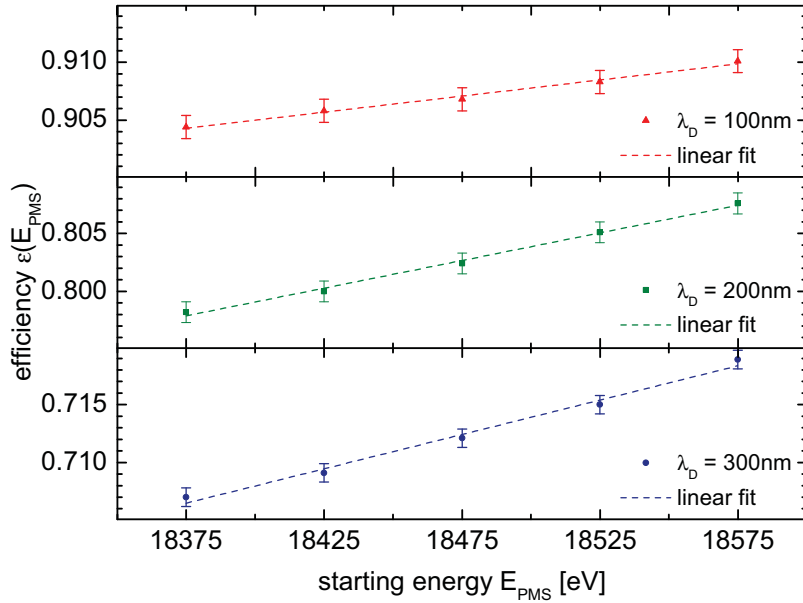


**Figure 6.13:** Simulated focal plane detector efficiency  $\varepsilon(U_R)$  over the initial energy  $E_{PMS}$  for a retarding potential  $U_R = 18370$  V, a initial polar angle  $\theta_{PMS}$  uniformly distributed between  $0^\circ$  and  $60^\circ$  and for dead layer thicknesses of  $\lambda_D = 100, 200$  and  $300$  nm. The statistical errors are shown. The region of interest is  $15 < E < 21$  keV.

quantify the slope  $d\varepsilon(E_{\text{PMS}})/dE$ , a linear fit taking into account the statistical errors of  $\varepsilon(E_{\text{PMS}})$  was applied. The values for slope and offset can be found in Tab. 6.2. Additionally to the average decrease of  $\varepsilon(E_{\text{PMS}})$  for thicker dead layers  $\lambda_{\text{D}}$  also shown in Figure 6.11, the steepness of the slope  $d\varepsilon(E_{\text{PMS}})/dE$  increases too. Both effects can be understood from the shape of the average energy deposition  $E_{\text{dep}}(z)$  over the depth  $z$  in the detector shown in Figure 5.12. The decrease of  $\varepsilon$  for lower  $E_{\text{PMS}}$  is caused by the fact that the  $E_{\text{dep}}(z)$  distribution is basically being compressed for lower incident energies. Therefore the energy deposited in the dead layer is increasing. Thicker dead layers emphasize this effect because they affect areas with an already higher energy deposit. Since all simulated  $\lambda_{\text{D}}$  cut into the region with still rising  $E_{\text{dep}}(z)$ , a steady increase of  $d\varepsilon(E_{\text{PMS}})/dE$  towards higher  $\lambda_{\text{D}}$  is observed. The effect of the statistically significant dependency of  $\varepsilon$  on  $E_{\text{PMS}}$  is discussed below.

### The maximum allowed slope of $d\varepsilon(E_{\text{PMS}})/dE$

The maximum allowed slope  $d\varepsilon(E_{\text{PMS}})/dE$  of the detection efficiency over the electron energy was determined via KATRIN sensitivity calculations under the premise that such an effect would not be corrected for in the analysis.

The detector efficiency is defined as:

$$\varepsilon(E) = \varepsilon(E_0) \times \left(1 - \frac{d\varepsilon}{dE} \times (E_0 - E)\right) \quad (6.6)$$

Here,  $E_0$  denotes an arbitrary reference energy. For convenience the endpoint energy of the tritium spectrum is taken. As noted, the analysis is insensitive on the absolute value of  $\varepsilon(E_0)$  since it is treated as a free parameter.

A large number (10,000) of tritium  $\beta$ -spectra were simulated with the KATRIN design values, taking into account  $d\varepsilon/dE \neq 0$ . The simulated spectra are analyzed with a response function which still assumes  $d\varepsilon/dE = 0$ . This leads to a bias in the mean values of the fit parameters; especially for the fit parameters  $m_\nu^2$  and  $E_0$ . This is understandable, since in the simulated measurement events below the endpoint are "missing" due to the decrease in detection efficiency. The fitting procedure will try to recover this by attributing the deficit to the effect of a finite neutrino mass. The shift of the mean values of the fit parameters is then interpretable as a systematic error on the fit parameters. To meet the KATRIN sensitivity of  $m_\nu < 0.2$  eV (90% C.L.), a single contribution must not exceed  $\Delta m_{\text{sys,max}}^2 < 7.5 \times 10^{-3}$  eV<sup>2</sup>. This kind of statistical approach to determine a systematic error contribution, which is introduced by an unaccounted for correction, is described in detail in the KATRIN Design Report [30]. The analysis package KSOP [98, 97] has been used for these simulations and fitting procedures.

In Figure 6.14, the shift  $\Delta m_\nu^2$  is plotted against different assumptions for  $d\varepsilon(E)/dE$ . Each curve represents a different assumption on the fit interval below the endpoint.

As expected, the larger the chosen fit interval below the endpoint, the stronger the associated bias. Thus, the contribution to the systematic error is increased. The horizontal dashed line shows the KATRIN requirement. For a reference fit interval 50 eV below the endpoint and a maximum contribution of  $\Delta m_{\text{sys,max}}^2 < 7.5 \times 10^{-3} \text{ eV}^2$ , the simulation gives a maximum allowed slope of

$$\frac{d\varepsilon}{dE} = 7.1 \times 10^{-5} / \text{ eV}. \quad (6.7)$$

It should be emphasized that even if  $d\varepsilon/dE$  is measured in advance by a dedicated calibration measurement, changes in the measured slope of the same size must be avoided. The measurement of  $d\varepsilon(E)/dE$  will be accessible through the calibration electron disc of the focal plane detector system (Sec. 3.1).

## Conclusion

The thickness of the dead layer has a significant influence on the detection efficiency as one can see in Figure 6.11. One can derive that for each additional 10 nanometers of dead layer thickness, the total detection efficiency decreases by 0.7% for incident angles of  $0^\circ$ . The efficiency loss is 1.3% for initial angles of  $\theta_{\text{PMS}} = 60^\circ$ . Again, the reason is the increased deposited energy in the detector deadlayer, leading to lower energy deposits in the sensitive detector volume. Therefore, the fraction of events in the region of interest is lowered. This means that not only  $\varepsilon(E_{\text{PMS}})$  will be a function of the deadlayer thickness, but also  $d\varepsilon/dE$ .

Figure 6.13 shows the simulated detection efficiency as a function of the initial energy for three different assumptions on the dead layer ( $\lambda_{\text{D}} = 100 \text{ nm}, 200 \text{ nm}, 300 \text{ nm}$ ) for an electron source with isotropic emission up to  $60^\circ$ . A linear fit to the simulation points gives the corresponding efficiency slopes:

$$\frac{d\varepsilon}{dE}(100 \text{ nm}) = (2.78 \pm 0.16) \times 10^{-5} / \text{ eV} \quad (6.8)$$

$$\frac{d\varepsilon}{dE}(200 \text{ nm}) = (4.78 \pm 0.19) \times 10^{-5} / \text{ eV} \quad (6.9)$$

$$\frac{d\varepsilon}{dE}(300 \text{ nm}) = (5.94 \pm 0.35) \times 10^{-5} / \text{ eV} \quad (6.10)$$

The slope for each dead layer thickness is still under the upper allowed limit from Eq. 6.7. The sensitivity of the focal plane detector calibration devices allows to monitor changes of the detector dead layer with 20 nm accuracy [125]. Despite the visible effects of the dead layer in the detector response, a significant contribution to the neutrino mass analysis can be excluded.

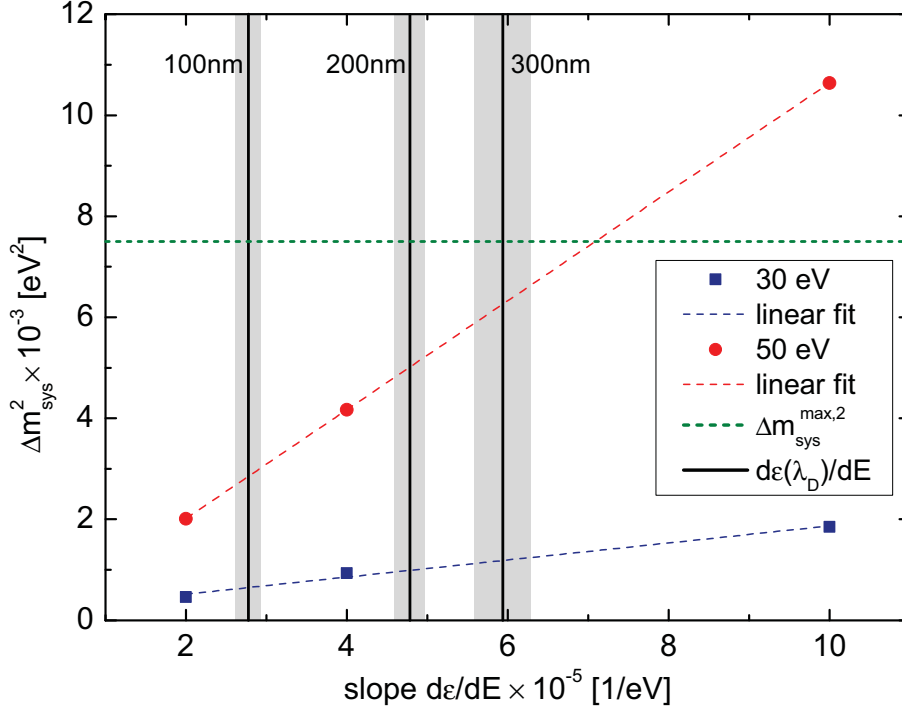


**Figure 6.14:** Systematic error on  $m_\nu^2$  as a function of an energy dependent detection efficiency  $\epsilon$ , which is characterized by the slope  $d\epsilon/dE$ . Each curve represents an analysis with different energy ranges of the examined beta spectrum below the endpoint (red 50 eV, blue 30 eV). The vertical lines show the KESS results for three different dead layer thicknesses  $\lambda_D$ , the grey shade shows the statistical error.

### Time distribution of detector hits

The simulation results presented above assume a low rate of incident at the detector. The maximum time difference between the first and last energy deposit in the sensitive volume is smaller than the DAQ shaping time. For the KATRIN analysis, only the energy interval 50 eV below the tritium endpoint energy is used. The expected count rate is 100 cps, from which in first approximation no pile-up effects are expected. A shaping time of a few  $\mu\text{s}$  is four orders of magnitude below the average time interval between two  $\beta$ -decay electrons. Rarely, pile-up effects can arise because the events are of course not equally distributed over time.

While partial energy deposits from backscattered electrons and the dead layer are described by KESS, partial energy deposits caused by the time distribution of the re-entry of backscattered electrons are a DAQ effect. For the pre-spectrometer test experiment, travel times are of the order of 10 ns. For the main spectrometer, much larger travel times can be expected. The dimensions of the main spectrometer are 5.3 times bigger, which elongates the electron trajectory. High magnetic fields increase the ratio of the transversal energy component to the longitudinal energy component.

Therefore, the electron path is elongated, since the effective movement in  $z$ -direction is shortened. The volume with high magnetic fields which backscattered electrons will traverse is larger for the main spectrometer and focal plane detector setup (Fig. 6.9 and 6.6). The longest time-of-flight for the return of electrons is observed in case of reflection at the main spectrometer potential. The time-of-flight in the main spectrometer is large due to the small longitudinal energy of the electrons.

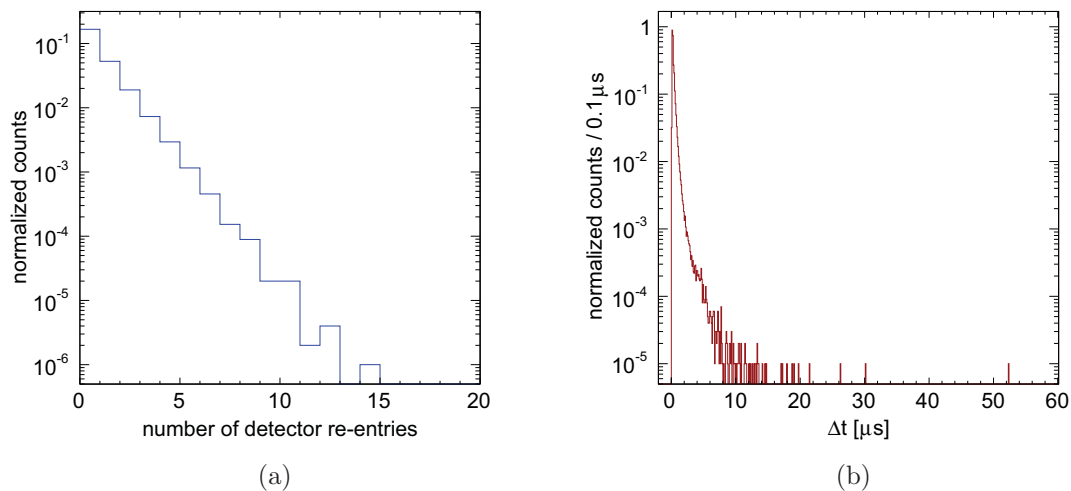


**Figure 6.15: Multiple focal plane detector hits by one electron.**

(a) Number of focal plane detector re-entries of electrons with incidence energy  $E_I = 18.575$  keV and uniformly distributed initial polar angles  $0^\circ < \theta_{\text{PMS}} < 60^\circ$ . A single electron can re-enter the detector up to 14 times. (b) The time difference  $\Delta t$  between the first and the last incidence at the focal plane detector for each primary electron is shown.

The distribution of subsequent re-entries per single electron is shown in Figure 6.15(a). A single electron can re-enter the focal plane detector up to 14 times. The electrons can be reflected at the detector magnet, the pinch magnet or the spectrometer potential. The time between the first and last detector hit of a single electron is shown in Figure 6.15(b). While the mean of the time distribution is  $0.33 \mu\text{s}$ , events with time differences up to  $52 \mu\text{s}$  are observed. The DAQ shaping times currently available with the IPEv4 DAQ range from  $0.1 \mu\text{s}$  to  $12.8 \mu\text{s}$ .

It is therefore necessary to extend *KESS* with a full DAQ simulation for the focal plane detector system, to study the influence of the time distribution of detector re-entries (Fig. 6.15(b)) on the detection efficiency. It was shown in Section 6.1.2 that *KESS* can be used as an input for such a DAQ simulation.

# 7 Summary and Outlook

## 7.1 Summary

The evidence for massive neutrinos and its impact on particle physics and cosmology has triggered the need for the measurement of the neutrino mass. The **K**arlsruhe **T**ritium **N**eutrino experiment KATRIN will determine the electron antineutrino mass with a sensitivity of  $m(\bar{\nu}_e) \leq 0,2 \text{ eV}/c^2$  (90% C.L.). It uses a direct approach by measuring the tritium  $\beta$ -decay spectrum accurately. From the spectral shape, the neutrino mass can be derived. The current upper limit from direct measurements is  $m(\bar{\nu}_e) < 2.3 \text{ eV}/c^2$  (95% C.L.) [1].

In the KATRIN experiment,  $\beta$ -electrons emitted from a gaseous tritium source are magnetically guided to the focal plane detector (FPD) system. The electrons are analyzed in energy by a large electrostatic spectrometer. Electrons with a longitudinal kinetic energy component larger than the spectrometer retarding potential are transmitted and re-accelerated to their original energy and finally hit the focal plane detector.

The focal plane detector is a large ( $\phi = 50 \text{ mm}$ ), monolithic, 148-fold segmented silicon PIN diode and is used to detect electrons with kinetic energies  $E \leq E_0$ , where  $E_0 = 18.6 \text{ keV}$  is the tritium end-point energy. In the current picture of systematic uncertainties on the KATRIN observable  $m_\nu^2$ , no contribution from the focal plane detector is considered. The main purpose of this study was to provide a simulation to determine this contribution by modeling the detector response to low-energy electrons in detail. Due to the electromagnetic design of the main spectrometer and focal plane detector region, backscattering must be described accurately. Note that multiple passages through insensitive detector regions (i.e. dead layer) can occur. After the development and validation of the simulation, it was used to quantify the systematic effects on the neutrino mass measurement for the first time (see below).

It was shown in this study that neither general purpose codes like **Geant4** or **Penelope2008**, nor simple theoretical approaches like the widely used continuous-slowning-down-approximation are sufficient in the case of KATRIN. To successfully describe the detector response of silicon semiconductor detectors to tritium  $\beta$ -electrons, the following must be modeled precisely:

- The energy loss of low-energy electrons in silicon,
- the trajectory of the electron, which can lead to backscattering,

- the energy deposition in the detector including the production and tracking of secondary electrons,
- the charge collection efficiency, where dead layers lead to partial charge collection,
- the amplification chain of the detector signal, and
- the analysis of the detector signal (i.e. data acquisition system, DAQ).

To fulfill these requirements, an event-based Monte Carlo simulation **KESS** (**KATRIN Electron Scattering in Silicon**) based on first principles was developed. It uses doubly differential inelastic collision cross sections to describe the energy loss of electrons in crystalline silicon. Elastic differential cross sections describe the angular deflections during scattering of the electrons with silicon atoms. Knock-on electrons are created from the ionization of inner shells or the collective excitations of the valence band. During the subsequent rearrangement of the shell electrons, Auger electrons are emitted. These secondary electrons take the major part of energy lost by the incident electron away.

The relation between 'energy deposited' and 'charge carriers created' is linear and is accounted for experimentally by the ADC-to-energy calibration. Thus, the explicit creation of charge carrier pairs is omitted in the simulation. **KESS** is a major part of the KATRIN global simulation framework **Kassiopeia**. With the available particle generation and electromagnetic tracking modules, it is possible to simulate complex experimental setups.

Two models to describe the inelastic collisions were compared in this study. One is based on a model dielectric function proposed by Penn [72], the other is based on the first Born approximation for inelastic scattering on free atoms and was proposed by Bethe and Fano [73]. The models agree for electron energies  $E > 500$  eV. At lower electron energies, the speeds of the silicon shell electrons become comparable and the Born approximation breaks down. With Penn's cross sections tracking is possible for electron energies down to 1 eV. Electrons with only a few tens of eV can lead to background for the KATRIN experiment, if they are electromagnetically trapped and ionize residual gas molecules. Here, the Penn model cross sections should be used for electrons with  $E < 40$  keV.

The influence of secondary electrons on the detector response and on backscattering effects was shown in this study. The production and tracking of secondary electrons should be included in the simulation. They contribute to the lower half of the backscattered electron energy spectrum. This includes Auger lines and the 'true' secondary electron peak ( $E < 50$  eV). For comparison, simulations *not* including the creation of secondary electrons were carried out. They show an effective decrease of dead layer effects. If only the highest-energy electrons and the counts in an energy region of interest are required for an analysis, secondary electrons can be neglected.

The primary backscattering coefficient and the secondary backscattering yield in

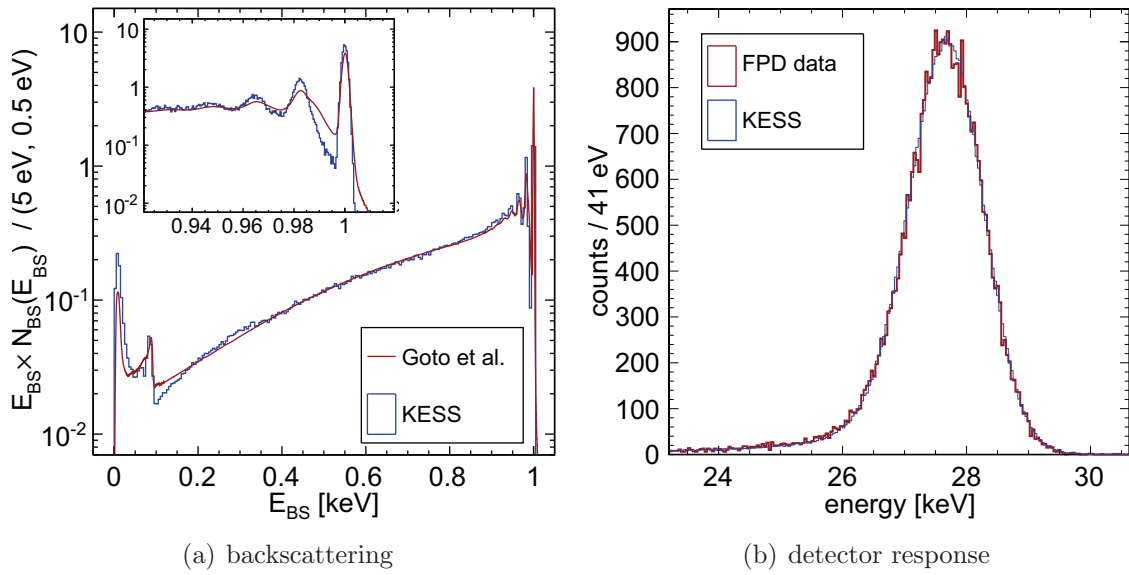


**Figure 7.1: Comparison of KESS to experimental data.** (a) The energy distribution of backscattered electrons obtained with KESS is compared to data from [61]. The incident electron energy is  $E_I = 1$  keV.  $E_{BS}$  is the energy of backscattered electrons and  $N_{BS}(E_{BS})$  is the number of backscattered electrons. For details see Section 5.2.3. (b) The detector response of the focal plane detector to electrons with kinetic energy  $E_I = 30.13$  keV obtained with KESS is compared to measurements carried out by the KATRIN group at the university of Washington (FPD data).

dependence on the incident energy were compared to published experimental data. It was shown from simulations that the secondary backscattering yield is strongly dependent on the electron affinity of the detector surface. The primary backscattering coefficient depends strongly on the polar incident angle. This dependence was verified by comparing KESS simulations to experimental results. For all comparisons good agreement within experimental uncertainties was found.

Experimental data from a spectroscopic measurement [61] was used to evaluate the energy distribution of backscattered electrons. KESS reproduces all visible effects in detail: The elastic peak, plasmon peaks, Auger electron lines and the true secondary peak (Fig. 7.1(a)). The good agreement shows that KESS can be applied to model the backscattering from the focal plane detector and can in principle be used in Auger electron spectroscopy (AES) and reflective electron energy-loss spectroscopy (REELS). The spatial energy distribution at the detector surface and the angular distribution of backscattered electrons were also examined by simulations.

To account for partial charge collection over the depth  $z$  in the detector, two models describing the dead layer were evaluated. The first approach is the commonly used step function dead layer  $C_S(z) = \Theta_\lambda(z)$ , where no charge is collected in a thickness  $\lambda$  below the detector surface. The second approach approximates detailed calcu-

lations of the charge collection efficiency by assuming  $C_E(z) = 1 - e^{-z/\tau}$ . It was shown that a step function dead layer is a good approximation for the focal plane detector in neutrino mass measurements, since the interval of incident energies is small. However, the detailed calculation or measurements of the charge collection efficiency is preferable to overcome systematic effects in the simulation, depending on the incident energy.

KESS results were compared to experimental energy spectra of the focal plane detector as well as the forward beam monitor detector to show the application of KESS to KATRIN detectors. The analysis for three arbitrary focal plane detector pixels were shown. The dead layer was treated as a free parameter and the central values of the ADC-to-energy calibration were modified inside their errors. The reduced  $\bar{\chi}^2$  and  $\bar{p}$ -values, averaged over all incident energies for each pixel are

$$\begin{aligned} \text{Pixel 52 : } \bar{\chi}^2 &= 1.74, \bar{p} = 0.02 \\ \text{Pixel 61 : } \bar{\chi}^2 &= 1.15, \bar{p} = 0.11 \\ \text{Pixel 140 : } \bar{\chi}^2 &= 1.14, \bar{p} = 0.24. \end{aligned}$$

The worse agreement for pixel 52 remains unexplained, but is most likely related to experimental issues. However, the simulated detector response of the focal plane detector agreed well for pixel 61 and 140 (Fig. 7.1(b)). The calculated dead layer thicknesses disagree with earlier measurements of a detector with the same manufacturing technique [54]. The same disagreement is also found from an analysis independent from KESS simulations. This can be explained by a vacuum breakdown prior to the focal plane detector measurement [119]: Gas molecules have a probability to stick to the cold detector surface and effectively enlarge the dead layer thickness. It is suggested that the analysis be repeated for measurements with a clean detector surface and extended to all focal plane detector pixels. To obtain the dead layer thickness from experimental data, the spectral shape of the detector response has to be taken into account. Dead layer measurements have to be interpreted by detailed simulations (i.e. KESS) to yield accurate results. A simplified theoretical model, the continuous-slowning-down-approximation, leads to systematically lower dead layer thicknesses of  $\sim 30\%$ .

The forward beam monitor detector will detect the complete  $\beta$ -spectrum and will have high count rates. In contrast to the focal plane detector, it is based on silicon-drift-detector technology. To account for effects (i.e. pile-up) arising from the signal amplification and signal analysis at high rates of incidence, KESS was extended by the KDES package written by M. Babutzka [40]. The good agreement with the experimentally obtained detector response implies that KESS can be used as an input for simulations of the detector electronics. In addition, it was shown that KESS can model the detector response of PIN diodes and silicon drift detectors.

Measurements of transmission functions of the pre-spectrometer test experiment [3] showed a loss in count rate for electrons with increasing energies greater than the

spectrometer retarding potential. If this effect would have been caused by the pre-spectrometer itself, the requirement for adiabatic transport would not be fulfilled. Detailed simulations with **KESS** as a part of **Kassiopeia** showed that the effect is fully accounted for by electron backscattering from the detector, the magnetron drift and non-adiabatic transport of backscattered electrons in the electron emitter (e-gun). The loss in count rate is caused by the external components (i.e. detector and e-gun) of the test experiment. No violation of adiabaticity in the pre-spectrometer itself was observed. Therefore, the pre-spectrometer fulfills the requirements for KATRIN with regard to adiabatic transport. Moreover, this analysis showed unambiguously the need to include detailed backscattering simulations in the data analysis to describe and understand the measured spectra correctly.

Finally, the expected contribution of statistic and systematic errors on the KATRIN observable  $m_\nu^2$  were calculated with **Kassiopeia** simulations. The average detection efficiency was calculated, taking into account the angular distribution of electrons hitting the focal plane detector and a dead layer of  $\lambda_D = 100$  nm. It is compatible with the estimated detection efficiency of  $\varepsilon = 0.9$  used to calculate the expected statistical error. However, the design values and the measurements [54] of the dead layer had been derived by the continuous-slown-down-approximation. **KESS** dead layers are generally thicker, since **KESS** accounts for energy loss straggling in detail. Therefore, the detection efficiency  $\varepsilon$  in dependence on the dead layer thickness was also calculated. Note that the dependence of the detection efficiency on the polar incident angle is of special importance, as most calibration measurements at KATRIN are done with artificial electron emitters with fixed angle of emittance [108, 109]. It is therefore necessary to include this dependency in the analysis and when extrapolating to an isotropically emitting source (e.g. transmission function measurements).

For the first time the effects on the systematic error were examined under the assumption that the detection efficiency shows a dependence on the electron energy or the spectrometer retarding potential. This analysis sets upper limits for allowed unaccounted slopes of  $d\varepsilon/dE < 7.1 \times 10^{-5}/\text{eV}$  from the restriction of a maximum allowed contribution to the systematic error of  $\Delta m_{sys,max}^2 < 7.5 \times 10^{-3} \text{eV}^2$ . No statistically significant slope  $d\varepsilon/dU_R$  with regard to a changing spectrometer retarding potential  $U_R$  was found. For the dependence on the electron energy, the following slopes

$$\begin{aligned} \frac{d\varepsilon}{dE}(\lambda_D = 100 \text{ nm}) &= (2.78 \pm 0.16) \times 10^{-5}/\text{eV} \\ \frac{d\varepsilon}{dE}(\lambda_D = 200 \text{ nm}) &= (4.78 \pm 0.19) \times 10^{-5}/\text{eV} \\ \frac{d\varepsilon}{dE}(\lambda_D = 300 \text{ nm}) &= (5.94 \pm 0.35) \times 10^{-5}/\text{eV} \end{aligned}$$

for different dead layer thicknesses  $\lambda_D$  were found. Note that a  $\lambda_D = 300$  nm **KESS** dead layer corresponds to a dead layer calculated from the continuous-slown-down-

approximation of  $\lambda_{\text{CSDA}} = 223 \text{ nm}$ . The slopes for each dead layer are less than the upper allowed limit. The sensitivity of the focal plane detector calibration devices allow to monitor changes of the detector dead layer with 20 nm accuracy. Therefore, it can be concluded that despite the visible effects of the dead layer in the detector response, the contribution to the neutrino mass analysis will be small.

Finally, the time interval between the first and last detector incident  $\Delta t$  for a single electron were investigated. While the mean of the time distribution is  $\Delta t = 0.33 \mu\text{s}$ , the distribution is broad and events with time differences up to  $\Delta t = 52 \mu\text{s}$  were observed. The DAQ shaping times currently available range from  $0.1 \mu\text{s}$  to  $12.8 \mu\text{s}$ . It is therefore necessary to extend KESS with a full DAQ simulation for the FPD system, to investigate the impact on the detection efficiency. As mentioned above, it was shown in this study that KESS can be used as an input for such a DAQ simulation.

## 7.2 Outlook

In a future version of KESS, the energy losses during elastic collisions should also be considered. A worst case estimate shows that 18 keV electrons will lose up to 1.4 eV in an elastic collision with a free silicon atom in case of total reflection. As a first step, the energy loss  $\Delta E_{\text{ES}}$  can be calculated from the collision with a free atom [126] following

$$\Delta E_{\text{ES}} = 4 \frac{m_e}{M_{\text{Si}}} E \cdot \sin^2 \frac{\Theta_{\text{ES}}}{2}, \quad (7.1)$$

with the electron mass  $m_e$ , the mass of the silicon atom  $M_{\text{Si}}$  and the elastic scattering angle  $\Theta_{\text{ES}}$ . Note that this elastic energy loss depends on the electron energy  $E$ . For small scattering angles ( $\Theta_{\text{ES}} < \pi/2$ ) equation 7.1 overestimates the energy loss, since the influence of the crystal on the effective mass of  $M_{\text{Si}}$  increases. More details and references to theoretical descriptions can be found in [127]. The results obtained from the simulation can then be compared to the incident-energy dependent shift of the elastic peak, observed in reflective and especially angular resolved energy-loss spectroscopy experiments.

Bulk plasmon and interband transitions are included in the Penn model inelastic collision cross sections. At the detector surface however, surface plasmons with  $E_{\text{S}} = \hbar\omega_{\text{S}} \approx 11 \text{ eV}$  and surface-state transitions with  $E_{\text{ST}} \approx 2$  and  $7.5 \text{ eV}$  are neglected in KESS. Spectra from reflective electron energy-loss spectroscopy for a clean surface and after an exposure to  $\text{O}_2$  are given in [113, Fig. 1]. It is likely that these energy dependent energy losses, occurring during the surface escape process, can improve the agreement between measurement and simulation in Figure 5.7(b). A difference is visible in the energy range between the elastic peak and the first bulk plasmon peak for low incidence energies.

KESS calculations can easily be extended to keV x-rays. In first approximation, x-

rays transfer their full energy to an electron in a single interaction. In principle, only the position where this photoelectron is created, its direction and its kinetic energy must be given to *KESS*. The detector response is then calculated in the usual way. This would also allow the comparison to x-ray photoelectron spectroscopy (XPS) measurements. In a second step, Compton scattering can be included to further increase the detail.

It was shown in Sections 6.2.2 and 5.2 that 25% of all incident electrons are backscattered at least once from the focal plane detector. Together with multiple backscattering (Fig. 6.15(a)) and additional secondary electrons emitted from the detector (Sec. 5.2), the number of electrons between the spectrometer retarding potential and the focal plane detector is significantly increased. These electrons can collide with residual gas molecules. This can lead to a non-adiabatic change of the angle between electron momentum and the magnetic field line. Thus, electrons can be trapped electromagnetically (e.g. in Penning traps). These traps can fill and contribute to background by subsequent collisions with residual gas molecules. *KESS* models the electron backscattering and the production of secondary electrons in detail. Therefore, it is now feasible to investigate this possible background. A simulation taking into account electromagnetic tracking and detector backscattering is proposed, similar to the one in Section 6.2.2. However, the production of secondary electrons (available in *KESS*) and the scattering with residual gas molecules (available in *Kassiopeia*) must be included in this new simulation.



# A Appendix

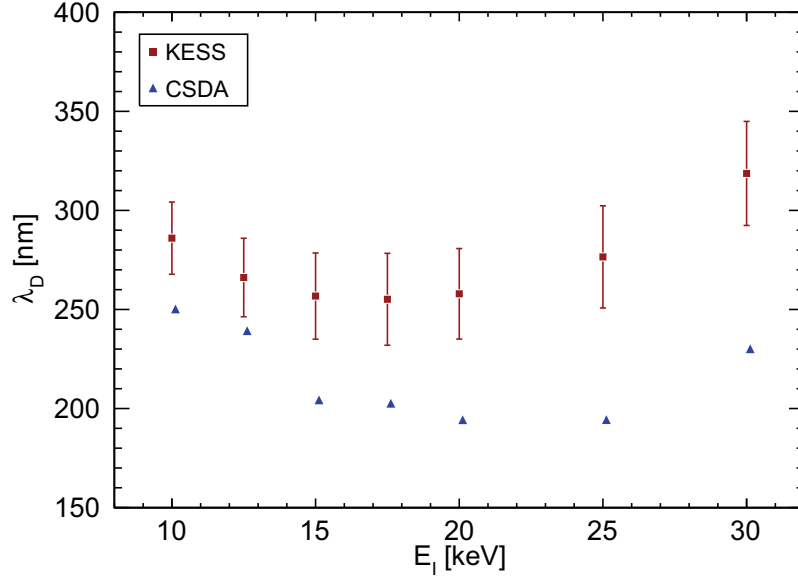
## A.1 Standard KESS simulation settings

Table A.1: Standard simulation settings used, if not stated otherwise.

parameter	symbol	value
dead layer thickness	$\lambda_D$	100 nm
detector thickness	$t$	500 $\mu\text{m}$
incident angle	$\theta_I$	0°
electron affinity	$\chi$	4.05 eV
$E_{\text{CBM}} - E_{\text{F}}$		0.56 eV
transmission probability	$T$	yes
electron energy cut	$E_C$	$\chi - 0.5 \text{ eV}$
create secondaries		yes
inelastic model	CCS	Penn
elastic model	DCS	see sec. 4.2.2
knock-on secondary angle		spherical symmetry
ionization model	ICS	see sec. 4.3.1
energy region of interest	ROI	$15 < E < 21 \text{ keV}$
number of incident electrons	$N_I$	$10^6$

## A.2 Additional focal plane detector figures

This section shows the final results of the comparison of KESS simulations to focal plane detector data from Sec. 6.1.1 for pixel 61 and pixel 52.



**Figure A.1: Best-fit dead layer values for pixel 61.** Plotted are the KESS dead layer thicknesses with lowest  $\chi^2$  over  $E_I$ . The error shown is the uncertainty of the  $\chi^2$ -fit. Results obtained with the continuous-slowing-down-approximation (CSDA) are shown for comparison. The energy calibration is  $E(\text{in keV}) = (3.83 \pm 0.04) \cdot 10^{-2} \text{ keV/chan.} \cdot \text{ADC} + (0.07 \pm 0.58) \text{ keV}$ . In addition, the energy calibration offset was changed by  $\delta = -0.49 \text{ keV}$  and the slope by  $\gamma = 0.82 \times 10^{-3} \text{ keV/channel}$ .

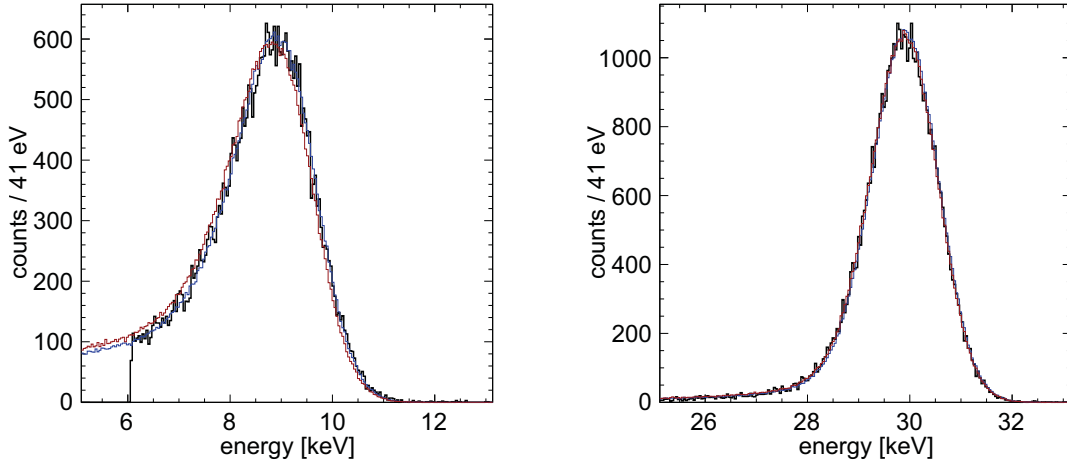


**Figure A.2: Comparison of FPD data to simulations for pixel 61 with a modified energy calibration.** Measurement data (black) compared to the two simulations with lowest  $\chi^2$ . The energy calibration offset was changed by  $\delta = -0.49 \text{ keV}$  and the slope by  $\gamma = 0.82 \times 10^{-3} \text{ keV/channel}$ . **(a)** Incident energy  $E_I = 10.12 \text{ keV}$  (blue) dead layer thickness  $\lambda_D = 280 \text{ nm}$ ,  $\chi^2 = 1.08$  (red)  $\lambda_D = 300 \text{ nm}$ ,  $\chi^2 = 2.35$  and **(b)**  $E_I = 30.13 \text{ keV}$  (blue)  $\lambda_D = 300 \text{ nm}$ ,  $\chi^2 = 1.67$  (red)  $\lambda_D = 320 \text{ nm}$ ,  $\chi^2 = 1.13$ .

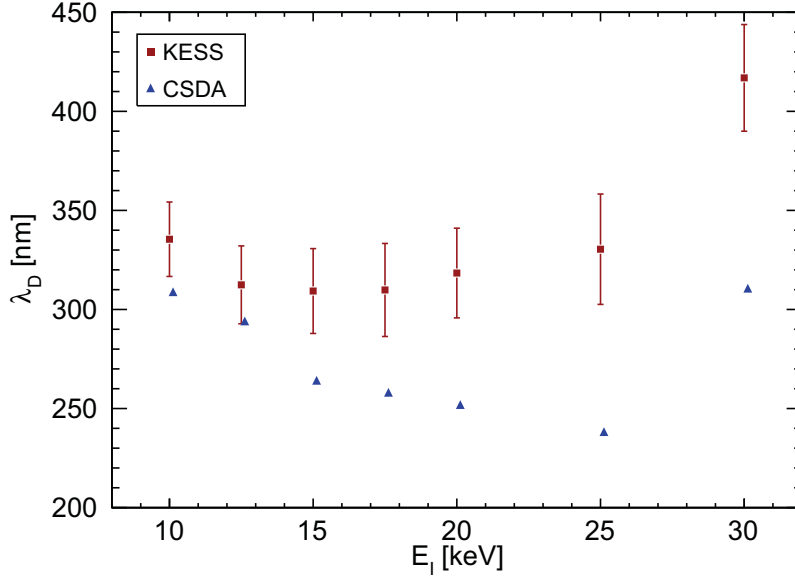


**Figure A.3: Best-fit dead layer values for pixel 52.** Plotted are the KESS dead layer thicknesses with lowest  $\chi^2$  over  $E_I$ . The error shown is the uncertainty of the  $\chi^2$ -fit. Results obtained with the continuous-slowng-down-approximation (CSDA) are shown for comparison. The energy calibration was  $E(\text{in keV}) = (4.09 \pm 0.04) \cdot 10^{-2} \text{ keV/chan.} \cdot \text{ADC} + (0.60 \pm 0.55) \text{ keV}$ . In addition, the energy calibration offset is changed by  $\delta = -0.34 \text{ keV}$  and the slope by  $\gamma = 0.82 \times 10^{-3} \text{ keV/channel}$ .

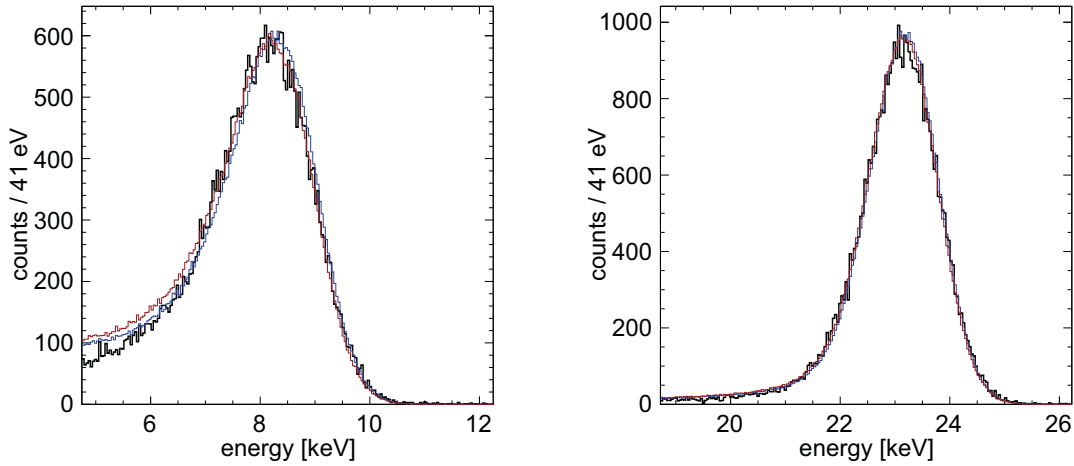


**Figure A.4: Comparison of FPD data to simulations for pixel 52 with a modified energy calibration.** Measurement data (black) compared to the two simulations with lowest  $\chi^2$ . The energy calibration offset was changed by  $\delta = -0.34 \text{ keV}$  and the slope by  $\gamma = 0.82 \cdot 10^{-3} \text{ keV/channel}$ . (a) Incident energy  $E_I = 10.12 \text{ keV}$  (blue) dead layer thickness  $\lambda_D = 320 \text{ nm}$ ,  $\chi^2 = 1.83$  (red)  $\lambda_D = 340 \text{ nm}$ ,  $\chi^2 = 1.56$  and (b)  $E_I = 25.13 \text{ keV}$  (blue)  $\lambda_D = 320 \text{ nm}$ ,  $\chi^2 = 1.66$  (red)  $\lambda_D = 340 \text{ nm}$ ,  $\chi^2 = 1.68$ .



# Acknowledgements

At this point I would like to thank everyone who supported me during my Ph.D. years. I am especially grateful to:

- Prof. Dr. J. Blümer for giving me the opportunity to work in this very interesting field of physics and for accepting the function of first reviewer,
- Prof. Dr. G. Quast for kindly accepting the function of second reviewer,
- Prof. Dr. G. Drexlin for giving me the opportunity to contribute to the KATRIN project, for his support and advice,
- Dr. M. Steidl for his constant support and the discussions on my work and detector physics,
- Prof. Dr. H. Bichsel (University of Washington) and Prof. Dr. Z. Chaoui (University of Setif, Algeria) for guidance, advice and many fruitful discussions and hints,
- Prof. Dr. R.G.H. Robertson, Prof. Dr. P. Doe, Prof. Dr. H. Bichsel, Dr. A. Cox and the whole Seattle KATRIN group for welcoming me at the University of Washington during my academic stay abroad,
- Dr. F. Glück and the international KATRIN simulation group for the great teamwork as well as help with electromagnetic simulations,
- the KALINKA and TESLA cluster administrators as well as T. Csabo for their technical support.

Finally, I want to thank my parents, family and friends for their ongoing support during all parts of my life.

My stay abroad at the University of Washington, Seattle, USA was funded by the Karlsruhe House of Young Scientists (KHYS). This work was funded by the Deutsche Forschungsgemeinschaft (DFG Transregio 27: *Neutrinos and Beyond*).



# Bibliography

- [1] C. Kraus, B. Bornschein, L. Bornschein, J. Bonn, B. Flatt, et al. (2005): *Final results from phase II of the Mainz neutrino mass search in tritium  $\beta$ -decay*. The European Physical Journal C - Particles and Fields 40 447.
- [2] K. Nakamura and Particle Data Group (2010): *Review of Particle Physics*. Journal of Physics G: Nuclear and Particle Physics 37(7A) 075021.
- [3] M. Prall (2011): *The KATRIN Experiment: Transmission Function of the Pre-Spectrometer and Quality Assurance of the Wire Electrode System*. Ph.D. thesis in preparation, Universität Münster.
- [4] W. Pauli (1964): *Offener Brief an die Gruppe der Radioaktiven bei der Gauvereinstagung zu Tübingen (4. Dez. 1930)*. R. Kronig and V. Weisskopf, Collected Scientific Papers 2 1316.
- [5] J. Chadwick (1914): *The intensity distribution in the magnetic spectrum of  $\beta$ -rays of Radium B + C*. Verh. d. D. Phys. Ges. 16 383.
- [6] E. Fermi (1934): *Versuch einer Theorie der  $\beta$ -Strahlen*. Zeitschrift f. Phys. A 88 161.
- [7] F. Reines and C. L. Cowan (1953): *Detection of the Free Neutrino*. Phys. Rev. 92(3) 830.
- [8] G. Danby et al., *Observation of high-energy neutrino reactions and the existence of two kinds of neutrinos*. In K. Winter (ed.), *Neutrino Physics*, p. 57 (1991).
- [9] K. Kodama et al. (2001): *Observation of tau-neutrino interactions*. Phys. Lett. B504 218.
- [10] M. Goldhaber, L. Grodzins, and A. W. Sunyar (1958): *Helicity of Neutrinos*. Phys. Rev. 109(3) 1015.
- [11] M. Gaillard, P. Grannis, and F. Sciulli (1999): *The standard model of particle physics*. Rev. Mod. Phys. 71(2) S96.
- [12] B. Povh, K. Rith, and C. Scholz, *Teilchen und Kerne* (Springer, 2004).
- [13] S. Eidelman et al. (2004): *Rev. Part. Phys.* Phys. Lett. B 592 1.

## Bibliography

- [14] Y. Fukuda et al. (1998): *Evidence for Oscillation of Atmospheric Neutrinos*. Phys. Rev. Lett. 81(8) 1562.
- [15] B.T. Cleveland et al. (1998): *Measurement of the solar electron neutrino flux with the Homestake chlorine detector*. Astrophys. J. 496 505.
- [16] GALLEX Collaboration (1999): *GALLEX solar neutrino observations: results for GALLEX IV*. Phys. Lett. B 447 127.
- [17] J. Abdurashitov, E. Veretenkin, V. Vermul, V. Gavrin, S. Girin, et al. (2002): *Solar neutrino flux measurements by the Soviet-American gallium experiment (SAGE) for half the 22-year solar cycle*. Journal of Experimental and Theoretical Physics 95 181. 10.1134/1.1506424.
- [18] J.N. Abdurashitov et al. (2006): *The BNO-LNGS joint measurement of the solar neutrino capture rate in  $^{71}\text{Ga}$* . Astropart. Phys. 25 349.
- [19] J. Bahcall, A. Serenelli, and S. Basu (2006): *10,000 standard solar models: A Monte Carlo simulation*. Astrophys. J. Suppl. 165 400.
- [20] SNO Collaboration (2002): *Direct Evidence for Neutrino Flavor Transformation from Neutral-Current Interactions in the Sudbury Neutrino Observatory*. Phys. Rev. Lett. 89 011301.
- [21] P.C. de Holanda and A.Y. Smirnov (2003): *LMA MSW solution of the solar neutrino problem and first KamLAND results*. JCAP 2003(02) 001.
- [22] S. P. Rosen and J. M. Gelb (1986): *Mikheyev-Smirnov-Wolfenstein enhancement of oscillations as a possible solution to the solar-neutrino problem*. Phys. Rev. D 34(4) 969.
- [23] L. Wolfenstein (1978): *Neutrino oscillations in matter*. Phys. Rev. D 17(9) 2369.
- [24] J. Bahcall, M. Gonzalez-Garcia, and C. Pena-Garay (2001): *Global analysis of solar neutrino oscillations including SNO CC measurement*. JHEP 2001(08) 014.
- [25] G. Fogli, E. Lisi, A. Marrone, and A. Palazzo (2006): *Global analysis of three-flavor neutrino masses and mixings*. Prog. Part. Nucl. Phys. 57 742.
- [26] C. Arpesella, G. Bellini, J. Benziger, S. Bonetti, B. Caccianiga, et al. (2008): *First real time detection of  $^7\text{Be}$  solar neutrinos by Borexino*. Physics Letters B 658(4) 101.
- [27] KamLAND Collaboration (2005): *Measurement of Neutrino Oscillation with KamLAND: Evidence of Spectral Distortion*. Phys. Rev. Lett. 94 081801.

- [28] SNO Collaboration (2005): *Electron Energy Spectra, Fluxes, and Day-Night Asymmetries of  $^8\text{B}$  Solar Neutrinos from the 391-Day Salt Phase SNO Data Set*. Phys. Rev. C 72 055502.
- [29] KamLAND Collaboration (2003): *First Results from KamLAND: Evidence for Reactor Anti-Neutrino Disappearance*. Phys. Rev. Lett. 90 021802.
- [30] KATRIN Collaboration (2005): *KATRIN Design Report 2004*. Tech. Rep. FZKA 7090, Forschungszentrum Karlsruhe.
- [31] S. Pastor and J. Lesgourgues (2000): *Relic neutrino asymmetry, CMB and large scale structure*. Nucl. Phys. Proc. Suppl. 81 47.
- [32] G. Fiorentini and B. Ricci (2002): *What have we learnt about the Sun from the measurement of the  $^8\text{B}$  neutrino flux?* Phys. Lett. B 526 186.
- [33] A. B. Balantekin, C. Volpe, and J. Welzel (2007): *Impact of the neutrino magnetic moment on the neutrino fluxes and the electron fraction in core-collapse supernovae*. Journal of Cosmology and Astroparticle Physics 2007(09) 016.
- [34] M. Wojcik (2006): *The  $^{76}\text{Ge}$  Double-Beta Decay Experiment GERDA at LNGS*. Acta Physica Polonica B 37(7) 1923.
- [35] EXO Collaboration (2005): *EXO: an advanced Enriched Xenon double-beta decay Observatory*. Nucl. Phys. B Proc. Suppl. 138 224.
- [36] E. Majorana (1937): *Teoria simmetrica dell'elettrone e del positrone*. Nuovo Cimento 14 171.
- [37] A. Dietz (2003): *Auswertung des neutrinolosen Doppelbetazerfalls von  $^{76}\text{Ge}$  im Heidelberg-Moskau-Experiment mit verbesserten statistischen Methoden*. Ph.D. thesis, Ruprecht-Karls-Universität Heidelberg.
- [38] A. Monfardini, C. Arnaboldi, C. Brofferio, S. Capelli, F. Capozzi, et al. (2006): *The microcalorimeter arrays for a rhenium experiment (MARE): A next-generation calorimetric neutrino mass experiment*. Nuclear Instruments and Methods in Physics Research Section A: Accelerators, Spectrometers, Detectors and Associated Equipment 559(2) 346. Proceedings of the 11th International Workshop on Low Temperature Detectors - LTD-11.
- [39] G. Altarelli and K. Winter (eds.), *Neutrino Mass*, vol. 190 (Springer, 2003).
- [40] M. Babutzka (2010): *Untersuchung eines verfahrenbaren Monitordetektors zur Überwachung der Aktivität des  $\beta$ -Zerfalls in der kryogenen Pumpstrecke des KATRIN-Experiments*. Diploma thesis, Universität Karlsruhe.

- [41] R.G.H. Robertson (2007): *Possible Technique for Absolute Calibration of Si Focal Plane Detector for KATRIN*. Draft v1.0, unpublished.
- [42] S. Wüstling, T. Armbrust, M. Steidl, and S. Zadorozhny (2006): *A large, 64-pixel PIN-diode detector for low-energy beta-electrons*. Nuclear Instruments and Methods in Physics Research Section A: Accelerators, Spectrometers, Detectors and Associated Equipment 568(1) 382. New Developments in Radiation Detectors - Proceedings of the 10th European Symposium on Semiconductor Detectors, 10th European Symposium on Semiconductor Detectors.
- [43] S. Wuestling, F. Fraenkle, F. Habermehl, P. Renschler, and M. Steidl (2010): *Results from a 64-pixel PIN-diode detector system for low-energy beta-electrons*. Nuclear Instruments and Methods in Physics Research Section A: Accelerators, Spectrometers, Detectors and Associated Equipment 624(2) 295. New Developments in Radiation Detectors - Proceedings of the 11th European Symposium on Semiconductor Detectors, 11th European Symposium on Semiconductor Detectors.
- [44] U. Schmitt (2008): *Entwicklung eines Monitordetektors für das KATRIN-Experiment*. Ph.D. thesis, Universität Karlsruhe.
- [45] P. Doe (2008): *Status of the focal plane detector (FPD)*. Presentation at the XVth KATRIN Collaboration Meeting.
- [46] M. L. Leber (2010): *Monte Carlo Calculations of the Intrinsic Detector Backgrounds for the Karlsruhe Tritium Neutrino Experiment*. Ph.D. thesis, University of Washington.
- [47] F. Fränkle (2006): *Erste Messungen der elektromagnetischen Eigenschaften des KATRIN Vorspektrometers*. Diploma thesis, Universität Karlsruhe.
- [48] F. Habermehl (2009): *Electromagnetic measurements with the KATRIN pre-spectrometer*. Ph.D. thesis, Universität Karlsruhe.
- [49] F. Fränkle (2010): *Background investigations of the KATRIN pre-spectrometer*. Ph.D. thesis, Universität Karlsruhe.
- [50] K. A. Hugenberg (2008): *Design of the electrode system for the KATRIN main spectrometer*. Diploma thesis, Universität Münster.
- [51] Z. Pei and C. N. Berglund (2002): *Angular Distribution of Photoemission from Gold Thin Films*. Japanese Journal of Applied Physics 41(Part 2, No. 1A/B) L52.
- [52] F. Glück (2010): *personal communication*.

- [53] P. Renschler (2007): *Inbetriebnahme und Charakterisierung von Detektorsystemen für elektromagnetische Tests von Spektrometern*. Diploma thesis, Universität Karlsruhe.
- [54] B. Wall, T. Burritt, P. Doe, C. Fredericks, H. Gemmeke, et al., *Dead layer measurements for KATRIN prototype PIN diode array*. In *Nuclear Science Symposium Conference Record, 2006. IEEE*, vol. 1, pp. 204–207 (2006).
- [55] M. Schlösser (2009): *First Laser Raman measurements with tritium for KATRIN and studies of systematic effects of the LARA-setup*. Diploma thesis, Universität Karlsruhe.
- [56] W. Leo, *Techniques for Nuclear and Particle Physics Experiments* (Springer, 1987).
- [57] M. Steidl (2005): *KATRIN sensitivity in dependance of detector performance*. Katrin internal document 40-ME-2013-1.
- [58] M. Berger, J. Coursey, M. Zucker, and J. Chang, *Stopping-Power and Range Tables for Electrons, Protons, and Helium Ions* (NIST, 2005).
- [59] D. Smith, M. Inokuti, W. Karstens, and E. Shiles (2006): *Mean excitation energy for the stopping power of light elements*. Nuclear Instruments and Methods in Physics Research Section B: Beam Interactions with Materials and Atoms 250(1-2) 1 . Radiation Effects in Insulators - Proceedings of the 13th International Conference on Radiation Effects in Insulators (REI-2005).
- [60] H. Bichsel (1990): *Inelastic electronic collision cross sections for Monte Carlo calculations*. Nuclear Instruments and Methods in Physics Research Section B: Beam Interactions with Materials and Atoms 52(2) 136.
- [61] K. Goto, N. Sakakibara, Y. Takeichi, Y. Numata, and Y. Sakai (1994): *True Auger spectral shapes: A step to standard spectra*. Surface and Interface Analysis 22(1-12) 75.
- [62] D. C. Joy (1995): *A database on electron-solid interactions*. Scanning 17 270.
- [63] R. Shimizu, Y. Kataoka, T. Matsukawa, T. Ikuta, K. Murata, et al. (1975): *Energy distribution measurements of transmitted electrons and Monte Carlo simulation for kilovolt electron*. Journal of Physics D: Applied Physics 8(7) 820.
- [64] H. Bichsel (1988): *Straggling in thin silicon detectors*. Rev. Mod. Phys. 60(3) 663.
- [65] S. Agostinelli, J. Allison, K. Amako, J. Apostolakis, H. Araujo, et al. (2003): *Geant4 - a simulation toolkit*. Nuclear Instruments and Methods in Physics Research Section A: Accelerators, Spectrometers, Detectors and Associated Equipment 506(3) 250.

## Bibliography

- [66] F. Salvat, J. M. Fernandez-Varea, and J. Sempau, *PENELOPE—A code system for Monte Carlo simulation of electron and photon transport* (OECD Nuclear Energy Agency, Issy-les-Moulineaux, France, 06).
- [67] E. Poon, J. Seuntjens, and F. Verhaegen (2005): *Consistency test of the electron transport algorithm in the GEANT4 Monte Carlo code*. *Physics in Medicine and Biology* 50(4) 681.
- [68] E. Poon and F. Verhaegen (2005): *Accuracy of the photon and electron physics in GEANT4 for radiotherapy applications*. *Medical Physics* 32(6) 1696.
- [69] H. Bichsel (2006): *A method to improve tracking and particle identification in TPCs and silicon detectors*. *Nuclear Instruments and Methods in Physics Research Section A: Accelerators, Spectrometers, Detectors and Associated Equipment* 562(1) 154.
- [70] R. F. Egerton (2009): *Electron energy-loss spectroscopy in the TEM*. *Reports on Progress in Physics* 72(1) 016502.
- [71] A. Winkelmann, K. Aizel, and M. Vos (2010): *Electron energy loss and diffraction of backscattered electrons from silicon*. *New Journal of Physics* 12(5) 053001.
- [72] D. R. Penn (1987): *Electron mean-free-path calculations using a model dielectric function*. *Phys. Rev. B* 35(2) 482.
- [73] U. Fano (1963): *Penetration of Protons, Alpha Particles, and Mesons*. *Annual Review of Nuclear Science* 13(1) 1.
- [74] H. Bethe (1930): *Zur Theorie des Durchgangs schneller Korpuskularstrahlen durch Materie*. *Annalen der Physik* 397(3) 325.
- [75] Z.-E.-A. Chaoui (2009): *personal communication*.
- [76] D. R. Penn (1962): *Wave-Number-Dependent Dielectric Function of Semiconductors*. *Phys. Rev.* 128(5) 2093.
- [77] A. Jablonski, F. Salvat, and C. Powell (2004): *Comparison of electron elastic-scattering cross sections calculated from two commonly used atomic potentials*. *Journal of Physical and Chemical Reference Data* 33(2) 409. Cited By (since 1996) 93.
- [78] F. Salvat, A. Jablonski, and C. J. Powell (2005): *ELSEPA—Dirac partial-wave calculation of elastic scattering of electrons and positrons by atoms, positive ions and molecules*. *Computer Physics Communications* 165(2) 157.

- [79] A. Jablonski, F. Salvat, and C. J. Powell (2004): *Differential cross sections for elastic scattering of electrons by atoms and solids*. Journal of Electron Spectroscopy and Related Phenomena 137-140 299. ICES-9 Proceedings of the 9th International Conference on Electronic Spectroscopy and Structure.
- [80] A. Jablonski, F. Salvat, and C. J. Powell (2005): *Evaluation of elastic-scattering cross sections for electrons and positrons over a wide energy range*. Surface and Interface Analysis 37(12) 1115.
- [81] A. Jablonski, F. Salvat, and C. J. Powell, *NIST Electron Elastic-Scattering Cross-Section Database - Version 3.2* (National Institute of Standards and Technology, Gaithersburg, MD, 2010).
- [82] D. T. Cromer and D. Liberman (1970): *Relativistic Calculations of Anomalous Scattering Factors for X Rays*. LANL Report .
- [83] G. Fraser, A. Abbey, A. Holland, K. McCarthy, A. Owens, et al. (1994): *The X-ray energy response of silicon Part A. Theory*. Nuclear Instruments and Methods in Physics Research Section A: Accelerators, Spectrometers, Detectors and Associated Equipment 350(1-2) 368.
- [84] M. Gryziński (1965): *Classical Theory of Atomic Collisions. I. Theory of Inelastic Collisions*. Phys. Rev. 138(2A) A336.
- [85] E. Casnati, A. Tartari, and C. Baraldi (1982): *An empirical approach to K-shell ionisation cross section by electrons*. Journal of Physics B: Atomic and Molecular Physics 15(1) 155.
- [86] E. Casnati, A. Tartari, and C. Baraldi (1983): *An empirical approach to K-shell ionisation cross section by electrons*. Journal of Physics B: Atomic and Molecular Physics 16(3) 505.
- [87] M. P. Seah and I. S. Gilmore (1998): *Quantitative AES VII. The ionization cross-section in AES*. Surface and Interface Analysis 26(11) 815.
- [88] D. Bote and F. Salvat (2008): *Calculations of inner-shell ionization by electron impact with the distorted-wave and plane-wave Born approximations*. Phys. Rev. A 77(4) 042701.
- [89] D. Bote, F. Salvat, A. Jablonski, and C. J. Powell (2009): *Cross sections for ionization of K, L and M shells of atoms by impact of electrons and positrons with energies up to 1 GeV: Analytical formulas*. Atomic Data and Nuclear Data Tables 95(6) 871.
- [90] A. Jablonski, F. Salvat, and C. J. Powell (2009): *Practical formulas for inner-shell ionization cross sections by electron impact: Applications in quantitative Auger electron spectroscopy*. Journal of Applied Physics 106(5) 053706.

## Bibliography

- [91] A. Jablonski, F. Salvat, and C. J. Powell (2010): *Erratum: "Practical formulas for inner-shell ionization cross sections by electron impact: Applications in quantitative Auger electron spectroscopy" [J. Appl. Phys. 106, 053706 (2009)]*. Journal of Applied Physics 107(3) 039901.
- [92] M. Brigida, C. Favuzzi, P. Fusco, F. Gargano, N. Giglietto, et al. (2004): *A new Monte Carlo code for full simulation of silicon strip detectors*. Nuclear Instruments and Methods in Physics Research Section A: Accelerators, Spectrometers, Detectors and Associated Equipment 533(3) 322 .
- [93] M. V. Fischetti, D. J. DiMaria, L. Dori, J. Batey, E. Tierney, et al. (1987): *Ballistic electron transport in thin silicon dioxide films*. Phys. Rev. B 35(9) 4404.
- [94] C. C. Coleman, *Modern Physics for Semiconductor Science* (Wiley-VCH, 2008).
- [95] J. M. Fernández-Varea, X. Llovet, and F. Salvat (2005): *Cross sections for electron interactions in condensed matter*. Surface and Interface Analysis 37(11) 824.
- [96] M. Hötzel (2009): *Berechnung von KATRIN Messspektren unter Einbeziehung der fensterlosen gasförmigen Tritiumquelle*. Diploma thesis, Universität Karlsruhe.
- [97] M. Hötzel (2012): *Modellierung der KATRIN-Tritiumquelle*. Ph.D. thesis in preparation, Karlsruhe Institute of Technology.
- [98] W. Käefer (2011): Ph.D. thesis in preparation, Karlsruhe Institute of Technology.
- [99] M. Babutzka, J. Barrett, T. J. Corona, J. Formaggio, D. Furse, et al. (2010): *The Comprehensive Guide to Kassiopeia*. Version 1.20.00.
- [100] F. Glück (2002): *Runge-Kutta method for numerical solution of differential equation system*. Unpublished.
- [101] K. Valerius (2004): *Elektromagnetisches Design für das Hauptspektrometer des KATRIN Experiments*. Diploma thesis, Rheinische Friedrich-Wilhelm-Universität Bonn.
- [102] R. Brun and F. Rademakers (1997): *ROOT – An object oriented data analysis framework*. Nuclear Instruments and Methods in Physics Research Section A: Accelerators, Spectrometers, Detectors and Associated Equipment 389(1-2) 81. New Computing Techniques in Physics Research V.

- [103] M. Matsumoto and T. Nishimura (1998): *Mersenne twister: a 623-dimensionally equidistributed uniform pseudo-random number generator*. ACM Trans. Model. Comput. Simul. 8 3.
- [104] G. R. Massoumi, W. N. Lennard, P. J. Schultz, A. B. Walker, and K. O. Jensen (1993): *Electron and positron backscattering in the medium-energy range*. Phys. Rev. B 47(17) 11007.
- [105] E. Schreiber and H. J. Fitting (2002): *Monte Carlo simulation of secondary electron emission from the insulator SiO<sub>2</sub>*. Journal of Electron Spectroscopy and Related Phenomena 124(1) 25.
- [106] G. Collaboration) (2008): *Geant4.9.1 Physics Reference Manual*.
- [107] H. Drescher, L. Reiner, and H. Seidel (1970): *Zeitschrift für Angewandte Physik* 29(6) 331.
- [108] K. Hugenberg (2010): *An angular resolved pulsed UV LED photoelectron source for KATRIN*. Progress in Particle and Nuclear Physics 64(2) 288. Neutrinos in Cosmology, in Astro, Particle and Nuclear Physics, International Workshop on Nuclear Physics, 31st course.
- [109] K. Valerius, M. Beck, H. Arlinghaus, J. Bonn, V. M. Hannen, et al. (2009): *A UV LED-based fast-pulsed photoelectron source for time-of-flight studies*. New Journal of Physics 11(6) 063018.
- [110] G. Salace, A. Hadjadj, C. Petit, and M. Jourdain (1999): *Temperature dependence of the electron affinity difference between Si and SiO<sub>2</sub> in polysilicon (n<sup>+</sup>)-oxide-silicon (p) structures: Effect of the oxide thickness*. Journal of Applied Physics 85(11) 7768.
- [111] H. Bichsel and R. P. Saxon (1975): *Comparison of calculational methods for straggling in thin absorbers*. Phys. Rev. A 11(4) 1286.
- [112] I. R. 37 (1984). *Stopping powers for electrons and positrons*.
- [113] M. Nishijima and K. Fujiwara (1977): *Electron energy-loss spectroscopy of NO, O<sub>2</sub> and NH<sub>3</sub> on Si (1 1 1) surfaces*. Solid State Communications 24(1) 101.
- [114] Z.-E.-A. Chaoui and P. Renschler (2010): *Dead layer effect in silicon detectors: energy deposited*. Surface and Interface Analysis 42(6-7) 1093.
- [115] H. Funsten, D. Suszcynsky, S. Ritzau, and R. Korde (1997): *Response of 100% internal quantum efficiency silicon photodiodes to 200 eV-40 keV electrons*. Nuclear Science, IEEE Transactions 44(6) 2561 .

- [116] C. Weinheimer, M. Schrader, J. Bonn, T. Loeken, and H. Backe (1992): *Measurement of energy resolution and dead layer thickness of LN<sub>2</sub>-cooled PIN photodiodes*. Nuclear Instruments and Methods in Physics Research Section A: Accelerators, Spectrometers, Detectors and Associated Equipment 311(1-2) 273.
- [117] F. Scholze and M. Procop (2001): *Measurement of detection efficiency and response functions for an Si(Li) x-ray spectrometer in the range 0.1-5 keV*. X-Ray Spectrometry 30(2) 69.
- [118] R. Hartmann, D. Hauff, P. Lechner, R. Richter, L. Strüder, et al. (1996): *Low energy response of silicon pn-junction detector*. Nuclear Instruments and Methods in Physics Research Section A: Accelerators, Spectrometers, Detectors and Associated Equipment 377(2-3) 191. Proceedings of the Seventh European Symposium on Semiconductor.
- [119] B. Wall (2010): *personal communication*.
- [120] M. Prall for the KATRIN collaboration (2011): *The Katrin experiment and the pre-spectrometer at reduced retarding potential*. Progress in Particle and Nuclear Physics 66(2) 418. Particle and Nuclear Astrophysics, International Workshop on Nuclear Physics, 32nd Course.
- [121] F. Glück (2007): *Electron tracking with the program magfield3.c*. Presentation at the XIIIth KATRIN Collaboration Meeting.
- [122] F. Glück (2006): *Background from positive ions*. Presentation at the XIth KATRIN Collaboration Meeting.
- [123] F. Glück (2010): *Non-adiabatic electron reflection at pre-spectrometer egun*. Presentation at the XVIIIth KATRIN Collaboration Meeting.
- [124] S. Mertens (2012): Ph.D. thesis in preparation, Karlsruhe Institute of Technology.
- [125] B. Wall: Ph.D. thesis in preparation, University of Washington.
- [126] H. Boersch, R. Wolter, and H. Schoenebeck (1967): *Elastische Energieverluste kristallgestreuter Elektronen*. Zeitschrift für Physik A Hadrons and Nuclei 199 124.
- [127] M. Went and M. Vos (2008): *Rutherford backscattering using electrons as projectiles: Underlying principles and possible applications*. Nuclear Instruments and Methods in Physics Research Section B: Beam Interactions with Materials and Atoms 266(6) 998.